2005

Fabrication and Characterization of Schottky diode and Heterojunction Solar cells based on Copper Phthalocyanine (CuPc), Buckminster Fullerene (C60) and Titanium Dioxide (TiO2)

Subhash C. C. Vallurupalli
University of Kentucky

Recommended Citation

Vallurupalli, Subhash C. C., "Fabrication and Characterization of Schottky diode and Heterojunction Solar cells based on Copper Phthalocyanine (CuPc), Buckminster Fullerene (C60) and Titanium Dioxide (TiO2)" (2005). *University of Kentucky Master's Theses*. 260.
https://uknowledge.uky.edu/gradschool_theses/260

Abstract of Thesis

Fabrication and Characterization of Schottky diode and Heterojunction Solar cells based on Copper Phthalocyanine (CuPc), Buckminster Fullerene (C_{60}) and Titanium Dioxide (TiO_2)

Organic solar cells are cheaper and much easier to fabricate than the conventional inorganic solar cells, but they suffer from low efficiencies due to low carrier mobilities in organic films. In this study Copper Phthalocyanine (CuPc) and Buckminster Fullerene (C_{60}) based Schottky diodes were fabricated on ITO coated glass substrates to study their performance and a study of the effect of thickness on the cell parameters of CuPc Schottky diodes was made. Also, TiO_2 based devices were studied to see the effect of TiO_2 layer on the cell parameters. The J-V curves were analyzed for series resistance, diode ideality factor and reverse saturation current density. The devices were also characterized by SEM and XRD measurements.

KEYWORDS: C_{60} , CuPc, TiO_2, Schottky diode solar cells, Heterojunction solar cells.

Subhash C. C. Vallurupalli
Author's Signature

September 18, 2005
Date

FABRICATION AND CHARACTERIZATION OF SCHOTTKY DIODE AND HETEROJUNCTION SOLAR CELLS BASED ON COPPER PHTHALOCYANINE (CuPc), BUCKMINSTER FULLERENE (C_{60}) AND TITANIUM DIOXIDE (TiO_2)

By

Subhash C. C. Vallurupalli

Dr. Vijay P. Singh

(Director of Thesis)

Dr. YuMing Zhang

(Director of Graduate Studies)

(Date)

RULES FOR THE USE OF THESES

THESIS

Subhash C. C. Vallurupalli

The Graduate School

University of Kentucky

2005

FABRICATION AND CHARACTERIZATION OF SCHOTTKY DIODE AND HETEROJUNCTION SOLAR CELLS BASED ON COPPER PHTHALOCYANINE (CuPc), BUCKMINSTER FULLERENE (C_{60}) AND TITANIUM DIOXIDE (TiO_2)

THESIS

A thesis submitted in partial fulfillment of the requirements
for the degree of Master of Science in the
College of Engineering at the
University of Kentucky

By

Subhash C. C. Vallurupalli

Lexington, Kentucky

Director: Dr. Vijay P. Singh, Professor & Chair

Electrical and Computer Engineering

Lexington, Kentucky

2005

MASTER'S THESIS RELEASE

I authorize the University of Kentucky
Libraries to reproduce this thesis in
whole or in part for the purpose of research.

SIGNED: __________________________

DATE: __________________________

ACKNOWLEDGEMENTS

I thank Dr. Vijay P. Singh from the bottom of my heart for having given me a chance to be a part of this research. I am deeply obliged to Dr. J. Todd Hastings and Dr. Ingrid St. Omer for having agreed to be on my Thesis Committee. They have provided outstanding insights that have guided me to deliver a much better work. Their critical review is gratefully acknowledged.

It is only the unparalleled love, support and vision of my parents that has made this work a reality. I would like to thank Dr. Suresh Rajaputra for all his help in this work and for guiding me to solve most of the problems I faced. I would like to thank all my friends who have understood and motivated me during the course of this work. It is their unconditional love that has sustained me through the last couple of years.

Table of Contents

List of Tables

List of Figures

List of Files

Thesis-Subhash.pdf	1.93 MB

Chapter 1. Introduction

1.1 Purpose

For many years, single crystal devices and thin film devices made of inorganic materials served as solar cells for industrial and household applications. However, the trend in recent years has been to use devices whose manufacturing cost is less and which would provide decent performance. This recent trend urged many of the researchers to focus on the cheaper alternative to the inorganic materials i.e., the organic solar cells. The purpose of this research is to gain insight into the different kinds of organic solar cells i.e., the homojunction, heterojunction and the dispersed heterojunction solar cells. For this purpose CuPc (acceptor type) and C_{60} (donor type) were chosen as the basic materials with which the devices were fabricated.

1.2 A brief history of solar cells

In 1839 a French physicist named Antonie-Cesar Becquerel observed that shining light on an electrode submerged in a conductive solution would create an electric current. During the same time a physicist named Edmond Becquerel found that certain material would produce a small amount of electric current when it was exposed to light. This was described as the photovoltaic (PV) effect. Researchers from various parts of the world observed this phenomenon and were trying to find a way in which this phenomenon could be used to generate electricity on a large scale. They found that selenium PV cells were converting light to electricity. These selenium solar cells had an efficiency of 1% to 2%.

In 1941, an American scientist named Russel Ohl invented a silicon solar cell. In 1954, scientists at Bell Laboratories used the Czochralski process to develop the first crystalline silicon photovoltaic cell which had an efficiency of 4%. In the second half of the 20th century the science behind the solar energy was fully understood which led to improvements in the PV conversion efficiencies.

Solar cells became a good source of electricity for satellites and were also used as cheaper alternatives for power lines in remote areas. Even today, space use remains the primary application of solar cells. Solar cells could not replace the conventional means of generating electricity because of the large costs involved in manufacturing them.

1.3 Current trends with solar cells

With the accelerated interest in solar cells people searched for more materials which exhibited photovoltaic properties with higher efficiencies and lower cost of manufacturing. In the 1960's scientists turned towards the thin film materials due to their low cost of production. The thin film solar cells have reduced the cost of production of solar cells by a considerable amount. Thin film solar cells eliminate the expensive crystal growth techniques by using closed space sublimation, sputtering and deposition techniques. However thin film solar cells face some problems such as low efficiency and short lifetime [1]. In recent years researchers started focusing on cheaper alternatives for manufacturing solar cells. This paved the way for the organic materials to enter the field of photovoltaics. The first ever organic solar cell fabricated in the year 1986 [2] had an efficiency of 1%. Since then the efficiency of the organic solar cells started to increase and as of now, stands at about 4-5%. The efficiencies of organic solar cells are much less when compared to their inorganic counterparts but the ease with which they can be fabricated and also their cost of production makes them a good alternative [3]. Organic solar cells could be manufactured by printing or spraying the materials on to a roll of plastic. We could even have a sheet of solar cells that could be unrolled and put on a roof. The cells also could be made in different colours or even be transparent making them good architectural elements.

Organic solar cells are plagued with problems such as low efficiency and shorter lifetime. Today most of the research is focused on improving the efficiency and also to increase the lifetime of these cells.

1.4 C_{60} based Schottky diode solar cells

C_{60} also known as buckminster fullerene is a spherical shaped molecule which is used as an n-type organic semiconductor. C_{60} Schottky diode solar cells with ITO(Indium Tin Oxide)/C_{60}/Al structure and efficiencies of less than 10^4 were reported by Tetsuya Taima et al., [4]. They reported an open circuit voltage of 0.046 V and a short circuit current of 2.77 x 10^2 mA/cm^2. In this thesis, an effort has been made to increase the efficiency of these solar cells by improving the open circuit voltage and short circuit current. PEDOT:PSS(3, 4-polyethylenedioxythiophene: polystyrene sulfonate) was spincoated onto the ITO coated glass before the deposition of C_{60} to make the surface of ITO smooth. Also, LiF was deposited on the C_{60} film before the deposition of aluminium contacts to protect the surface of C_{60} from high energy Al atoms. The devices are characterized by SEM (Scanning Electron Microscopy), UV-Vis (Ultra Violet-Visible spectroscopy), XRD (X-Ray Diffraction) and I-V (Current-Voltage) measurements.

1.5 CuPc based Schottky diode solar cells

CuPc stands for Copper Phthalocyanine a p-type organic semiconductor which is widely used because of its low cost and good photoelectronic properties [5-6]. CuPc Schottky diode solar cells with ITO/CuPc (100 nm)/Al structure were fabricated by C.W. Kwong et al., [7] and they have reported a open circuit voltage of 0.94 V, short circuit current density of 23.5 μA/cm^2 and an efficiency of 0.00406 %. Organic Schottky diode solar cells are less efficient when compared to their inorganic counterparts because of low carrier mobility. In this thesis, we tried to study the effect of varying the thickness of the CuPc layer on the cell parameters such as open circuit voltage, short circuit current and efficiency etc.. As in the case of the C_{60} Schottky diode solar cells, PEDOT:PSS was spincoated on the surface of ITO coated glass before the deposition of CuPc to smooth out the irregularities of the ITO surface. Also the devices were characterized by SEM, UV-Vis, XRD and I-V measurements.

1.6 TiO_2/CuPc/Al and TiO_2/CuPc/PTCBI/Al solar cells

Titanium dioxide (TiO_2) is a well known n-type semiconductor. TiO_2/CuPc heterojunctions with structure ITO/TiO_2/CuPc (460 nm)/Au were fabricated by A. K. Ray et al., [8] with an open circuit voltage of 0.024 V, 0.012 mA/cm^2 at an illumination of 60 mW/cm^2. Annealed spin coated titanium dioxide films are known to produce porous films which can be used for the scattering of light, and thereby increasing the effective optical path of light. In this thesis, an attempt has been made to reduce the thickness of the CuPc film to avoid the recombination of the carriers, and thus to produce better efficiency. UV-Vis measurements were made to check the peaks of the absorption curves. Also, SEM and I-V measurements were made to calculate the cell parameters.

Chapter 2. Theory

2.1 Theory of Schottky diode solar cells

Depending on the work functions of the metal and the semiconductor the type of contact between a metal and a semiconductor can be rectifying or ohmic. Rectifying metal-semiconductor contacts are used in applications that require fast switching [9-10]. A Schottky barrier forms between a metal and a semiconductor contact in the following cases,

1. When $\Phi_m<\Phi_s$ and the semiconductor is p-type.
2. When $\Phi_m>\Phi s$ and the semiconductor is n-type.

Figure 2.1 and 2.3 depict the energy level diagrams of the metal and a p-type semiconductor before and after contact and Figure 2.2 and 2.4 depict the energy level diagrams of the metal and a n-type semiconductor after contact.

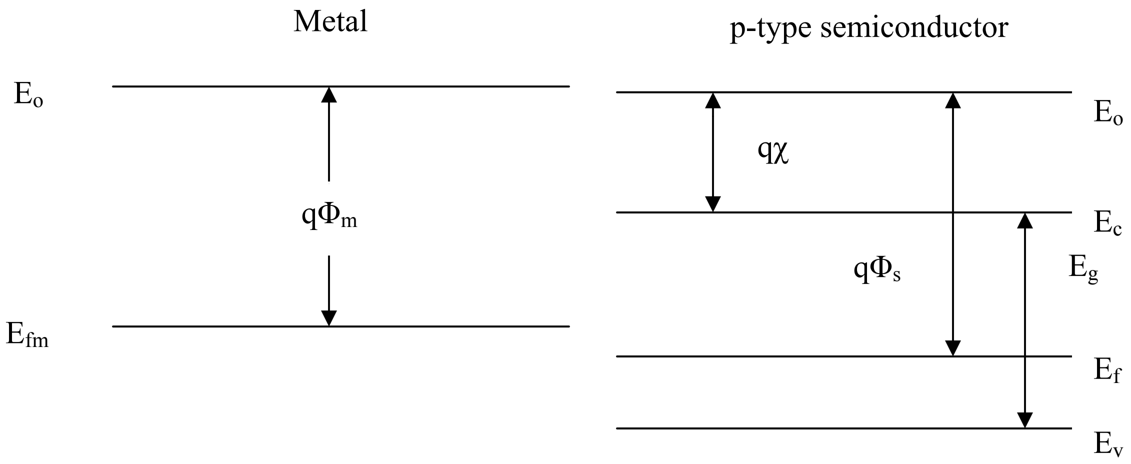

Figure 2.1 Energy levels of metal and a p-type semiconductor before contact.

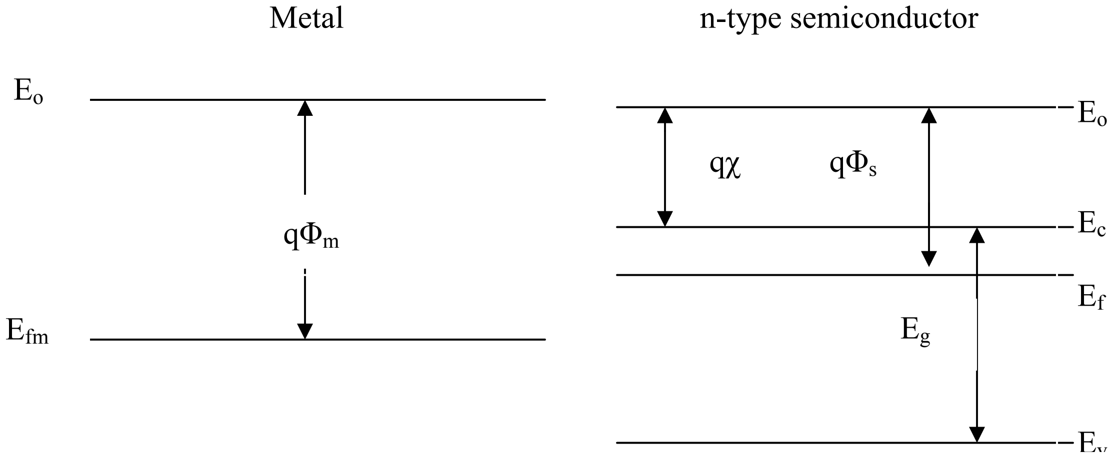

Figure 2.2 Energy levels of metal and a n-type semiconductor before contact.

$q\Phi_m$ - work function of metal.
$q\Phi_s$ - work function of semiconductor.
$q\chi$ - electron affinity of semiconductor.
E_o - vacuum level.
E_{fm} - metal fermi energy level.
E_f - semiconductor fermi energy level.
E_c - conduction band level.
E_v - valence band level.

When the semiconductor and the metal are brought into contact, the electrons would diffuse from the metal to the semiconductor until the Fermi levels of both sides are aligned and the system reaches equilibrium [11].

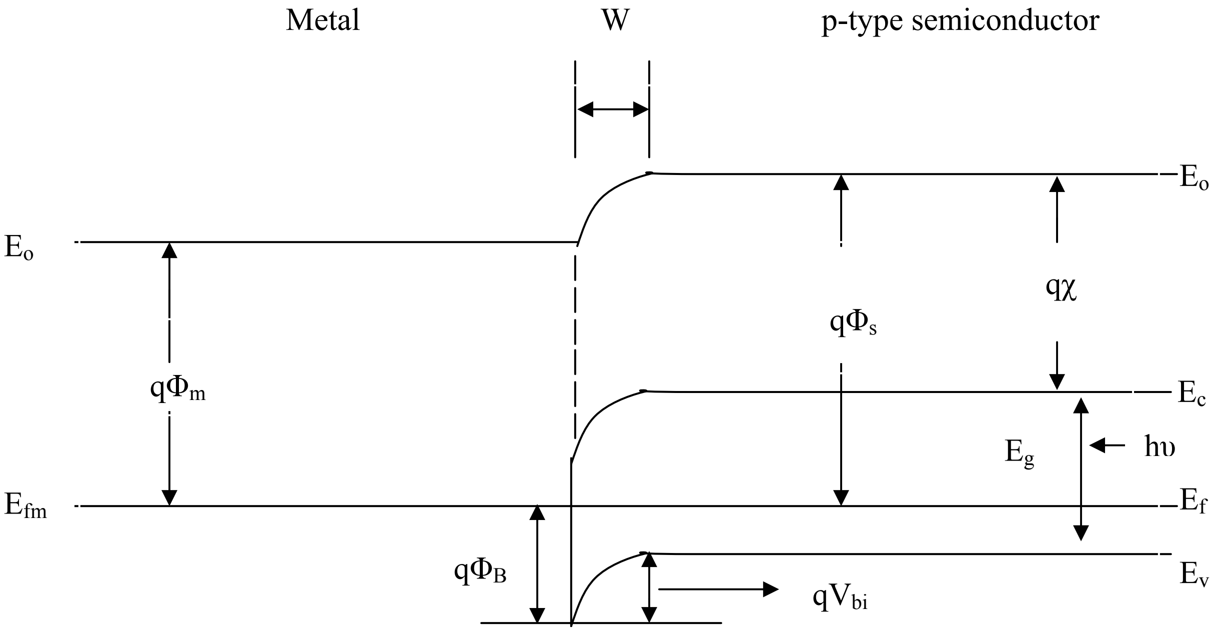

Figure 2.3 Energy levels of metal and a p-type semiconductor after contact.

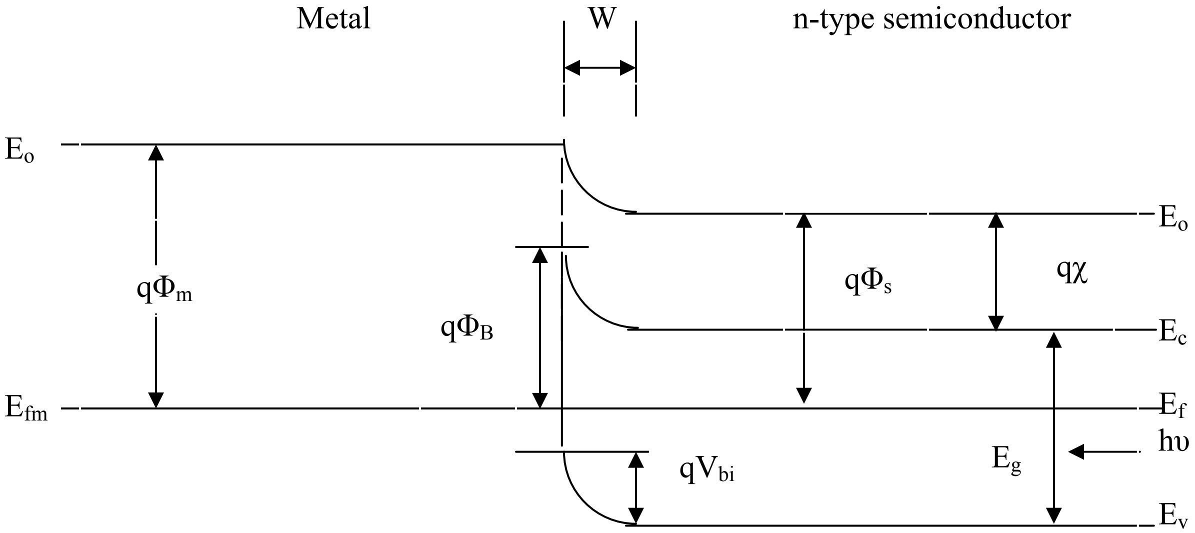

Figure 2.4 Energy levels of metal and a n-type semiconductor after contact.

A negative charge of width 'W' is developed in the p-type semiconductor and a positive charge of width 'W' is developed in the n-type semiconductor. This charge is balanced by a sheet charge of opposite type developed on the metal side as a result of the charge transfer. The effective depletion width is the width of the depletion region in the semiconductor, as the width of the sheet charge in the metal is negligible. Light with energy greater than 'E_g' will be absorbed by the n-type and the p-type material, and the carriers created in the depletion region and within a diffusion length of the junction will be collected. The separation of the light generated carriers across the barrier gives rise to the light generated current I_L.

2.2 Theory of Heterojunction Solar Cells

A heterojunction is formed between two semiconductors with different crystal structure, bandgap and other properties. Consider separate n-type and p-type semiconductor crystals. The energy band diagram for the n and p type semiconductors before contact is shown in Figure 2.5. The difference in electron concentrations between the two materials causes electrons to flow from n to p-type semiconductor and holes from p to n-type semiconductor when the two materials are brought together. This movement of the carriers into the oppositely doped materials leads to a charge build up near the junction and a subsequent electric field. This electric field extends from the n-side of the junction to the p-side. The energy band diagram of the p-type and the n-type semiconductors after the contact is depicted in Figure 2.6.

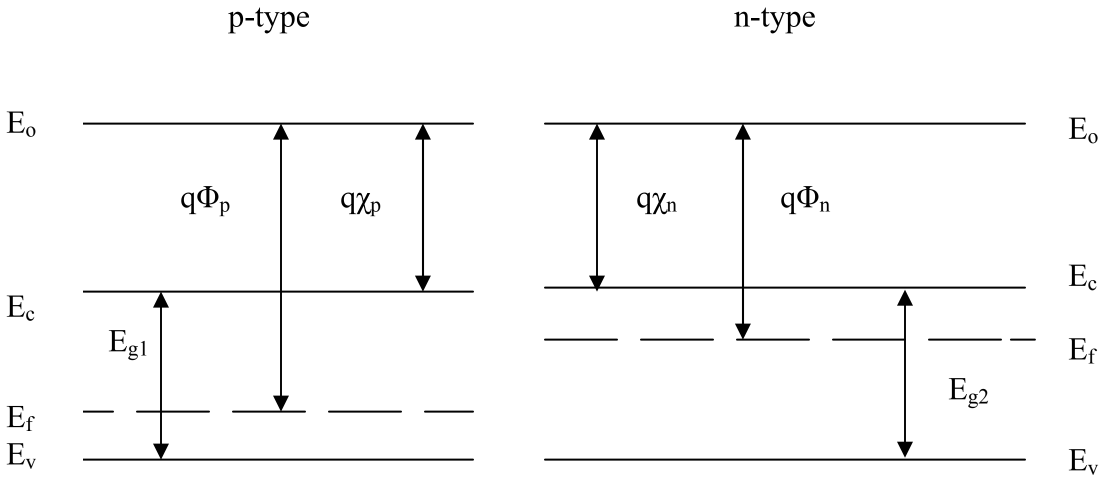

Figure 2.5 Energy levels of p and n type semiconductors before contact.

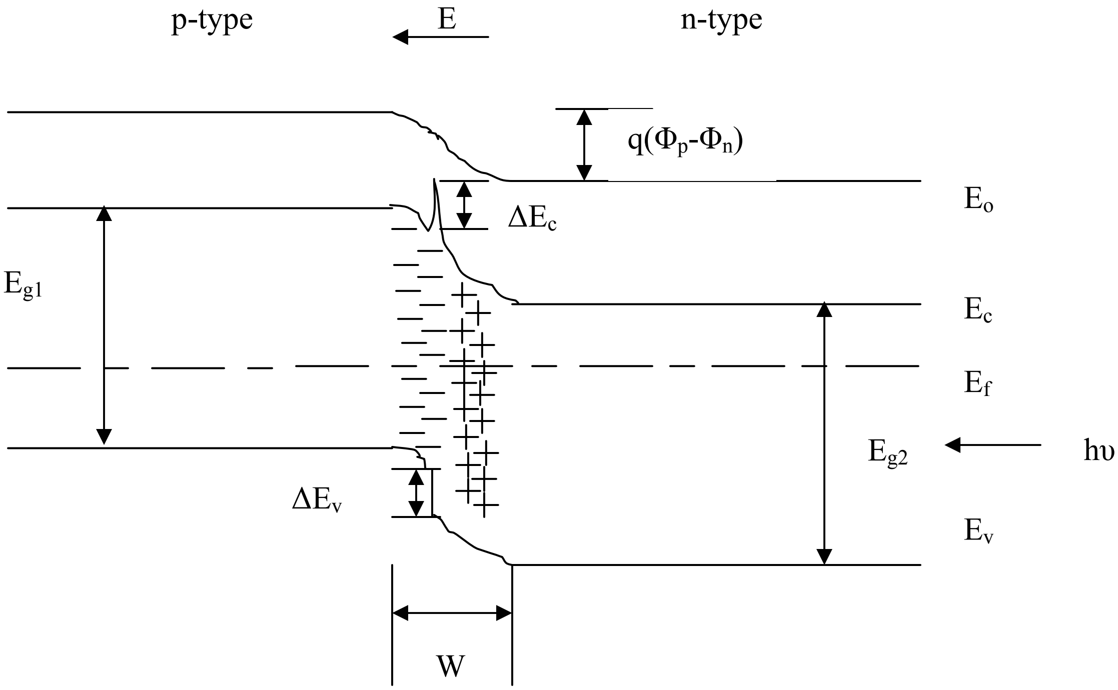

Figure 2.6 Energy band diagram of a heterojunction solar cell.

When light impinges on the cell, the photons with energy less than E_{g2} and greater than E_{g1} pass through the n-type semiconductor, will be absorbed by the p-type material and creates carriers which are collected. The photons with energy greater than E_{g2} are absorbed by the n-type material and lead to generation of carriers in the depletion region and as well as the bulk of the material. These separated carriers at the junction give rise to the light generated current I_L.

2.3 Principles of operation of organic solar cells

The fundamental physics of organic solar cells still remains poorly understood [12].Organic photovoltaic materials differ from inorganic photovoltaic materials in the following ways:

1. Photogenerated excitons are strongly bound to each other and do not dissociate into charge pairs by themselves as opposed to the conventional inorganic photovoltaic materials [13-15].

2. The mobilities of these charges are less when compared to those of inorganic materials.
3. The spectral range of absorption is relatively narrow when compared to the inorganic materials.

Homojunction: The simplest device structure for an organic solar cell is a homojunction which is essentially a sandwich of the organic photovoltaic material between two conducting contacts. The difference in the work function of these two contacts provides the necessary electric field which drives the separated charge carriers towards the contacts. Also the generation of separate charges occurs as a result of dissociation of these strongly bound excitons by interaction with interfaces, impurities or defects [16-17]. This electric field sometimes may not be sufficient to break the excitons i.e., the electron-hole pair. In this case the exciton itself travels to the contact where it breaks down into the constituent charges [18].

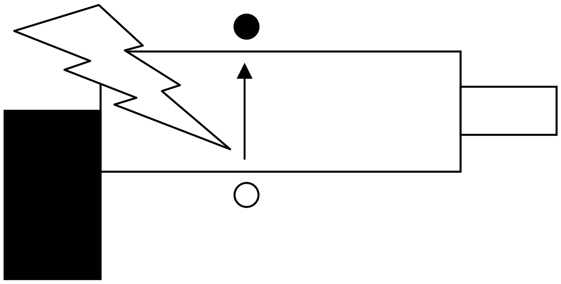

Figure 2.7 Generation of excitons in the organic semiconductor.

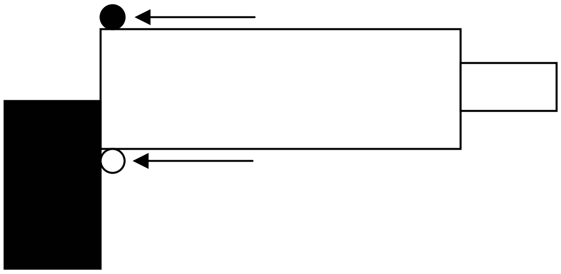

Figure 2.8 Diffusion of the exciton towards a contact.

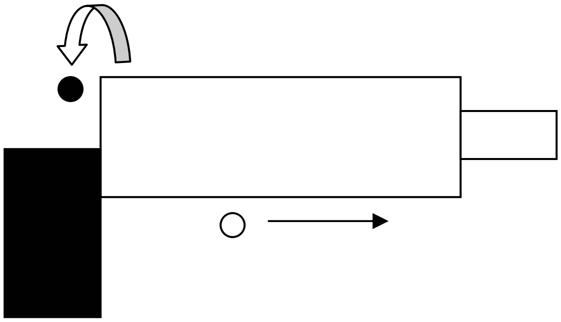

Figure 2.9 Dissociation of the exciton into its constituent electron and hole.

Heterojunction: The heterojunction solar cells are fabricated by sandwiching the donor and the acceptor organic photovoltaic materials between two different electrodes. In the heterojunction solar cells, electrostatic forces develop at the interface due to the differences in the electron affinity and ionization potential. This electric field is strong and can break the photogenerated excitons if the potential energy difference is greater than the exciton binding energy.

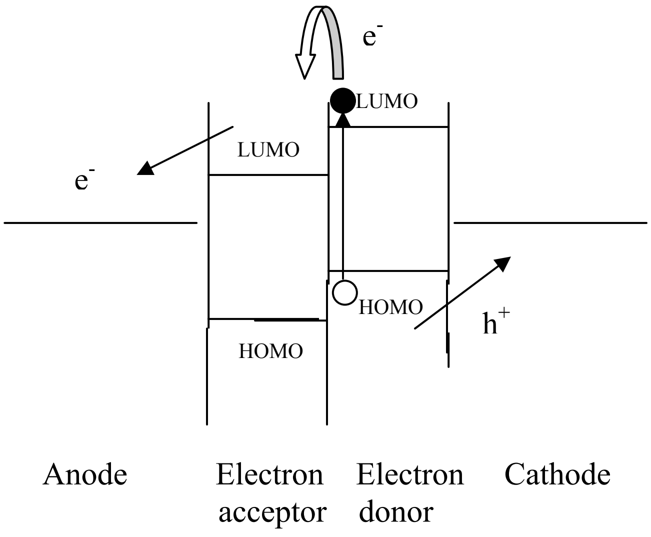

HOMO – Highest occupied molecular orbital.

LUMO – Lowest unoccupied molecular orbital.

Figure 2.10 Donor-Acceptor heterojunction of two organic Semiconductors.

2.4 Equivalent Circuit of a Solar Cell

To understand the electronic behavior of a solar cell, it is useful to create an electrically equivalent model whose components are well known. An ideal solar cell can be modeled by a diode in parallel with a current source [19-22]. Since practical solar cells are not ideal, a series resistance and a shunt resistance are added to the model. The equivalent circuit of a solar cell is shown in Figure 2.11.

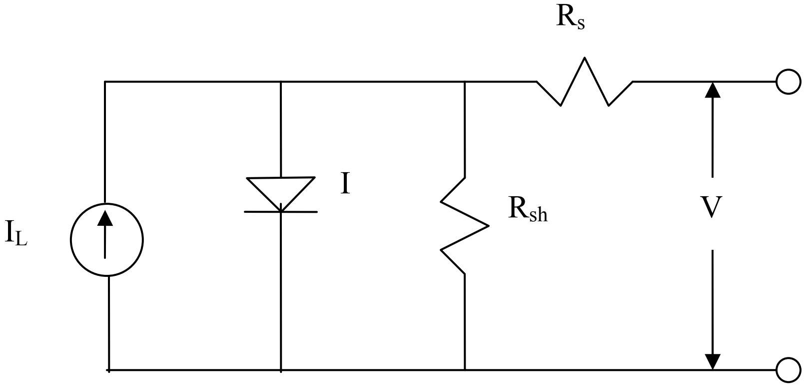

Figure 2.11 Equivalent circuit of a solar cell.

Here, R_s - series resistance associated with the device,

R_{sh} - shunt resistance associated with the device,

V - voltage across the device,

I_L - light-generated current,

I - current through the device.

The shunt resistance R_{sh}, arises from the presence of shunting paths formed between the layers during deposition. The series resistance (R_s), arises from the resistance associated with quasi neutral regions and the ohmic contacts.

2.5 Photovoltaic Parameters

The photovoltaic parameters of a solar cell include open-circuit voltage, short circuit current, maximum power output, fill factor and efficiency.

2.5.1 Short-Circuit Current

The current that flows between the two terminals of a solar cell when they are connected together and when light impinges on the cell is called the short circuit current. Short circuit current is directly proportional to the number of incident photons and is represented by I_{SC}.

2.5.2 Open-Circuit Voltage

The voltage that is developed when the terminals of the cell are isolated and when light impinges on the cell is called the open circuit voltage of the solar cell and is represented by V_{OC}.

2.5.3 Maximum Power Output

The maximum power output of a solar cell is a measure of the maximum power that can be delivered by the solar cell. It can be calculated as $P_m=I_mV_m$, where V_m and I_m represent the maximum values of voltage and current in the fourth quadrant of the I-V curve. The point where the power delivered reaches maximum is called the operating point of the solar cell.

2.5.4 Fill Factor

The fill factor of a solar cell is defined as the ratio of V_mI_m and $V_{oc}I_{sc}$ and it describes the squareness of the I-V curve.

$$\text{Fill Factor} = V_mI_m/V_{oc}I_{sc} \qquad 2.1$$

2.5.5 Efficiency

The efficiency of a solar cell is defined as the ratio of the power delivered at the operating point and the incident power.

$$\eta = (V_mI_m/P_{in})\text{x}100\% \qquad 2.2$$

Efiiciency is related to I_{sc} and V_{oc} using fill factor(FF) as

$$\eta = I_{sc}\ V_{oc}\ FF/P_{in} \qquad 2.3$$

Chapter 3. Experimental

3.1 Device Fabrication

3.1.1 Device Structures

Devices with structure

1) Glass/ITO/C_{60}/LiF/Al
2) Glass/ITO/PEDOT:PSS/C_{60}/LiF/Al
3) Glass/ITO/PEDOT:PSS/CuPc/Al
4) Glass/ITO/TiO_2/CuPc/Al
5) Glass/ITO/TiO_2/CuPc/PTCBI/Al

were fabricated. Figures 3.1, 3.2, 3.3, 3.4 and 3.5 depict the structure of the solar cells fabricated. ITO coated glass substrates were commercially purchased from Delta Technologies, Limited, Stillwater, MN. ITO, a transparent conductor serves as the bottom contact to the films and the glass provides mechanical support.

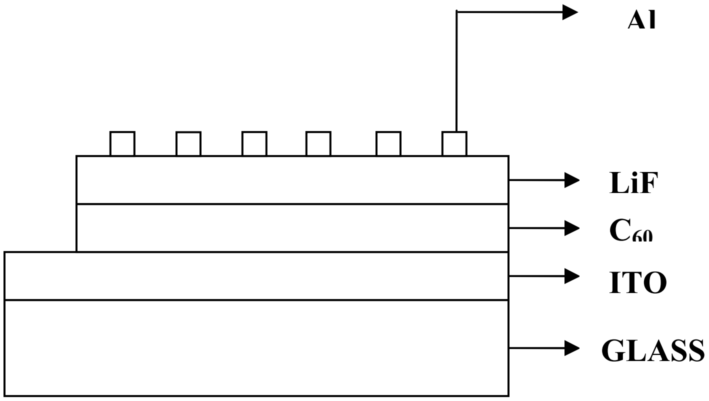

Figure 3.1 Glass/ITO/C_{60}/LiF/Al.

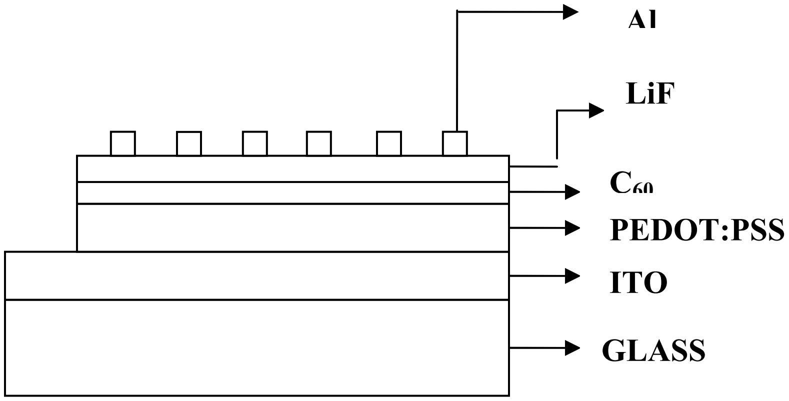

Figure 3.2 Glass/ITO/PEDOT:PSS/C_{60}/LiF/Al.

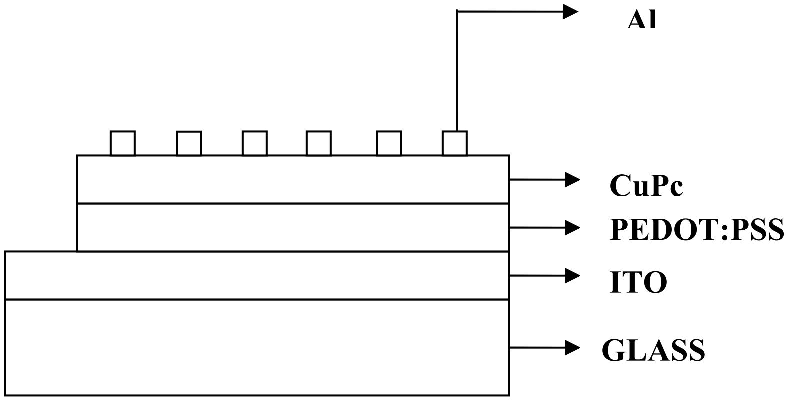

Figure 3.3 Glass/ITO/PEDOT:PSS/CuPc/Al.

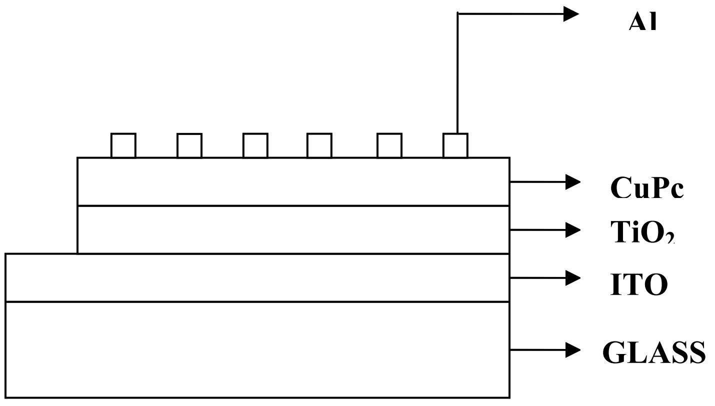

Figure 3.4 Glass/ITO/TiO_2/CuPc/Al.

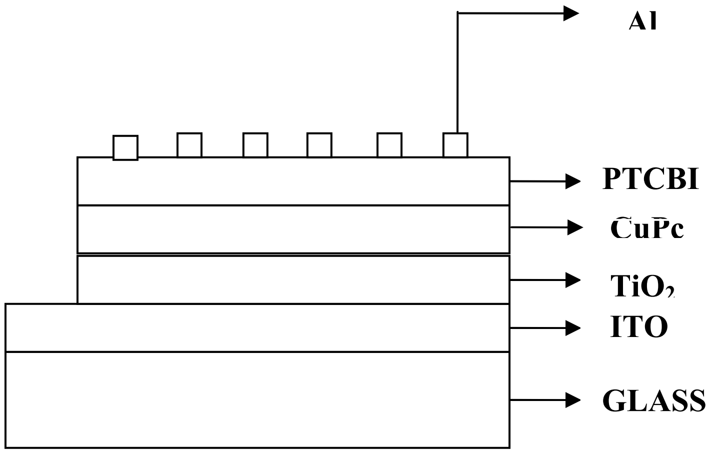

Figure 3.5 Glass/ITO/TiO_2/CuPc/PTCBI/Al.

3.1.2 Preparation of TiO_2 Sol-Gel

TiO_2 films were prepared by Sol-gel [23-24]. The reagents, namely titanium Tetra isopropoxide (99.999%), isopropanol (99.5%) and nitric acid (70% redistilled) were procured from Aldrich. The precursor titanium tetra isopropoxide (TTIP) was dissolved in isopropanol in a nitrogen environment to which deionized water and then nitric acid were added. The solution was stored in a nitrogen environment after being stirred for 2 hours. A typical preparation of 0.1 M TiO_2 solution contained 1 ml of TTIP, 0.05 ml of HNO_3 (70% distilled), 0.1 ml de-ionized water and 32.7 ml of isopropanol.

3.1.3 Substrate Cleaning

Prior to the fabrication of the devices the ITO coated glass substrates were cleaned thoroughly. Cleaning the substrates is an essential step which is performed prior to spincoating the PEDOT:PSS and TiO_2 films to obtain smooth and contaminant free films on the ITO coated glass. Initially the substrates were cleaned with de-ionized water. The substrates were then transferred to a beaker containing acetone and sonicated for about 10 minutes. The substrates were then cleaned again with de-ionized water. Then, the substrates were again transferred to a beaker containing methanol and sonicated for 10 minutes. The substrates were then cleaned with de-ionized water and were finally dried with flowing nitrogen. The ITO coated glass substrates were then electrically characterized to identify the ITO coated side by applying a small voltage on each side of the substrate and measuring the resulting current. The side of the glass without the ITO coating does not allow the passage of any current through it.

3.1.4 Spincoating of the PEDOT:PSS film for device structures 2 and 3

PEDOT:PSS was purchased from Bayer. The PEDOT:PSS films were spincoated onto the ITO side of the substrates using Chemat technology spin coater. The speed of the spincoater was set to 4000 rpm and the duration of the spin was 40 seconds. The substrates were then annealed in a Fisher-Scientific furnace at a temperature of 100^oC for about 1 hour to dry the PEDOT:PSS films and also to increase the adhesion of the films.

3.1.5 Spincoating of the TiO_2 sol-gel for device structures 4 and 5

TiO_2 solution prepared using the sol-gel technique was spin coated on the surface of the ITO coated glass substrates. The speed of the spincoater was set to 2000 rpm and the duration of the spin was 40 seconds. The substrates were then annealed overnight in a Boekel Industries furnace at a temperature of 300°C to increase the adhesion of the films.

3.1.6 Fabrication of C_{60} films

The C_{60} films were made by thermal evaporation of the powdered C_{60} obtained from Sigma-Aldrich. The C_{60} powder was kept in a molybdenum boat and a current of the order of approximately 4.0 A was passed through the boat. During the evaporation process, the pressure in the chamber was maintained at $1x10^{-6}$ Torr. The substrates were attached to a disc at a height of 30cms from the C_{60} source. The current was increased in steps of 0.5 A upto 4.0 A. The pressure in the chamber is maintained at the same level all through the evaporation process to maintain the uniformity of the films. The high vacuum in the chamber is required to avoid the vapors being deflected and also to avoid the oxidation of the films. The thickness of the C_{60} films was monitored using a quartz crystal monitor. A LiF layer was deposited on the C_{60} layer to protect it from high energy Aluminium atoms [25].

3.1.7 Fabrication of CuPc films

The CuPc films were made by thermal evaporation of the powdered CuPc obtained from Sigma-Aldrich. The powdered CuPc was kept in a molybdenum boat and a current of approximately 3.7 A was passed through the boat. During the evaporation process, the pressure in the chamber was maintained at $1x10^{-6}$ Torr. The substrates were attached to a disc at a height of 30 cms from the CuPc source. The current was increased in steps of 0.5 A upto 3.7 A. The pressure in the chamber is maintained at the same level all through the evaporation process to maintain the uniformity of the films. The high vacuum in the chamber is required to avoid the vapors being deflected and also to avoid the oxidation of the films. The thickness of the CuPc films was monitored using a quartz crystal monitor.

3.1.8 Fabrication of PTCBI (3,4,9,10-perylenetetracarboxylic bis-benzimidazole) films

The PTCBI films were made by thermal evaporation of the powdered PTCBI obtained from Dr. Anthony's lab in the Chemistry department at the University of Kentucky. The powdered PTCBI was kept in a molybdenum boat and a current of approximately 4.2 A was passed through the boat. During the evaporation process the pressure in the chamber was maintained at $1x10^{-6}$ Torr. The substrates were attached to a disc at a height of 30cms from the PTCBI source. The current was increased in steps of 0.5 A upto 4.2 A. The pressure in the chamber is maintained at the same level all through the evaporation process to maintain the uniformity of the films. The high vacuum in the chamber is required to avoid the vapors being deflected and also to avoid the oxidation of the films. The thickness of the CuPc films was monitored using a quartz crystal monitor.

3.1.9 Deposition of Aluminium contacts

The aluminium contacts were made on the films by thermal evaporation of aluminium. We used a tungsten basket for depositing the aluminium electrodes. Aluminium pellets purchased from Sigma-Aldrich were kept in a tungsten basket and the chamber was left pumping overnight since the current required for the evaporation of aluminium electrodes is high, which in turn increases the pressure in the chamber. The current that was passed through the basket was approximately 4.8 A. The substrates were covered with a mask of aluminium foil in which circular holes of area $0.07cm^2$ were made. The aluminium gets deposited in these circular holes thus creating circular electrodes of $0.07cm^2$ area. After the deposition of aluminium the chamber was left to cool down for about two hours and then the devices were measured for J-V characteristics.

3.2 X-Ray Diffraction (XRD)

In XRD, a diffraction pattern results from the interaction of x-rays with the material. XRD provides information regarding the phase, structure and composition of the material [26]. An XRD pattern is unique for each material.

X-rays are diffracted by a series of planes whose orientation is defined with the Miller indices h, k and l when incident on a crystal. If a, b and c are considered to be axes of the unit cell then h, k and l would cut the axes a, b and c into h, k and l sections respectively. The constructive interference would occur at an angle of incidence θ which satisfies Bragg's law given in equation 3.1.

$$2d\sin\theta = n\lambda \qquad 3.1$$

where d is the spacing between the parallel planes
n is an integer
λ is the wavelength of the x-rays.

The d-spacing among the planes in the crystal corresponds to the peak intensities at 2θ positions obtained from the XRD pattern. By comparing with the previously calculated reference the indices of the planes and the phase of the material can be estimated. The material can be identified by comparing with a standard set of data.

3.3 Field Emission Scanning Electron Microscopy (FE-SEM)

In Field Emission Scanning Electron Microscopy a beam of electrons generated by a field emission source scans the surface of the sample. The electrons which are generated in an electron gun are accelerated in a column with a high electrical field gradient. When the electrons bombard the sample, back scattered electrons, secondary electrons, light, heat and transmitted electrons are generated. Backscattered electrons are the ones that are bounced off the nuclei of atoms in the sample. Secondary electrons are the electrons from the sample. An electronic signal is generated by a detector which catches the secondary electrons. From the velocity and angle of the secondary electrons, the surface structure of the sample can be determined. Finally the signal is processed with amplifiers and the image is seen on the monitor [27].

3.3.1 Sample Preparation

The samples are mounted on copper stubs specifically available for SEM imaging. The copper stubs were cleaned by sonicating them with acetone and DI water. Later, they were wiped clean with kim wipes and dried in flowing nitrogen. A graphite tape of dimensions 2 mm x 6 mm was cut and pasted on the copper stub. Now the test sample is cut with dimensions less than the graphite tape and is firmly placed on the graphite tape. A conducting colloidal graphite paste is used to cover the edges of the sample by using a paint brush. Finally the samples are coated with gold before placing them in the SEM chamber.

3.3.2 Specimen Exchange

The specimen exchange chamber is isolated from the main chamber so that the air does not enter the main chamber. The specimen holder in the specimen exchange chamber has a set of grooves to hold the stub. The specimen is placed in the required groove depending on the thickness and imaging requirements. By following the standard procedures the specimen holder is replaced into the specimen exchange chamber.

3.3.3 SEM Imaging

The sample under test is first focused with low magnification. The object is then moved to the center of the screen and focused with high magnification. The aperture align switch is turned on and the sample checked for horizontal or vertical swing. In the presence of a swing the screws on the aperture holder are adjusted until the swing disappears. The image is then sharpened using the X and Y stigmator controls. This is done until we obtain the sharpest image.

3.4 Optical Absorption

Optical absorption is a technique used to calculate the bandgap energy (E_g) of a semiconductor. The absorption is recorded by making photons of selected wavelength incident on the sample under test. A semiconductor consists of a valence band which has electrons and a conduction band which is empty. When the sample is hit with photons the electrons absorb photons with energy higher than the bandgap (E_g) and jump to the conduction band as shown in Figure 3.5. The photons with energy less than the bandgap (E_g) are not absorbed since they cannot supply the electrons with energy required to cross the bandgap. The electrons which were initially excited and which have crossed to the conduction band, loose that excess energy to the lattice and reach thermal equilibrium.

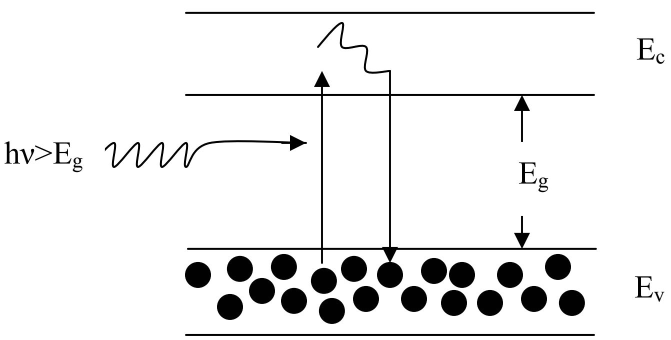

Figure 3.6 Figure depicting absorption of photons with hν>E_g.

3.4.1 Measurement of Spectrum

ITO/PEDOT:PSS/CuPc was taken as the test sample and ITO/PEDOT:PSS was taken as a reference sample. Dual beam spectrophotometer was used for the measurements as shown in the Figure 3.6. Two beams of equal intensity, one through the test sample and the other through the reference sample were passed and the resulting intensities of both the beams were compared over the selected wavelength range and plotted as $\log_{10}(I_o/I)$ where I is the intensity through the sample and I_o is the intensity through the reference sample [28].

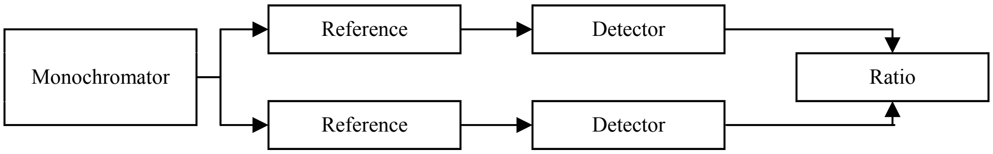

Figure 3.7 UV-Vis Spectrophotometer block diagram.

3.5 I-V Measurement Setup

The circuit diagram for the I-V measurement setup is shown in the Figure 3.7. Two Keithley digital multimeters and a DC power supply were used in performing these measurements. The measurements were recorded by a Labview software program.

Measurements were made within a voltage range of -1V to +1V. I-V sweep and delay time were controlled with the software.

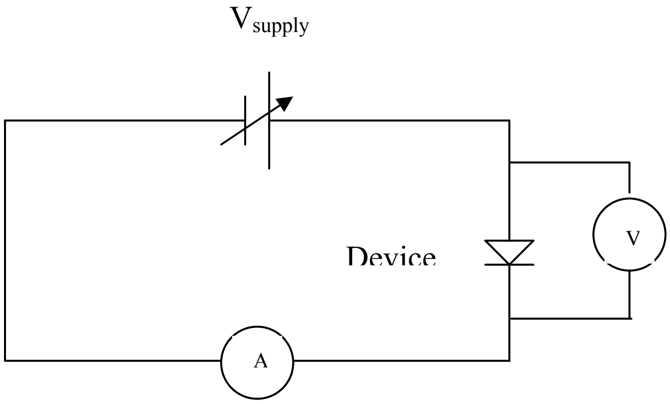

Figure 3.8 Circuit diagram of I-V measurement setup.

A – Ammeter used for the measurement of current through the device.

V – Voltmeter used for the measurement of voltage acroos the device.

V_{supply} – Supply voltage.

Device – Device under test.

The electrical characteristics of the device under illumination were measured with the help of a solar simulator. The solar simulator is a rectangular box with a bulb of illumination 1 sun (incident power of 100 mW/cm^2) at the bottom of the box and a glass slab on the top on which the device to be tested is mounted.

Chapter 4. Material Characterization

4.1 Characterization of C_{60} by SEM

C_{60} is a well-known n-type organic semiconductor and is being used in the fabrication of organic solar cells and OLED's. C_{60} has been used in the fabrication of Glass/ITO/PEDOT:PSS/C_{60}/LiF/Al and Glass/ITO/PEDOT:PSS/C_{60}/LiF/Al solar cells. C_{60} was thermally evaporated on the PEDOT:PSS coated glass substrates. Figure 4.1 shows the SEM image of C_{60} at a high magnification.

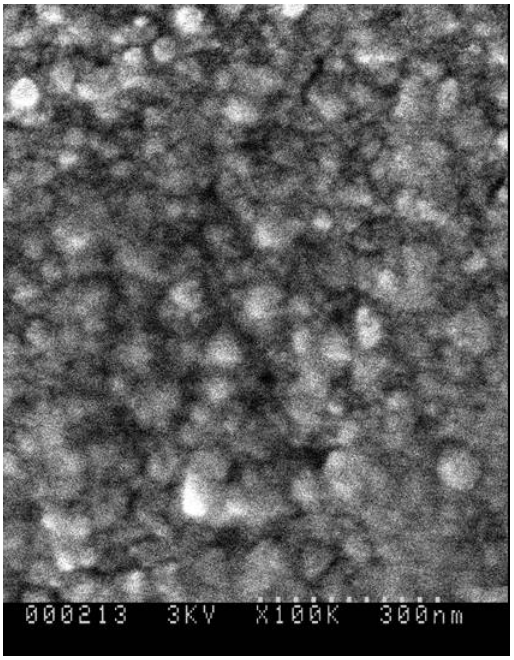

Figure 4.1 SEM image of C_{60} at high magnification.

The deposited film was uniform with a particle size of 30 nm. The SEM image of C_{60} at a low magnification is shown in Figure 4.2 which confirms the uniformity of the film.

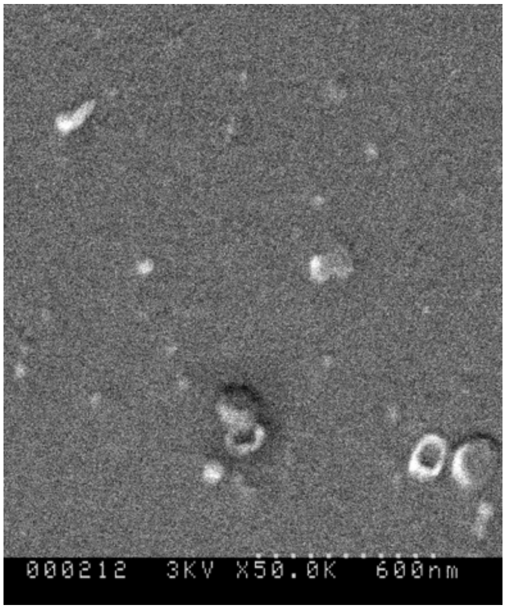

Figure 4.2 SEM image of C_{60} at low magnification.

4.2 Characterization of C_{60} by XRD

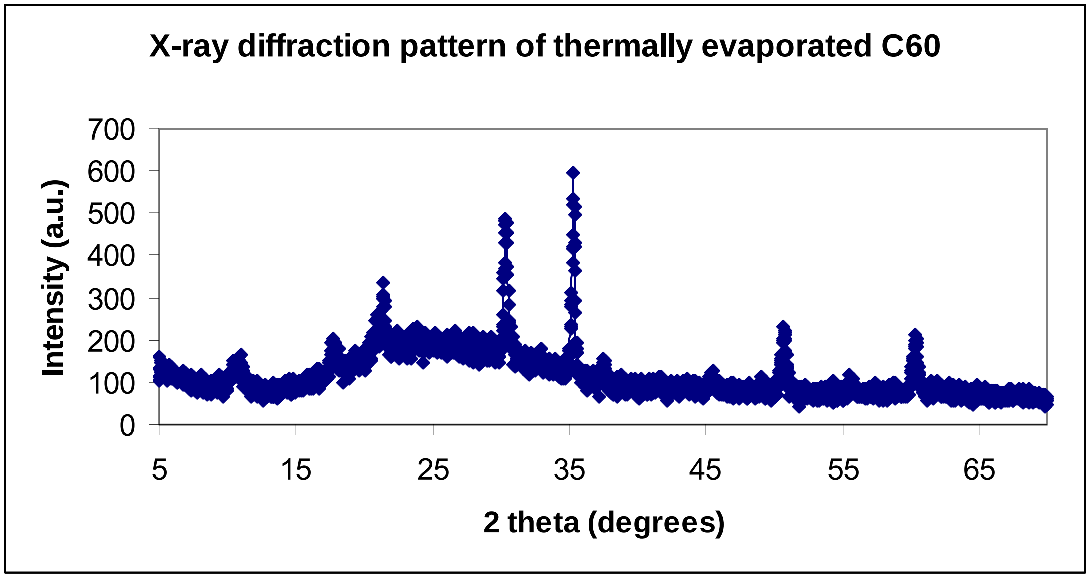

Figure 4.3 XRD of thermally evaporated C_{60} film.

The X-ray diffraction pattern of the thermally evaporated C_{60} film shows peaks at 2Θ positions of 10.1^0 (111), 22^0 (222), 34^0(333). The peaks at positions 23^0, 30^0,

35^0, 37^0, 45^0, 51^0 and 60^0 are produced by ITO.

4.3 Characterization of CuPc by SEM

CuPc is a well known p-type organic semiconductor used in the fabrication of organic solar cells and OLED's. CuPc was used in the fabrication of devices Glass/ITO/PEDOT:PSS/CuPc/Al, Glass/ITO/TiO_2/CuPc/Al and Glass/ITO/TiO_2/CuPc/PTCBI/Al. Figure 4.4 shows the SEM image of the thermally evaporated CuPc film on an ITO coated glass substrate at a high magnification.

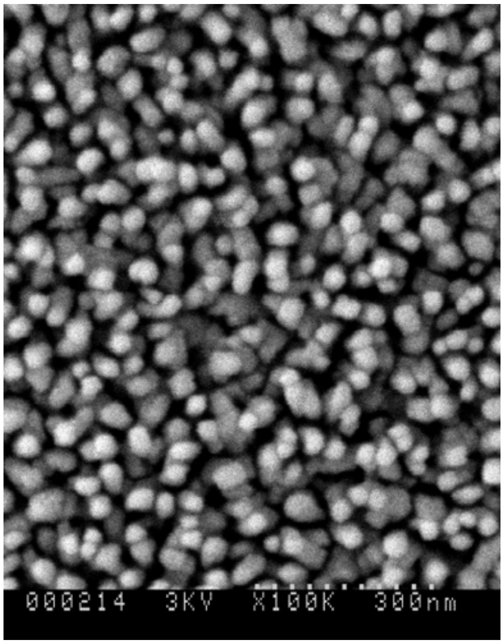

Figure 4.4 SEM image of CuPc at high magnification.

From Figure 4.4 it can be observed that the average particle size of the thermally evaporated CuPc film is around 30 nm. Figure 4.5 shows the SEM image of the CuPc film at a lower magnification. From Figure 4.5 it can be seen that the CuPc film is uniform.

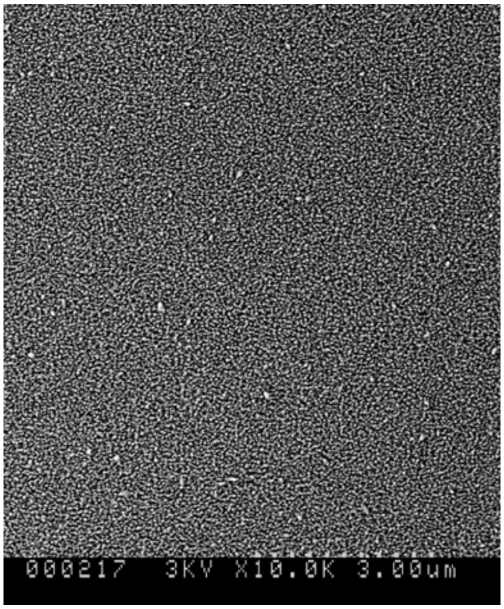

Figure 4.5 SEM image of CuPc at low magnification.

4.4 Characterization of CuPc by XRD

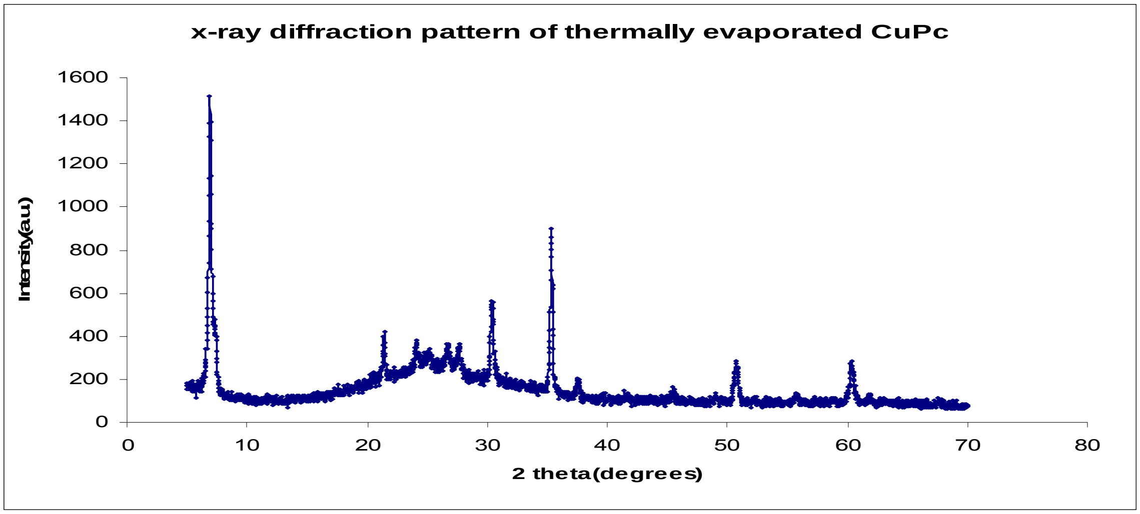

Figure 4.6 XRD of thermally evaporated CuPc film.

The X-ray diffraction pattern of the thermally evaporated CuPc film shows peak at 2Θ position of 6.85^0 as observed by Forrest et al.. The X-ray diffraction pattern of CuPc film is shown in Figure 4.6. The peaks at positions 23^0, 30^0, 35^0,37^0, 45^0, 51^0 and 60^0 are produced by ITO.

4.5 Characterization of TiO_2 by SEM

The TiO_2 sol-gel prepared as described in section 3.1b was spin coated on the surface of the ITO coated glass substrates. The speed of the spincoater was set to 2000 rpm and the duration of the spin was 40 seconds. The substrates were then annealed overnight in a Boekel industries furnace at a temperature of 300°C to increase the adhesion of the films and also for the formation of pores. The macropores formed were of diameter 300 nm. The TiO_2 film was characterized to be nano crystalline in nature. The SEM image of the TiO_2 film at a high magnification is shown in Figure 4.7 and at low magnification is shown in Figure 4.8. The TiO_2 particles were of size 25 nm.

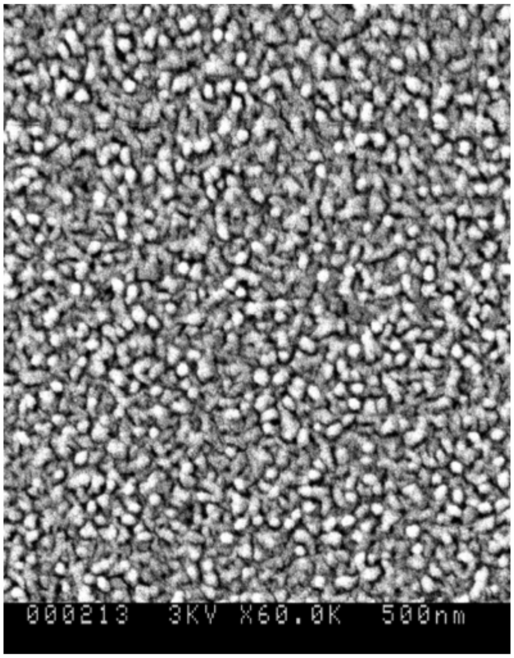

Figure 4.7 SEM image of TiO_2 at high magnification.

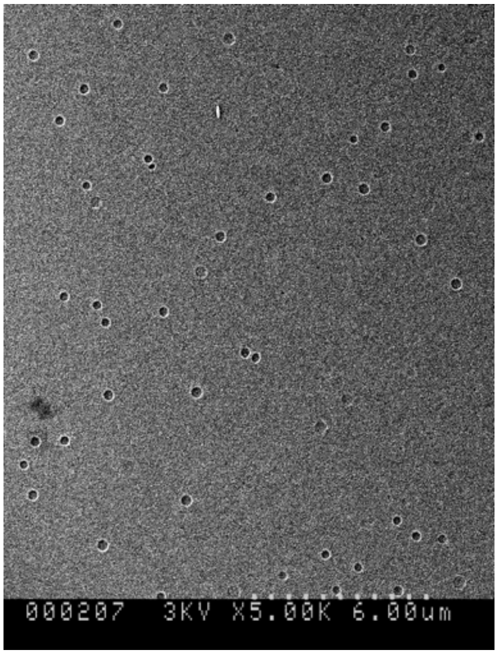

Figure 4.8 SEM image of TiO_2 at low magnification.

Chapter 5. Optical Characterization

5.1 Optical absorption of C_{60}

The optical absorption of C_{60} was measured in the wavelength range of 280-800 nm. Figure 5.1 shows the absorption vs. wavelength plot of the thermally evaporated C_{60} film. The C_{60} film shows peaks of amplitude 2.2 at 350 nm, 0.75 at 450 nm as observed by Tetsuya Taima et al. [4].

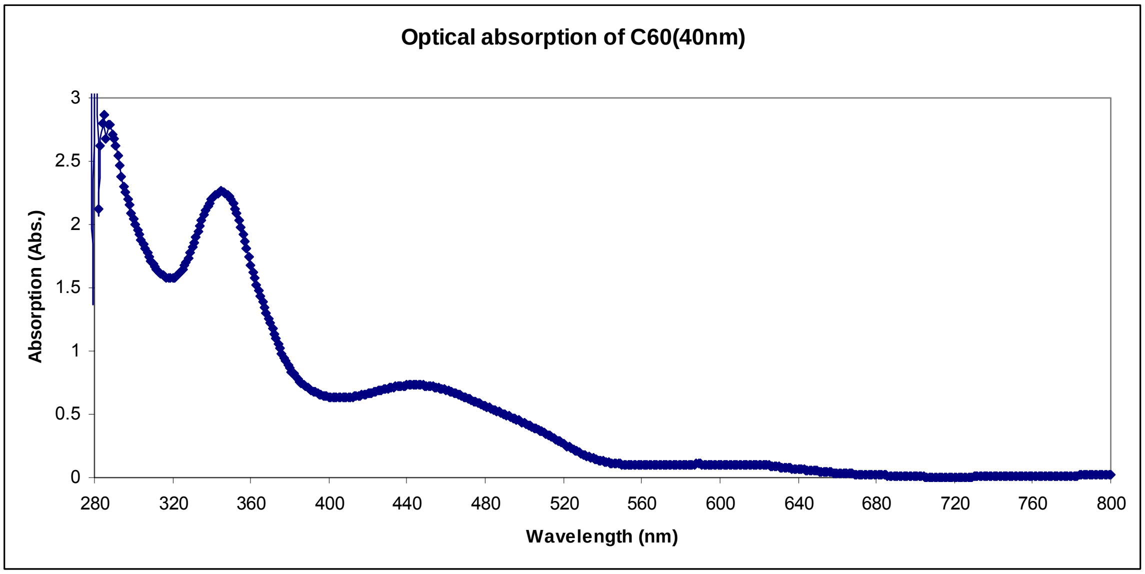

Figure 5.1 Optical absorption of C60(40 nm) film.

5.2 Calculation of Absorption coefficient (α)

Consider a sample of thickness x and let the intensity of light incident on the sample be I_o and let I(x) be the intensity at a distance x in the sample. The relation between δI the decrement in intensity at a small elemental volume δx at x and the intensity of the light at the distance x can be defined by equation 5.1.

$$\delta I = -\alpha\ \delta x\ I(x) \qquad 5.1$$

where α (cm^{-1}) is the absorption coefficient and it depends on the material and photon wavelength.

Solution to equation 5.1 can be obtained by integration and is given by equation 5.2.

$$I(x) = I_o \exp(-\alpha x) \qquad 5.2$$

$$\alpha = (1/t)\ln(I_o/I(x)) \quad 5.3$$

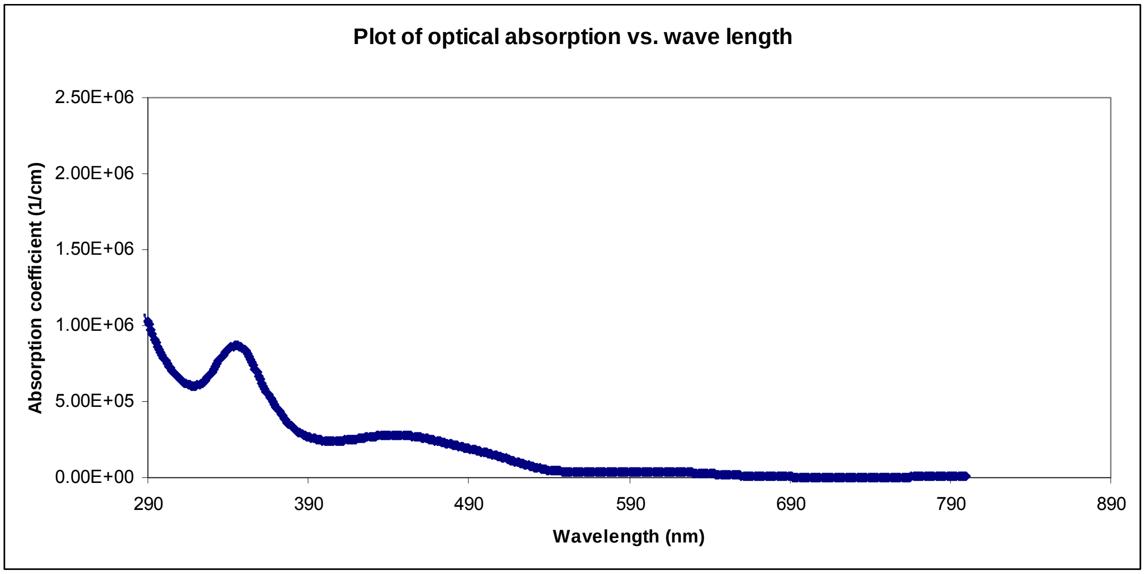

Figure 5.2 Plot of absorption coefficient vs. wavelength for C_{60} film.

Figure 5.2 shows the plot of absorption coefficient vs. wavelength for the C_{60} film.

5.3 Optical absorption of CuPc film of thickness 15 nm

Figure 5.4 shows the optical absorption curve of the CuPc layer of thickness 15nm and Figure 5.5 shows the absorption coefficient vs. wavelength plot for the film.

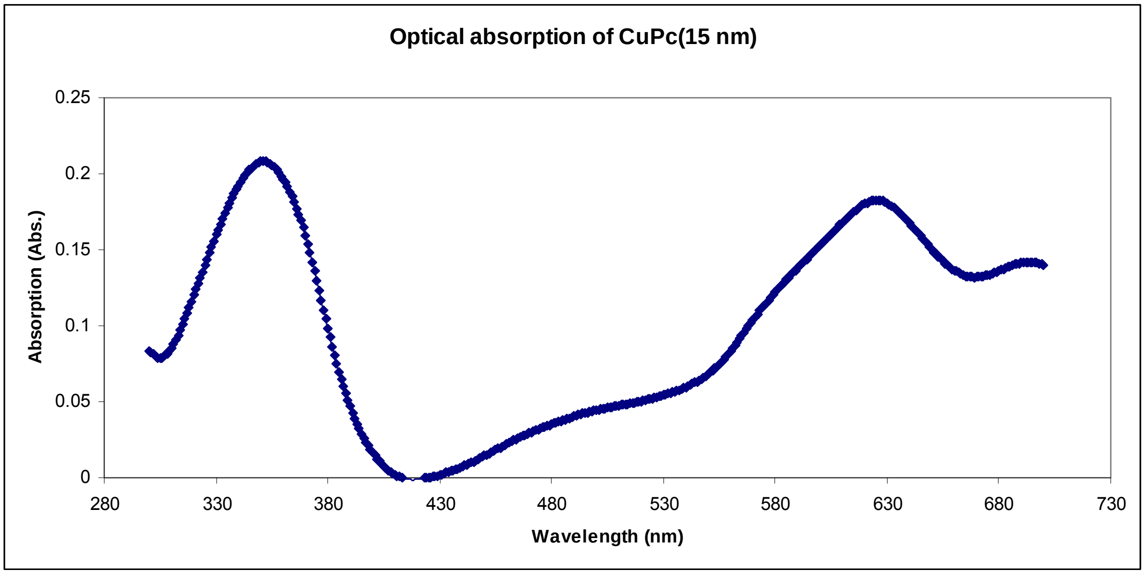

Figure 5.3 Optical absorption of CuPc (15 nm) film.

From Figure 5.4 it can be observed that the CuPc film has absorption peaks at wavelengths of 350 nm, 620 nm and 700 nm as observed by C.Y. Kwong et al. [7]. The values of the arbitrary units of absorption at 350 nm, 620 nm and 700nm are 0.21, 0.19 and 0.15 respectively.

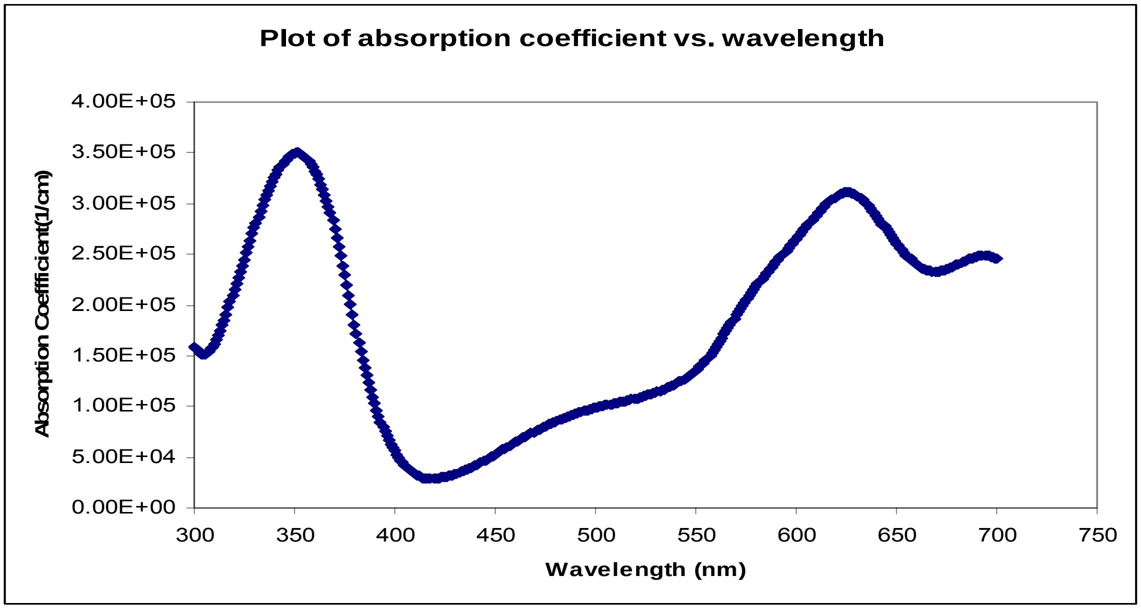

Figure 5.4 Plot of absorption coefficient vs. wavelength for CuPc (15 nm) film.

5.4 Optical absorption of CuPc film of thickness 60 nm

Figure 5.6 shows the optical absorption curve of the CuPc layer of thickness 60 nm and Figure 5.7 shows the absorption coefficient vs. wavelength plot for the film.

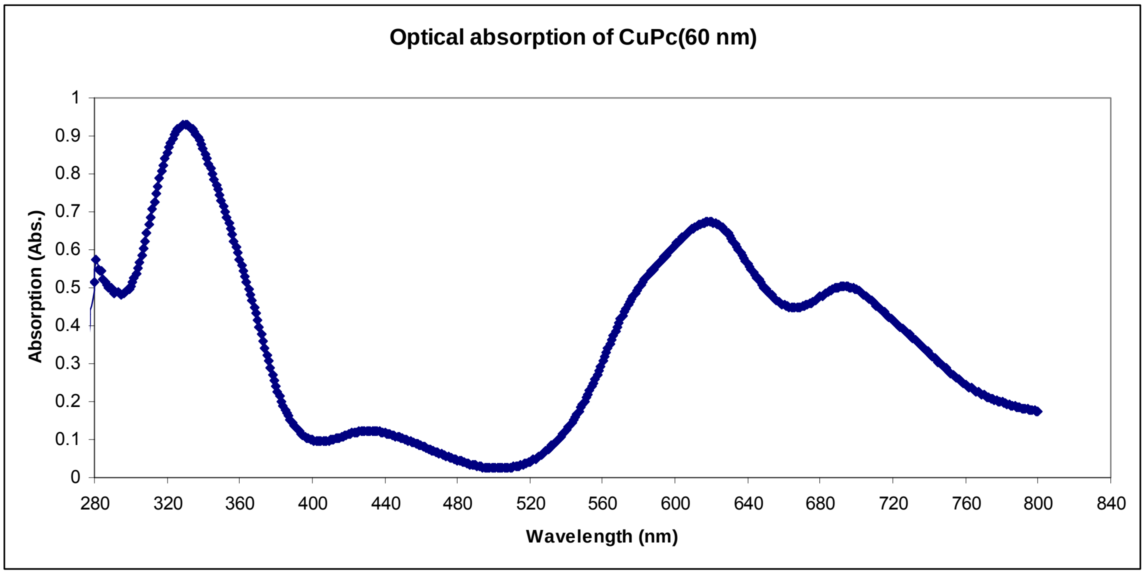

Figure 5.5 Optical absorption of CuPc(60 nm) film.

From Figure 5.6 it can be observed that the CuPc film has absorption peaks at wavelengths of 350 nm, 620 nm and 700 nm as observed by C.Y. Kwong et.al. [7]. The values of the arbitrary units of absorption at 350 nm, 620 nm and 700nm are 0.92, 0.71 and 0.55 respectively

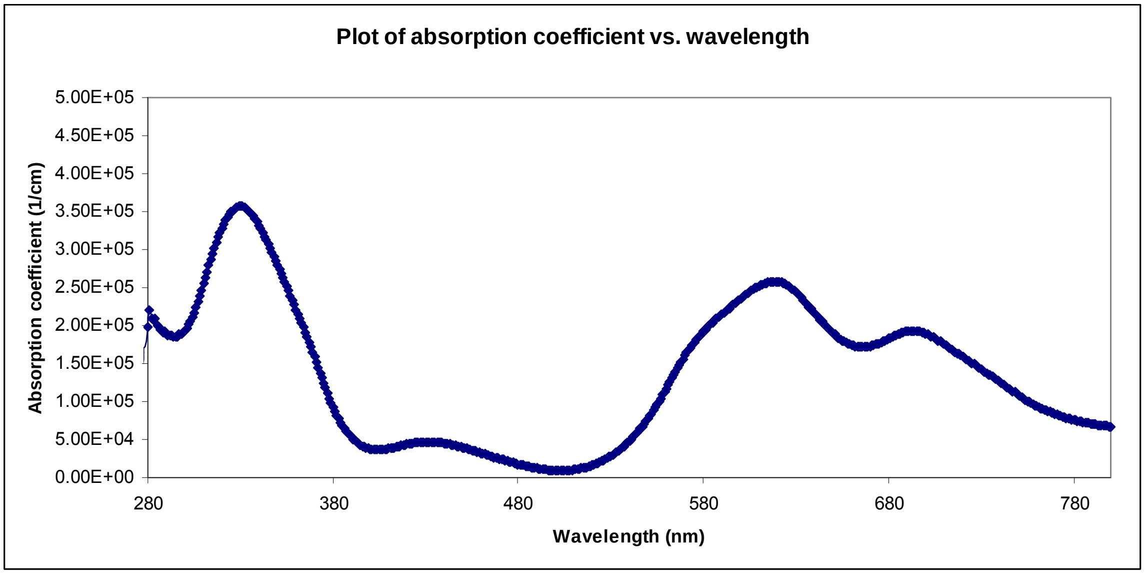

Figure 5.6 Plot of absorption coefficient vs. wavelength for CuPc (60 nm) film.

5.5 Optical absorption of CuPc film of thickness 80 nm

Figure 5.7 shows the optical absorption curve of the CuPc layer of thickness 80 nm and Figure 5.8 shows the absorption coefficient vs. wavelength plot for the film.

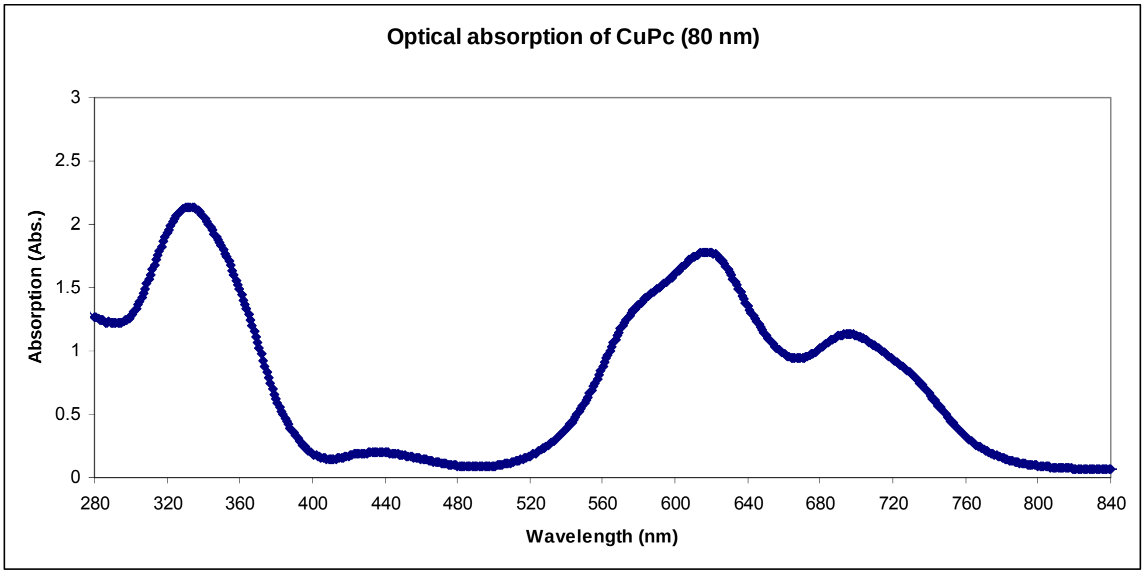

Figure 5.7 Optical absorption of CuPc(80 nm) film.

From Figure 5.8 it can be observed that the CuPc film has absorption peaks at Wavelengths of 350 nm, 620 nm and 700 nm as observed by C.Y. Kwong et.al.. The values of the arbitrary units of absorption at 350 nm, 620 nm and 700nm are 2.2, 1.8 and 1.2 respectively.

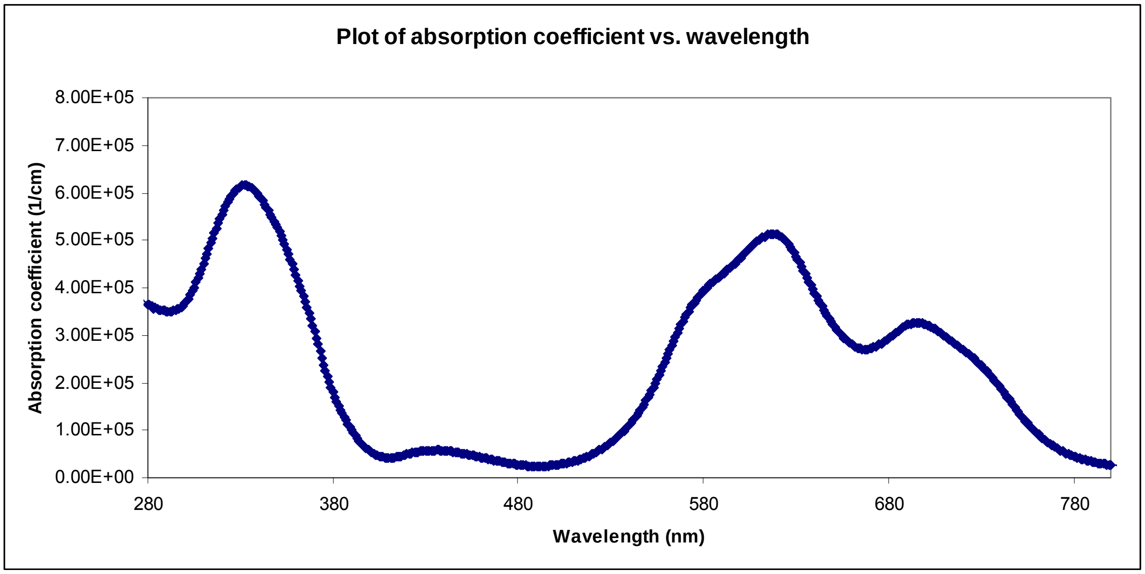

Figure 5.8 Plot of absorption coefficient vs. wavelength for CuPc (80 nm) film.

5.6 Optical absorption of CuPc film of thickness 100 nm

Figure 5.9 shows the optical absorption curve of the CuPc layer of thickness 100 nm and Figure 5.10 shows the absorption coefficient vs. wavelength plot for the film. From Figure 5.9 it can be observed that the CuPc film has absorption peaks at wavelengths of 350 nm, 620 nm and 700 nm. The values of the arbitrary units of absorption at 350 nm, 620 nm and 700nm are 2.5, 2.2 and 1.4 respectively.

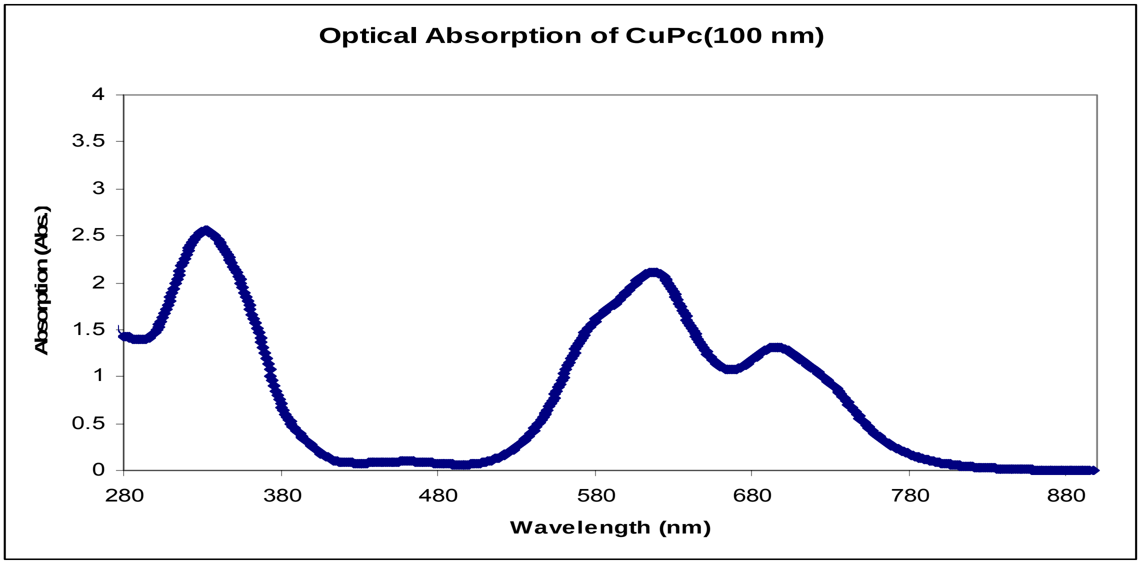

Figure 5.9 Optical absorption of CuPc(100 nm) film.

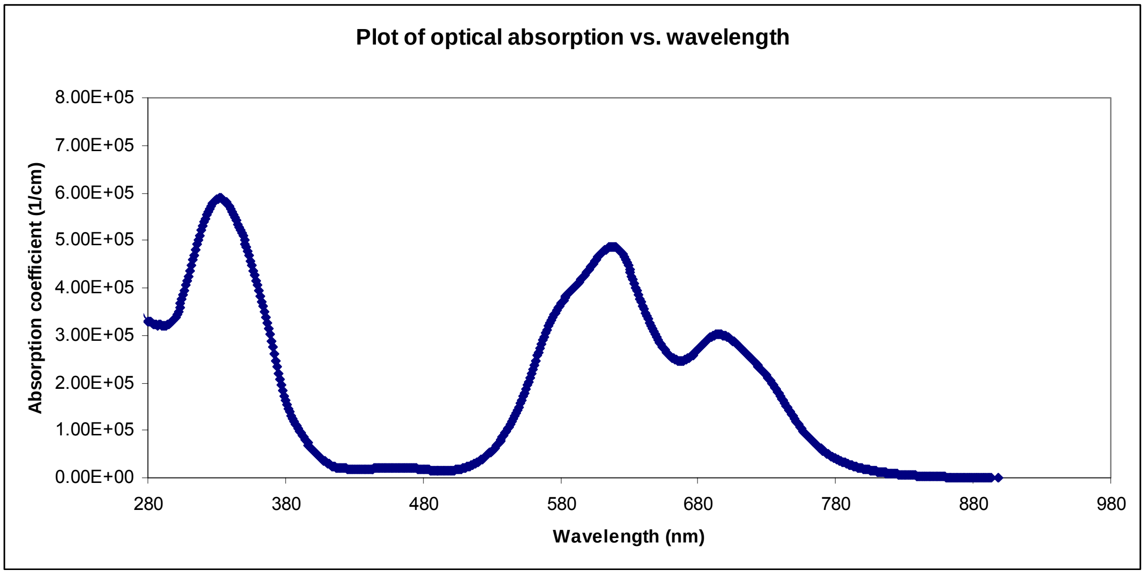

Figure 5.10 Plot of absorption coefficient vs. wavelength for CuPc (100 nm) film.

5.7 Optical absorption of CuPc film of thickness 120 nm

Figure 5.11 shows the optical absorption curve of the CuPc layer of thickness 120 nm and Figure 5.12 shows the absorption coefficient vs. wavelength plot for the film. From Figure 5.11 it can be observed that the CuPc film has absorption peaks at wavelengths of 350 nm, 620 nm and 700 nm. The values of the arbitrary units of absorption at 350 nm, 620 nm and 700nm are 3.5, 3.0 and 1.8 respecticely.

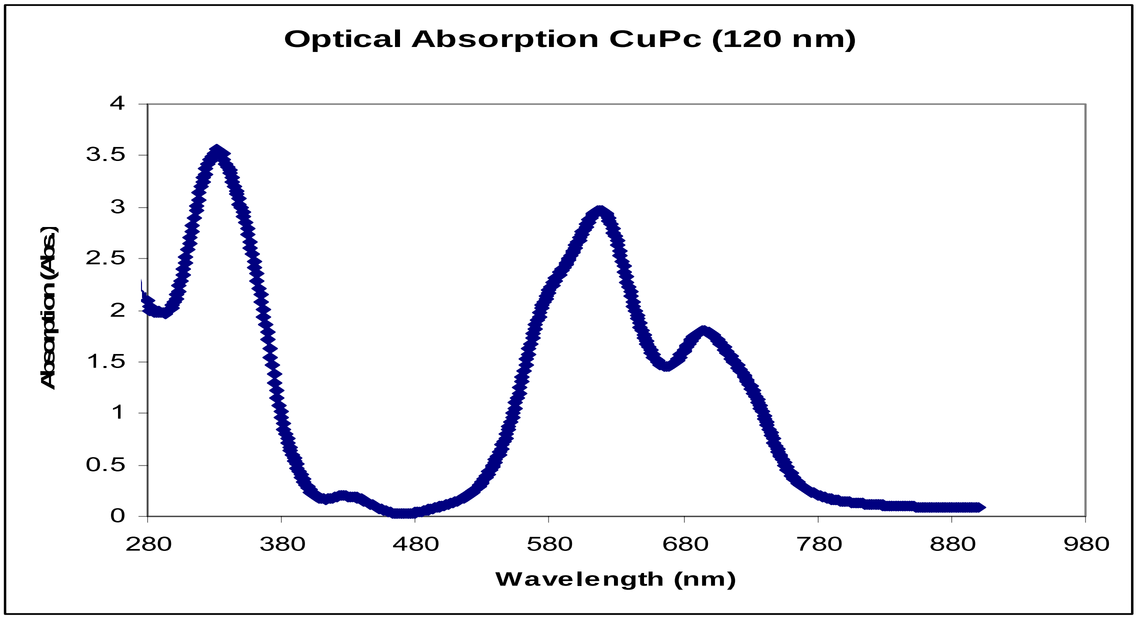

Figure 5.11 Optical absorption of CuPc(120 nm) film.

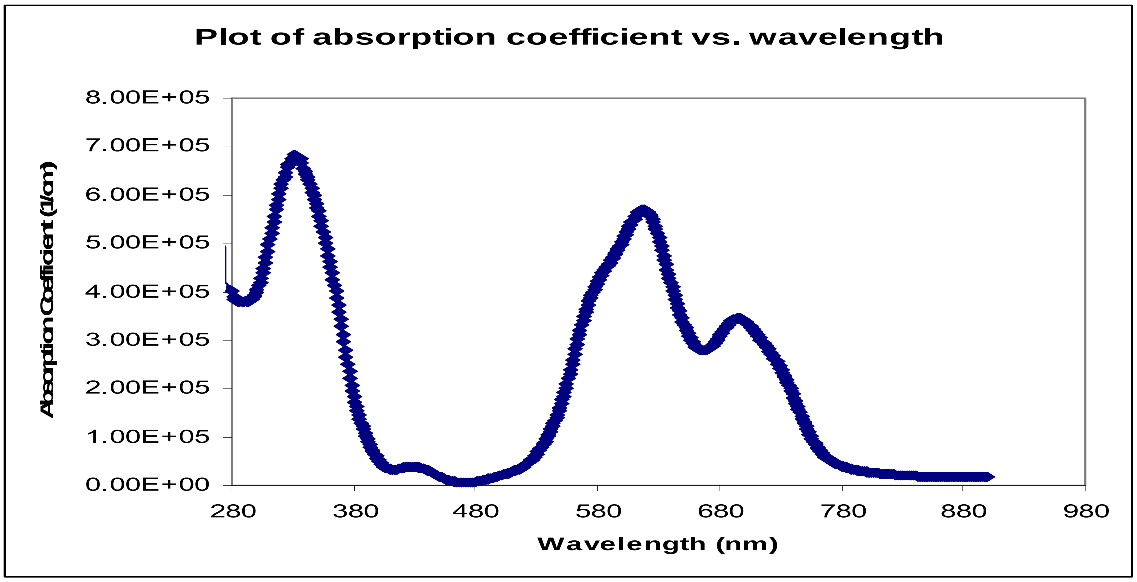

Figure 5.12 Plot of absorption coefficient vs. wavelength for CuPc (120 nm) film.

5.8 Optical absorption of CuPc film of thickness 140 nm

Figure 5.13 shows the optical absorption curve of the CuPc layer of thickness 140 nm and Figure 5.14shows the absorption coefficient vs. wavelength plot for the film. From Figure 5.13 it can be observed that the CuPc film has absorption peaks at wavelengths of 350 nm, 620 nm and 700 nm. The values of the arbitrary units of absorption at 350 nm, 620 nm and 700nm are 4.0, 3.5 and 2.0 respecticely.

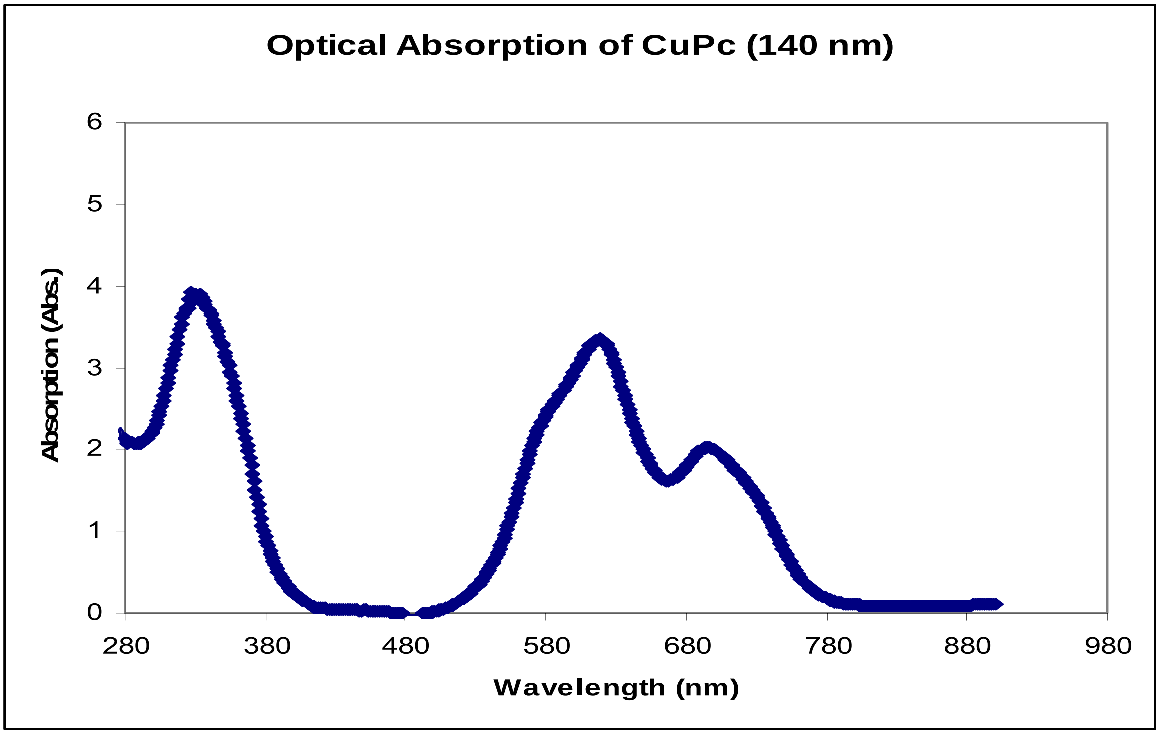

Figure 5.13 Optical absorption of CuPc(140 nm) film.

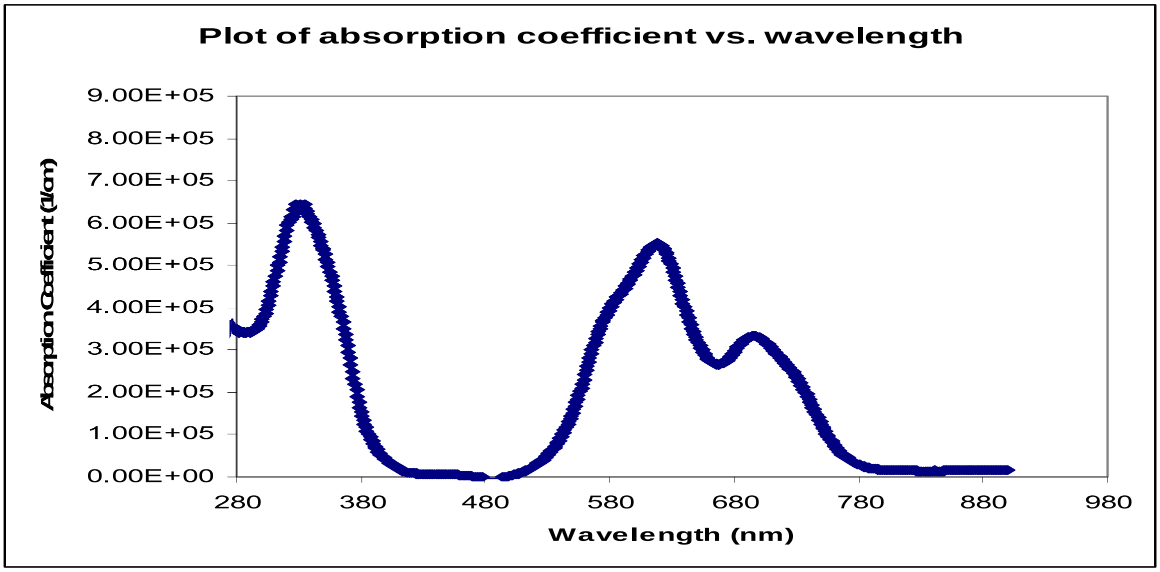

Figure 5.14 Plot of absorption coefficient vs. wavelength for CuPc (140 nm) film.

5.9 Comparision of optical absorption of CuPc films of thickness 15, 60, 80, 100, 120 and 140 nm.

Figure 5.15 shows the comparision of absorption curves of CuPc films of thickness of 15, 60, 80, 100, 120 and 140 nm. Figure 5.16 shows the absorption coefficient vs. wavelength plot for the CuPc films. As expected the absorbance of the CuPc films increased with the thickness of the film.

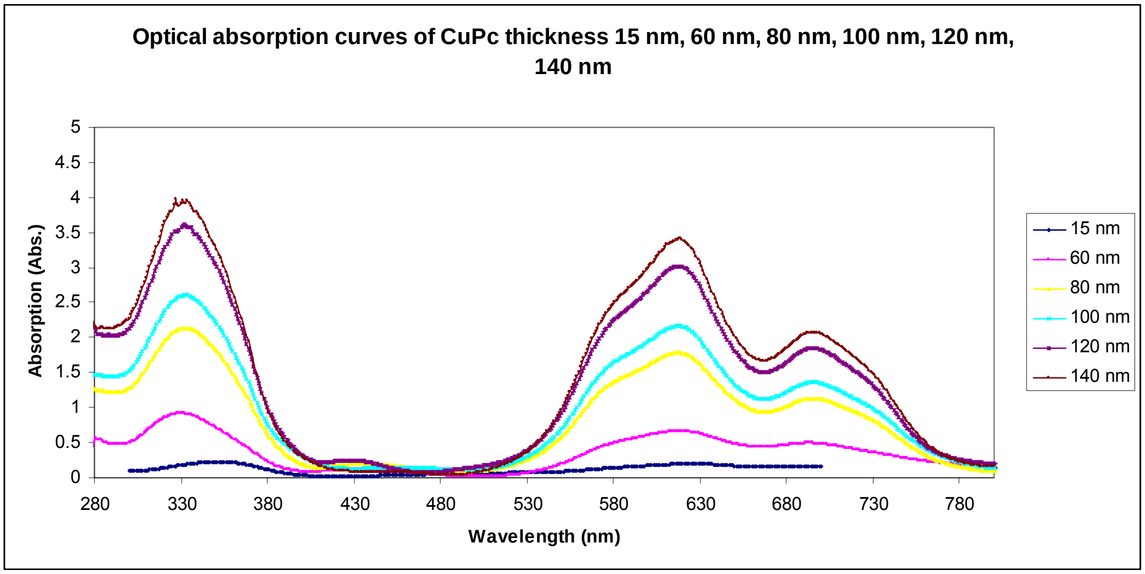

Figure 5.15 Optical absorption of CuPc films with thickness 15, 60, 80, 100, 120, 140 nm.

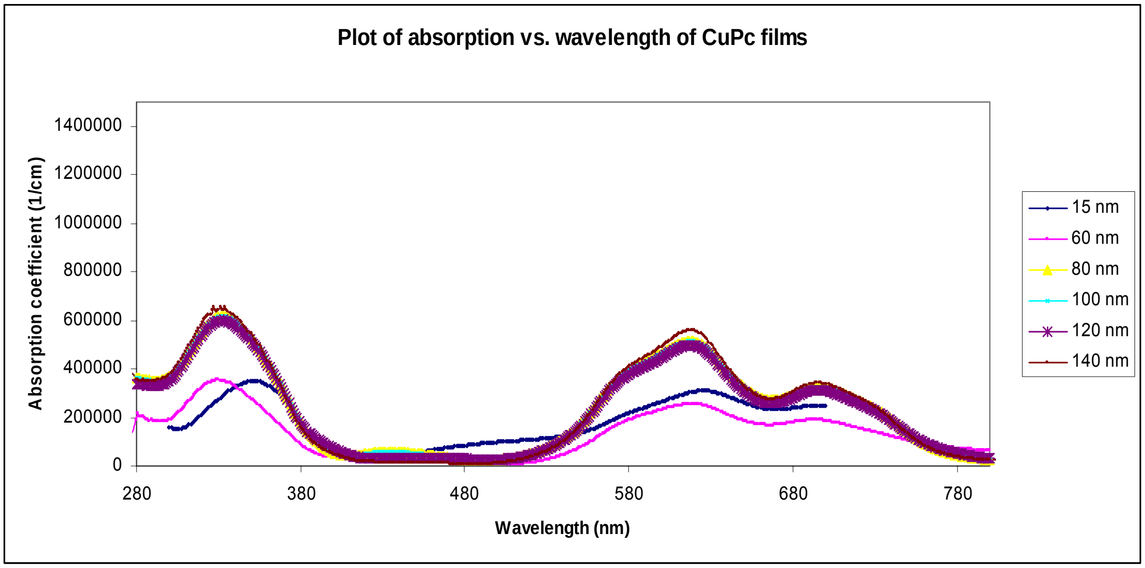

Figure 5.16 Plot of absorption coefficient vs. wavelength for CuPc films with thickness 15, 60, 80, 100, 120, 140 nm.

5.10 Optical absorption of 4 times spin coated TiO_2 film of thickness 30 nm.

Figure 5.17 shows the optical absorption of the 4 times spin coated TiO_2 film of thickness 30 nm and Figure 5.18 shows the absorption coefficient vs. wavelength plot for the same film. It can be seen from Figure 5.17 that the TiO_2 film has a absorption peak of amplitude 0.08 at 500 nm and 0.18 at 300 nm.

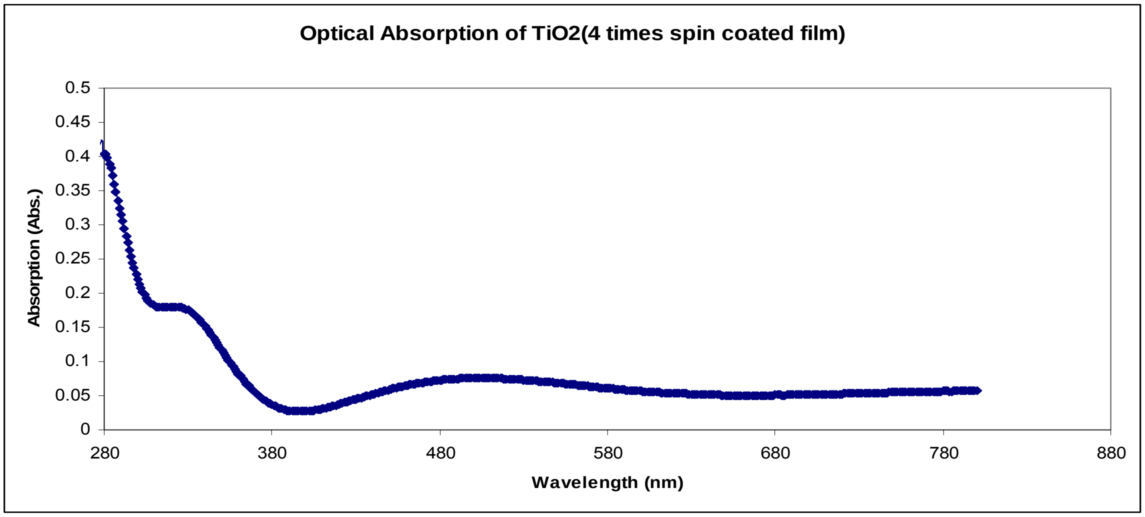

Figure 5.17 Optical absorption of TiO_2 (4 times spin coated) film.

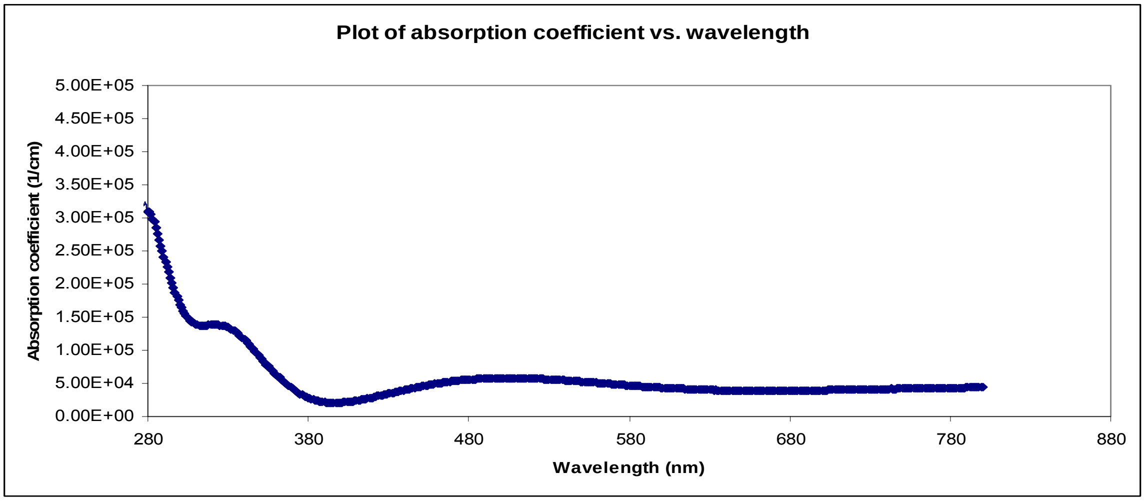

Figure 5.18 Plot of absorption coefficient vs. wavelength for TiO_2 (4 times spin coated) film.

5.11 Optical absorption of CuPc (15 nm) on top of 4 times spin coated TiO_2 film of thickness 30 nm.

Figure 5.19 shows the optical absorption of CuPc(15 nm) on top of 4 times spin coated TiO_2 film of thickness 30 nm and Figure 5.20 shows the absorption coefficient vs. wavelength plot for the same film. It can be seen from Figure 5.19 that the film has a absorption peaks of amplitude 0.4 at 360 nm, 0.4 at 630 nm and 0.38 at 700 nm.

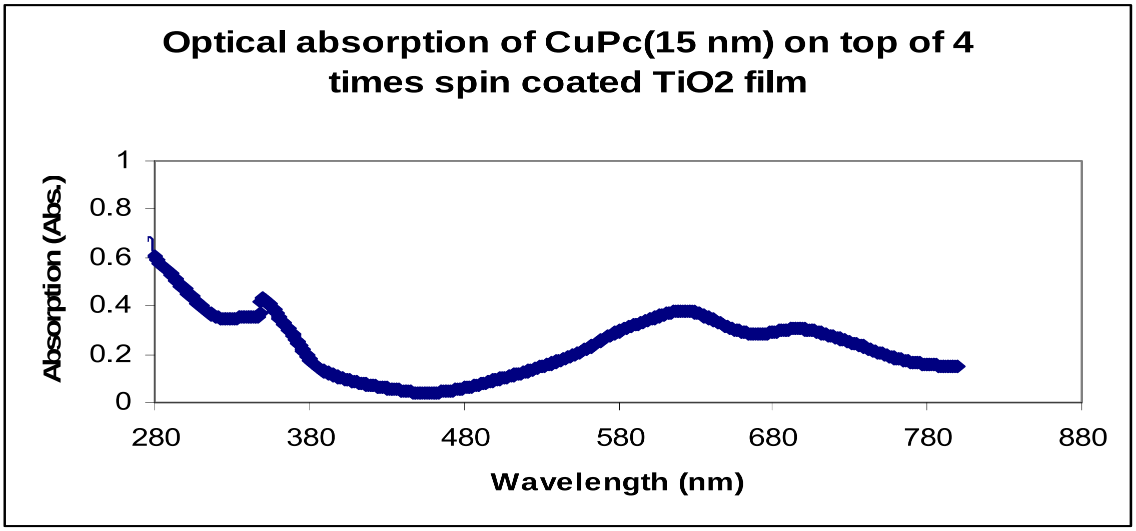

Figure 5.19 Optical absorption of CuPc(15 nm) on top of TiO_2 (4 times spin coated) film.

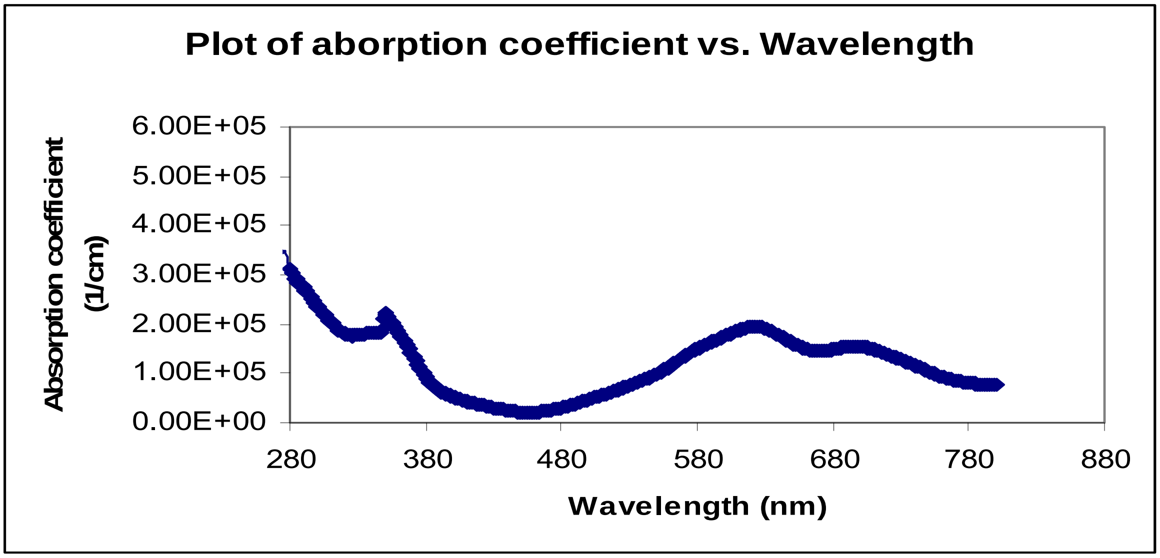

Figure 5.20 Plot of absorption coefficient vs. wavelength for CuPc(15 nm) on top of TiO_2 (4 times spin coated) film.

Chapter 6. Electrical Characterization

6.1 J-V Characterisitcs

The J-V characteristics of the devices were measured by applying a voltage across the device, with positive polarity to ITO and negative polarity to aluminium(Al).

The behavior of these devices is similar to that of an abrupt p-n junction. The J-V characteristics of such devices are usually governed by the "ideal diode equation" in an ideal case.

$$J = J_O\left[\exp\left(\frac{qV}{nkT}\right) - 1\right] \tag{6.1}$$

where J_o = reverse saturation current density

q = charge of electron = 1.6×10^{-19} C

k = Boltzmann constant = 1.38×10^{-23} $J.K^{-1}$

n = ideality factor of the diode

T = Absolute temperature in degree Kelvin.

According to equation 6.1 for an ideal diode,

1. The diffusion and drift current ($-J_o$) currents balance at zero bias (V=0), canceling each other and resulting in an absence of net current flow.
2. In forward bias, the barrier decreases, diffusion current increases exponentially and the drift current is unaltered.
3. In the reverse bias the barrier increases, diffusion current is negligible and drift current is unaltered.

In some real world cases the ideal diode equation may not be applicable due to the effects of series resistance, leakage current and other factors. In such cases equation 6.1 should be modified.

6.2 Series Resistance (R_s)

Series resistance is the resistance caused by quasi neutral regions and the contacts made to the device. In a device which shows a series resistance, the potential drop is attributed both to the junction and to the series resistance (R_s). The potential drop associated with the series resistance (R_s) needs to be separated from the applied potential so that the J-V characteristics can be corrected and the current component of the diode behavior is extracted.

Equation 6.1 would then be modified to equation 6.2

$$J = J_O\left[\exp\left(\frac{q(V - JRs)}{nkT}\right) - 1\right] \qquad 6.2$$

where Rs is the series resistance and therefore the potential drop across junction is calculated by V-JRs. Rs can then be calculated mathematically from the J-V Characteristics.

On differentiating equation 6.2 we get,

$$1 = Jo\frac{q}{nkT}\left(\frac{dV}{dJ} - Rs\right)\exp\left[\frac{q(V - JRs}{nkT}\right]$$

So,

$$\frac{dV}{dJ} = \frac{nkT}{qJo}\exp\left[\frac{-q}{nkT}(V - JRs)\right] + Rs \qquad 6.3$$

Again, from equation 6.2 and ignoring a Jo term, we can rewrite equation 6.3 as,

$$\frac{dV}{dJ} = \frac{nkT}{qJ} + Rs \qquad 6.4$$

When the applied bias is high, the current through the device would also be large. The first term in equation 6.4 would be negligible in this case. So at a higher bias the series resistance can be estimated with the slope of the J-V curve.

6.3 Ideality Factor(n) and Reverse Saturation Current Density(J_o)

Taking the natural logarithm of equation 6.1 we get,

$$\ln(J) = \ln(Jo) + \frac{qV}{nkT} \qquad 6.5$$

The slope of the above equation is q/nkT. The ideality factor n can be computed from the slope of the straight line. For an ideal diode, the value of n is 1 and the slope of the ln(J) vs. V plot is q/Kt. In real situations, the value of n deviates from 1 due to processes such as high injection and tunneling of carriers between states in the bandgap. The value of reverse saturation current density can be calculated from the value of y-intercept of the ln(J) vs. V plot.

6.4 J-V Characteristics of C_{60}(40 nm)/Al Schottky diode solar cell

The C_{60} (40 nm) Schottky diode solar cell consists Glass/ITO/C_{60} (40 nm)/LiF/Al. In this structure the C_{60}/Al forms the Schottky junction. Figure 6.1 shows the dark curve measured for device. The thickness of the LiF (Lithium fluoride) layer deposited was 1 nm. LiF was shown to improve the fill factor and efficiency of the devices by Christoph J. Brabec et al. [18]. LiF also shields the organic layer from high energy Al atoms.

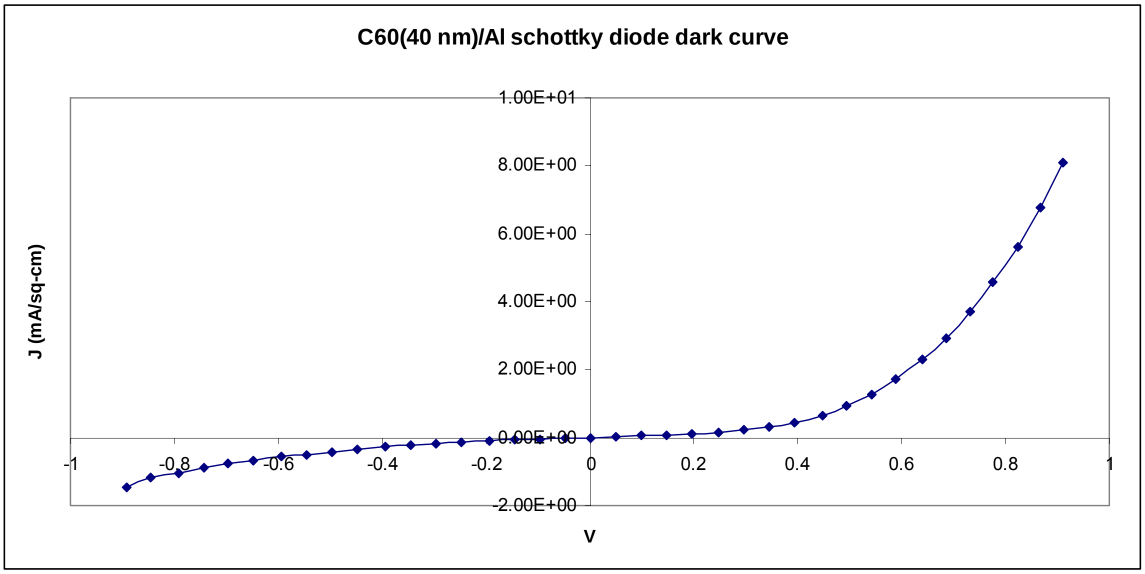

Figure 6.1 Glass/ITO/C_{60}(40 nm)/LiF/Al Schottky diode solar cell dark curve.

The J-V characteristic was obtained by sweeping the voltage from -1 V to +1 V and measuring the resulting current. The aluminium metal contacts were 0.07 cm^2 in area. The slope of the curve at higher voltages can be approximated as the series resistance of the device. The series resistance(R_s) of the curve in Figure 6.1 was calculated to be 78.06 Ω/cm^2. The J-V characteristic was then corrected for series resistance by subtracting JR_s from V. Figure 6.2 shows the plot of V vs. J and ($V-JR_s$) vs. J.

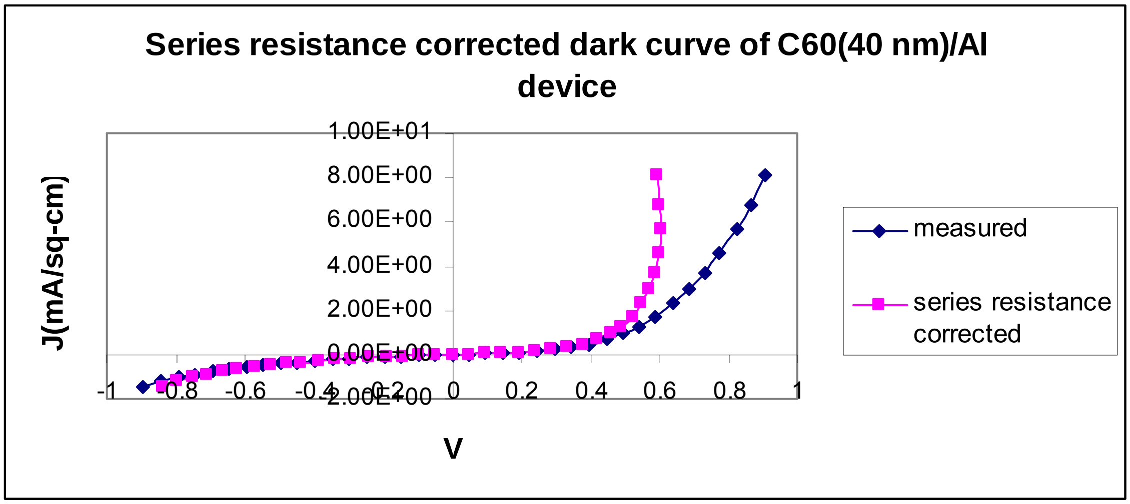

Figure 6.2 Series resistance corrected dark curve for C_{60} (40 nm)/Al device.

The reverse saturation current density $J_{0,}$ and the diode ideality factor n, were obtained from the plot of ln(J) vs. V (Figure 6.3). The value of J_0 was calculated from the y-intercept of the tangent drawn to the ln(J) vs. V plot, and it was found to be 0.019 mA/cm^2. The ideality factor was calculated to be 5.73. The slope of the curve shown in Figure 6.1 in reverse bias conditions can be attributed to the shunting paths between the metal contact and the C_{60}.

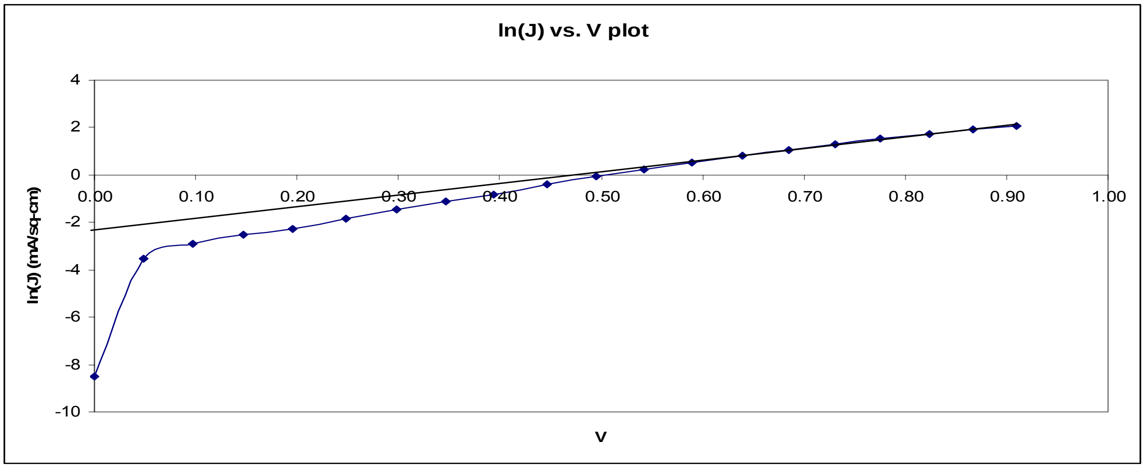

Figure 6.3 ln(J) vs. V plot for determining n and J_0 of C_{60} (40 nm)/Al device dark curve.

Figure 6.4 shows the J-V characteristics of the device Glass/ITO/PEDOT:PSS/C_{60}(40 nm)/LiF/Al under illumination. The series resistance, ideality factor and reverse saturation current were computed to be 63.08 Ω/cm^2, 11.2 and 0.045 mA/cm^2 respectively.

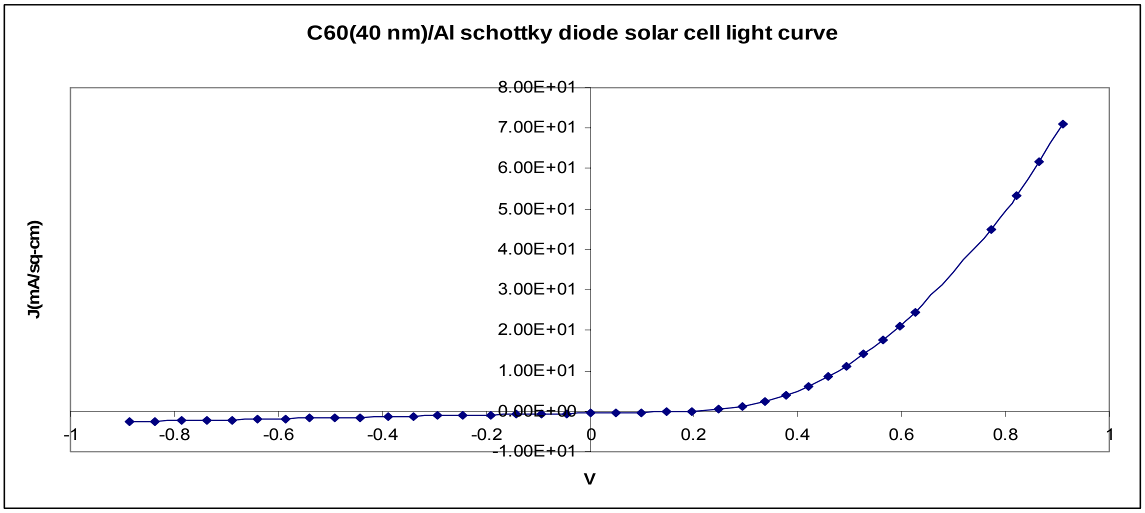

Figure 6.4 Glass/ITO/C_{60}(40 nm)/LiF/Al Schottky diode solar cell light curve.

Figure 6.5 and 6.6 show the series resistance corrected and ln(J) vs. V plot respectively for the light curve.

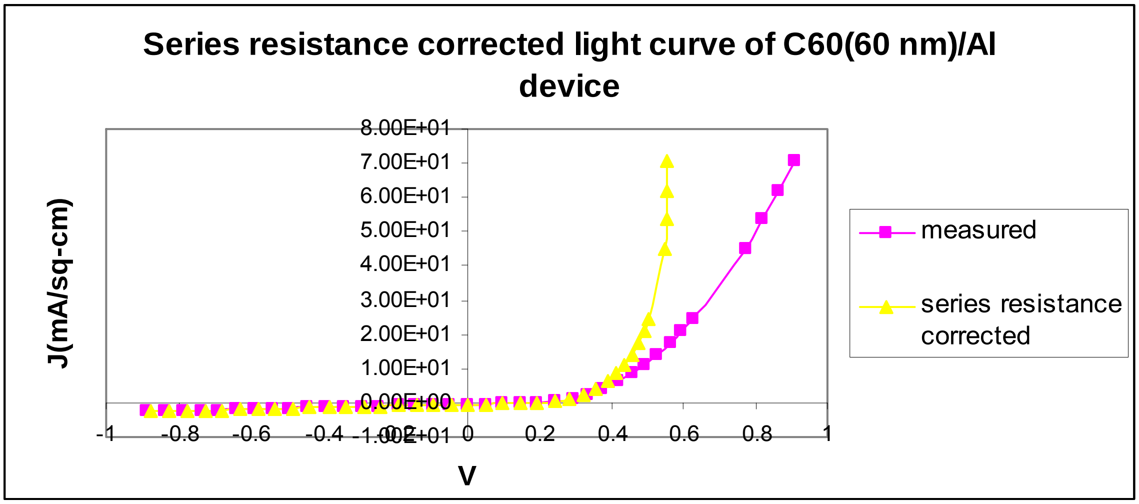

Figure 6.5 Series resistance corrected light curve for C_{60}(40 nm)/Al device.

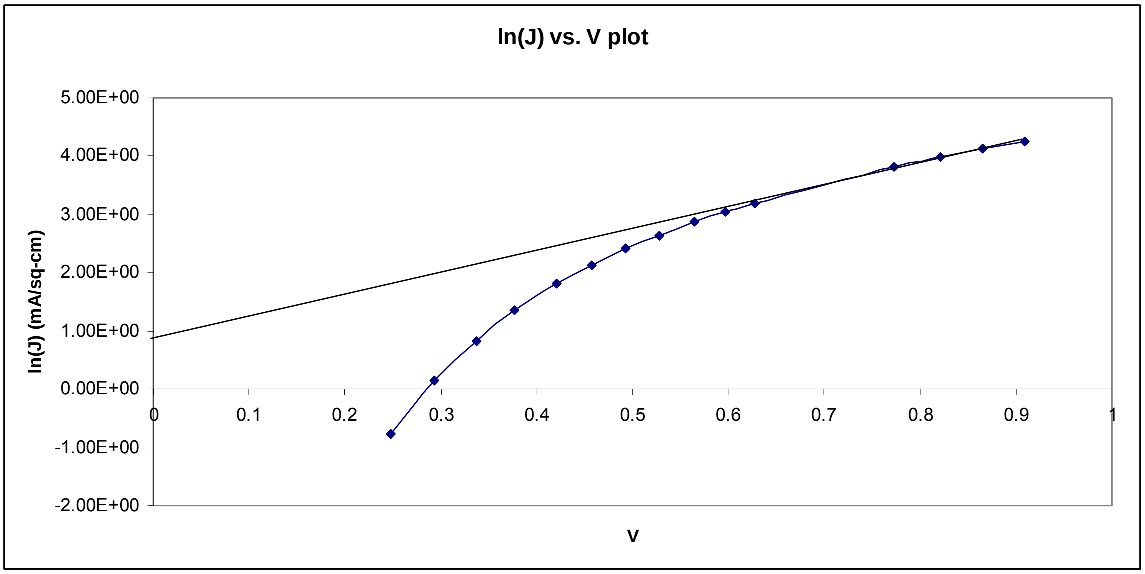

Figure 6.6 ln(J) vs. V plot for determining n and J_0 of C_{60}(40 nm)/Al device light curve.

The Glass/ITO/PEDOT:PSS/C_{60}(40 nm)/LiF/Al cell yielded a V_{oc} and J_{sc} of 190 mV and 0.49 mA/cm^2 respectively. The power delivered was 0.021 mW/cm^2 and the fill factor was .30. The cell had an efficiency of 0.021 %.

6.5 J-V Characteristics of C_{60}(60 nm)/Al Schottky diode solar cell

The C_{60} (60 nm) Schottky diode solar cell consists Glass/ITO/PEDOT:PSS/C_{60}(60 nm)/LiF/Al. In this structure, the C_{60}/Al forms the Schottky junction. It has been observed that the introduction of a thin layer of PEDOT:PSS on the ITO surface acts to smooth the surface of ITO. Figure 6.7 shows the dark curve measured for device.

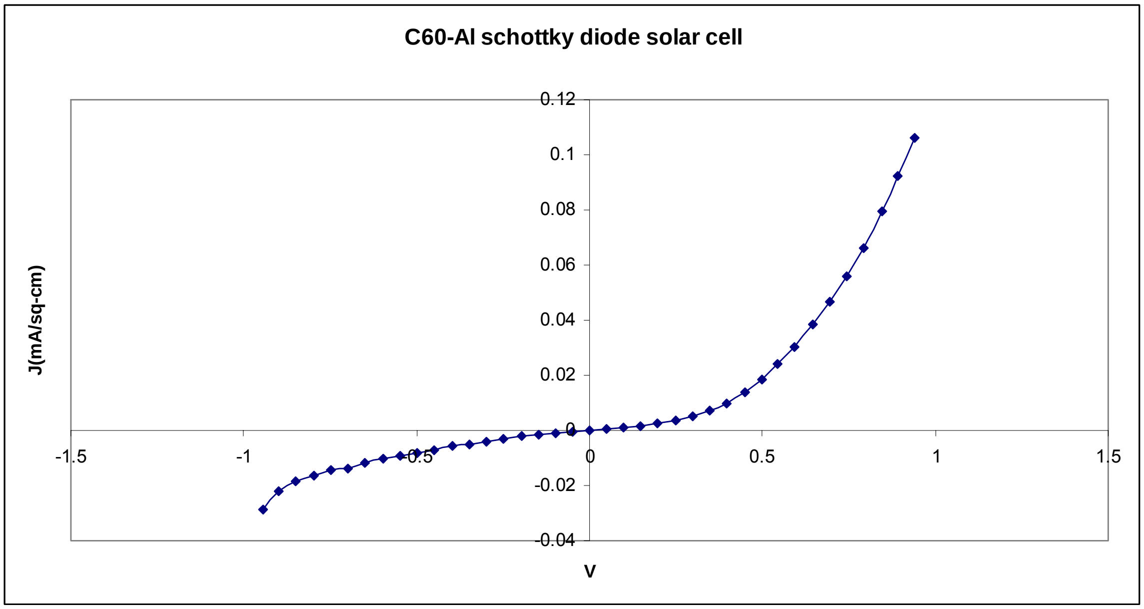

Figure 6.7 Glass/ITO/PEDOT:PPS/C_{60}(60 nm)/LiF/Al Schottky diode solar cell dark curve.

The J-V characteristic was obtained by sweeping the voltage from -1 V to +1 V and measuring the resulting current. The aluminium metal contacts were 0.07 cm^2 in area. The slope of the curve at higher voltages can be approximated as the series resistance of the device. The series resistance(R_s) of the curve in Figure 6.7 was calculated to be 0.75 $k\Omega/cm^2$. The J-V characteristic was then corrected for series resistance by subtracting JR_s from V. Figure 6.8shows the plot of V vs. J and ($V-JR_s$) vs. J.

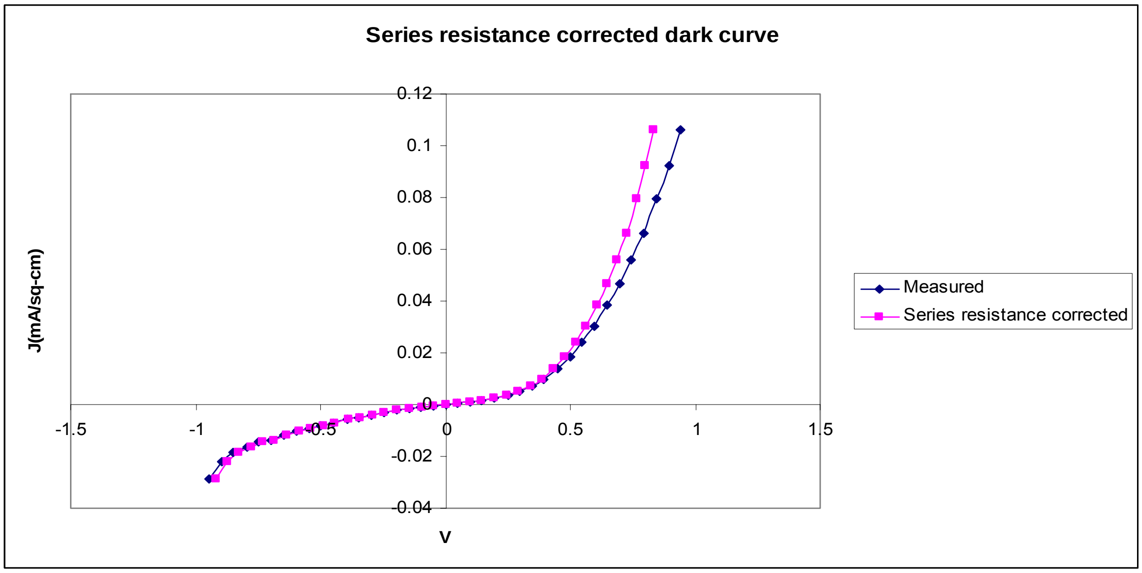

Figure 6.8 Series resistance corrected dark curve for C_{60}(60 nm)/Al device.

The reverse saturation current density J_0, and the diode ideality factor n, were obtained from the plot of ln(J) vs. V(Figure 6.9). The value of J_0 was found to be 0.047 mA/cm^2. The ideality factor was calculated to be 13.

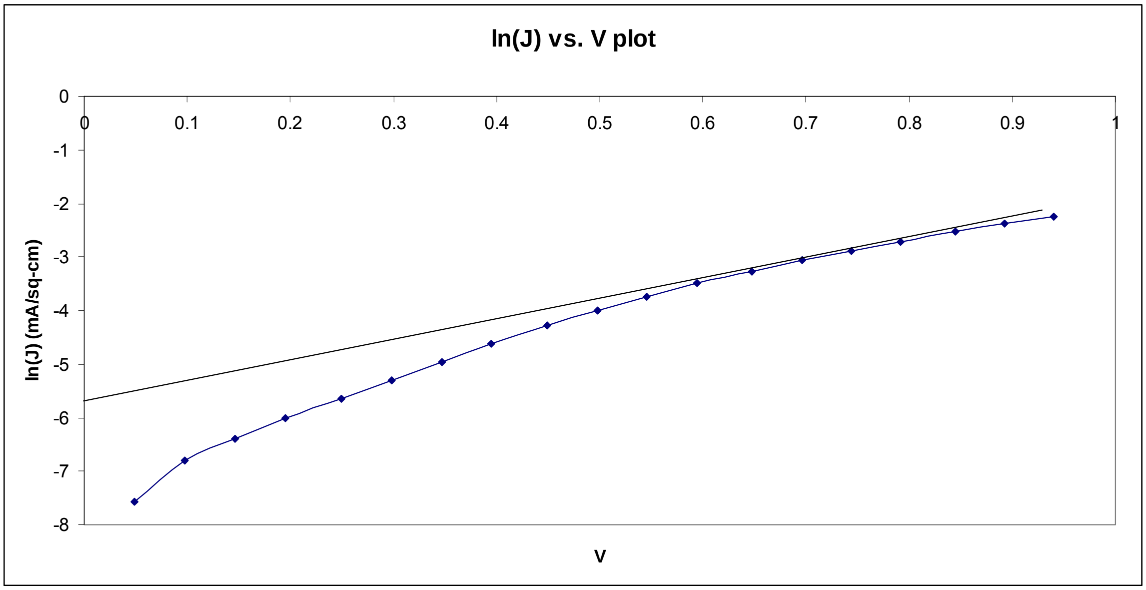

Figure 6.9 ln(J) vs. V plot for determining n and J_0 of C_{60}(60 nm)/Al device dark curve.

Figure 6.10 shows the J-V characteristics of the device Glass/ITO/PEDOT:PSS/C_{60}(60 nm)/LiF/Al under illumination. The series resistance, ideality factor and reverse saturation current were computed to be 0.12 kΩ/cm^2, 12.7 and 0.013 mA/cm^2 respectively.

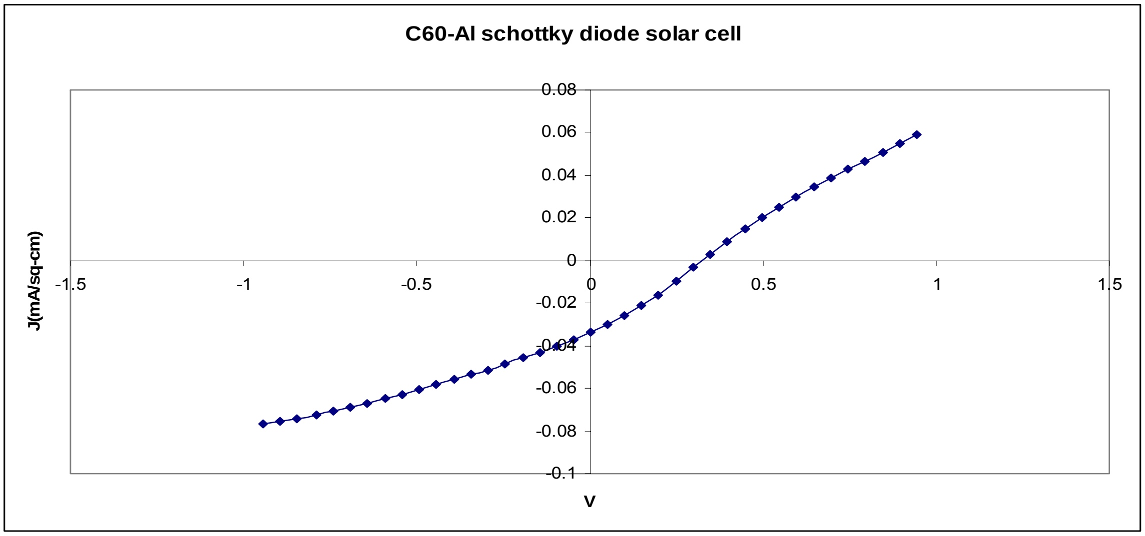

Figure 6.10 Glass/ITO/PEDOT:PPS/C_{60}(60 nm)/Al Schottky diode solar cell light curve.

Figure 6.11 and 6.12 show the series resistance corrected and ln(J) vs. V plot respectively for the light curve.

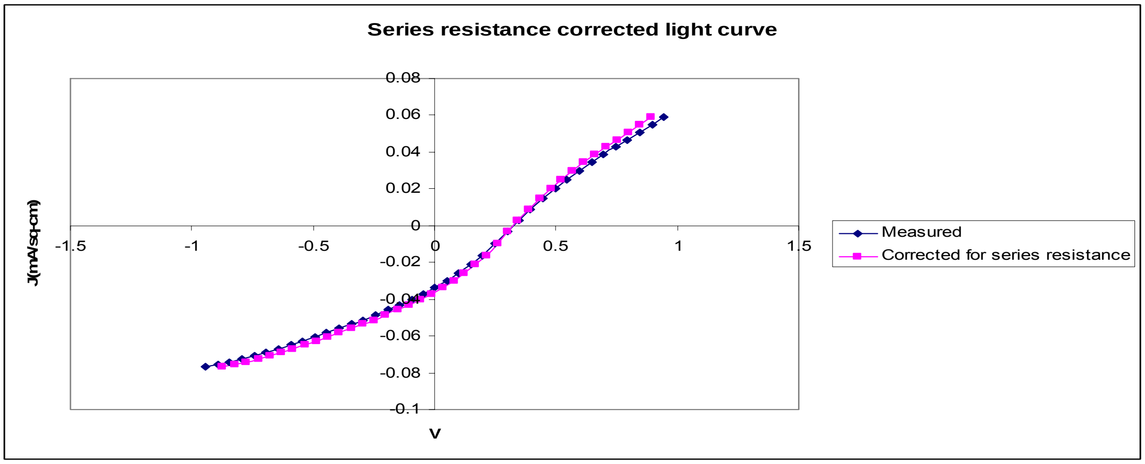

Figure 6.11 Series resistance corrected light curve for C_{60}(60 nm)/Al device.

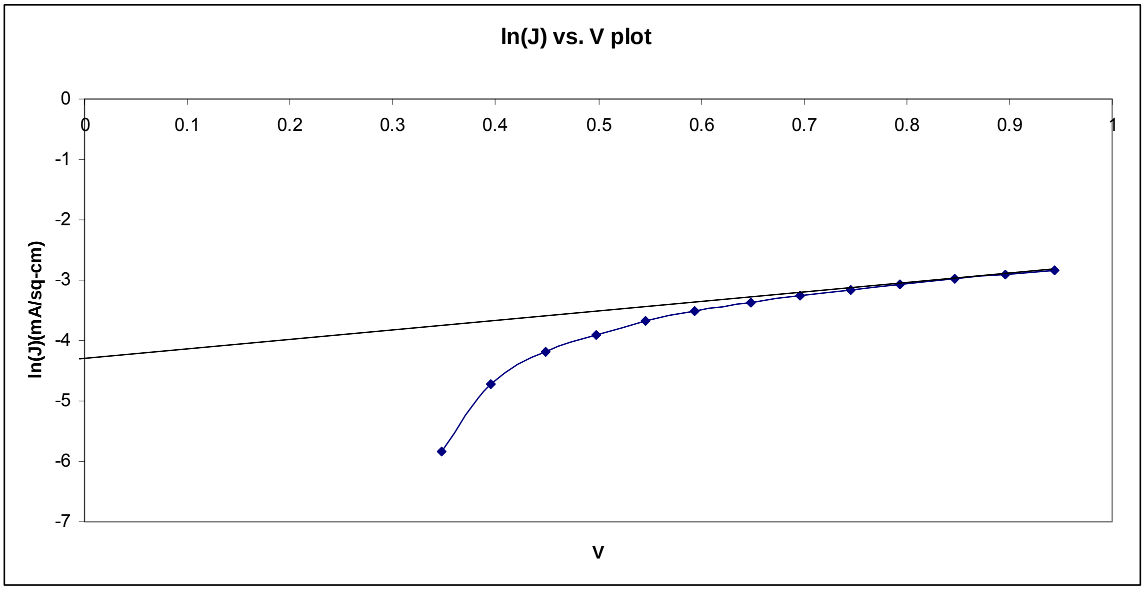

Figure 6.12 ln(J) vs. V plot for determining n and J_0 of C_{60}(60 nm)/Al device light curve.

The Glass/ITO/PEDOT:PSS/C_{60}(60 nm)/LiF/Al cell yielded a V_{oc} and J_{sc} of 310 mV and 0.048 mA/cm^2 respectively. The power delivered was 0.028 mW/cm^2 and the fill factor was 0.35. The cell had an efficiency of 0.028 %.

Structure	Series Resistance (R_s)	Ideality Factor (n)	J_o (mA/cm^2)
ITO/C_{60}(40 nm)/LiF/Al	78.06 Ω/cm^2	5.73	0.019 mA/cm^2
ITO/PEDOT:PSS/C_{60}(60 nm)/LiF/Al	0.75 kΩ/cm^2	13	0.047 mA/cm^2

Table 6.1 Results of C_{60} Schottky diode solar cell dark curves.

Table 6.1 indicates the variation of series resistance (R_s), ideality factor (n) and reverse saturation current density (J_o) of the C_{60} Schottky diode solar cell dark curves. It can be observed from Table 6.1 that there is an increase in the series resistance from 40 nm device to the 60 nm device which can be attributed to the low carrier mobility of PEDOT:PSS layer. The availability of shunting paths between the metal contact and the ITO surface in the case of the 40 nm device and the metal contact and the PEDOT:PSS layer in case of the 60 nm device can be the reason for the curves having a slope in the reverse bias conditions.

Structure	**R_s**	**n**	**J_o**	**V_{oc}**	**J_{sc}**	**F.F.**	**P. D.**	**η**
ITO/C_{60}(40 nm)/LiF/Al	63.08 Ω/cm^2	11.2	0.045 mA/cm^2	190 mV	0.49 mA/cm^2	0.30	0.021 mW/cm^2	0.021%
ITO/PEDOT:PSS/C_{60}(60 nm)/LiF/Al	0.12 kΩ/cm^2	12.7	0.013 mA/cm^2	310 mV	0.48 mA/cm^2	0.35	0.028 mW/cm^2	0.028%

Table 6.2 Results of C_{60} Schottky diode solar cell light curves.

Table 6.2 indicates the variation of series resistance (R_s), ideality factor (n), reverse saturation current density (J_o), open circuit voltage (V_{oc}), short circuit current (J_{sc}), fill factor, power delivered by the cell and the efficiency of the cell. As in the case of dark curves the series resistance of the cells under illumination also increased due to the inclusion of PEDOT:PSS layer in case of the 60 nm device. The high reverse saturation currents suggest the presence of physical shunting paths. PEDOT:PSS was included to smooth out the irregularities in the ITO surface which in turn leads to the formation of a uniform C_{60} film. With the increase in the thickness of the C_{60} layer the open circuit voltage (V_{oc}) increases by 120 mV. This increase in V_{oc} can be attributed to the increase in the absorption of C_{60} film when the thickness is increased from 40 nm to 60 nm. In case of the short circuit current (J_{sc}) we did not observe much change and this can be attributed to the increase in the series resistance from 40 nm to 60 nm device. We observed an increase in the fill factor, power delivered and efficiency in case of the 60 nm device. The high diode ideality factors indicate several transport mechanisms like recombination-generation currents in the depletion region and recombination through interface states at the junction.

6.6 J-V Characteristics of CuPc/Al Schottky diode solar cells

The CuPc/Al Schottky diode solar cell consists of Glass/ITO/PEDOT:PSS/CuPc (x)/Al where x is the thickness of the CuPc layer and its values are 15 nm, 60 nm, 80 nm, 100 nm, 120 nm, 140 nm.

6.6.1 J-V characteristics of CuPc(15 nm)/Al device

In this structure the CuPc/Al forms the Schottky junction. Figure 6.13 shows the dark curve measured for device in which the CuPc thickness is 15 nm.

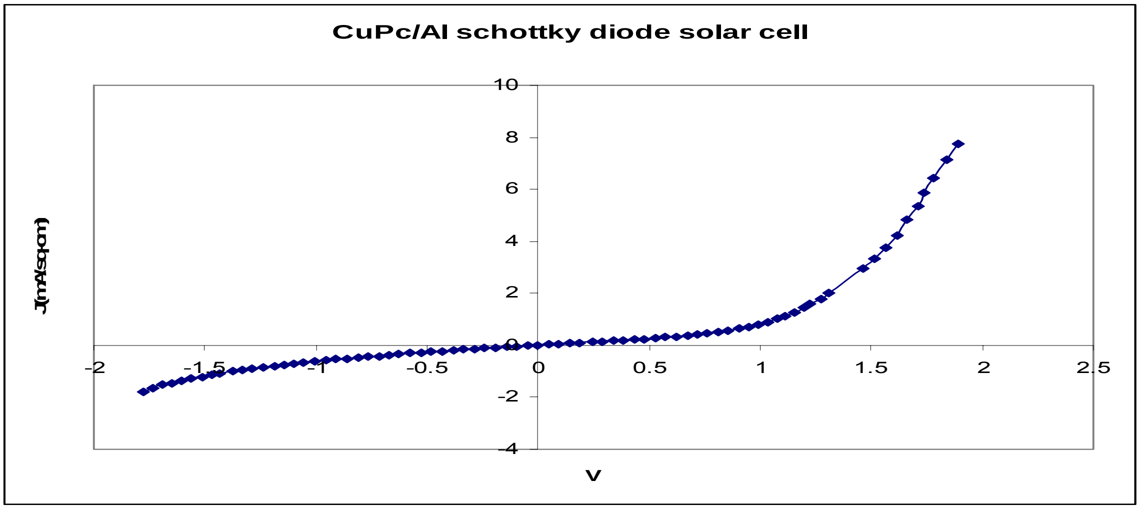

Figure 6.13 Glass/ITO/PEDOT:PPS/CuPc(15 nm)/Al Schottky diode solar cell dark curve.

The J-V characteristic was obtained by sweeping the voltage from -2 V to +2 V and measuring the resulting current. The aluminium metal contacts were 0.07 cm^2 in area. The series resistance(R_s) of the curve in Figure 6.13 was calculated to be 7.10 kΩ/cm^2. The J-V characteristic was then corrected for series resistance by subtracting JR_s from V. Figure 6.14 shows the plot of V vs. J and (V-JR_s) vs. J.

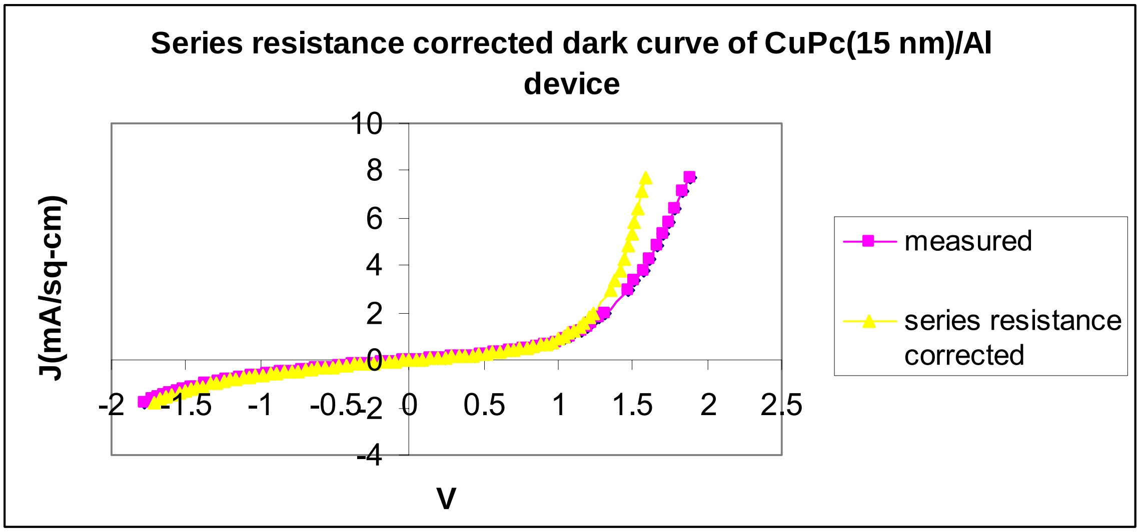

Figure 6.14 Series resistance corrected dark curve for CuPc(15 nm)/Al device.

Figure 6.15 shows the plot of ln(J) vs. V from which the value of J_o was calculated to be 0.121 mA/cm^2. The diode ideality factor n was calculated to be 7.7.

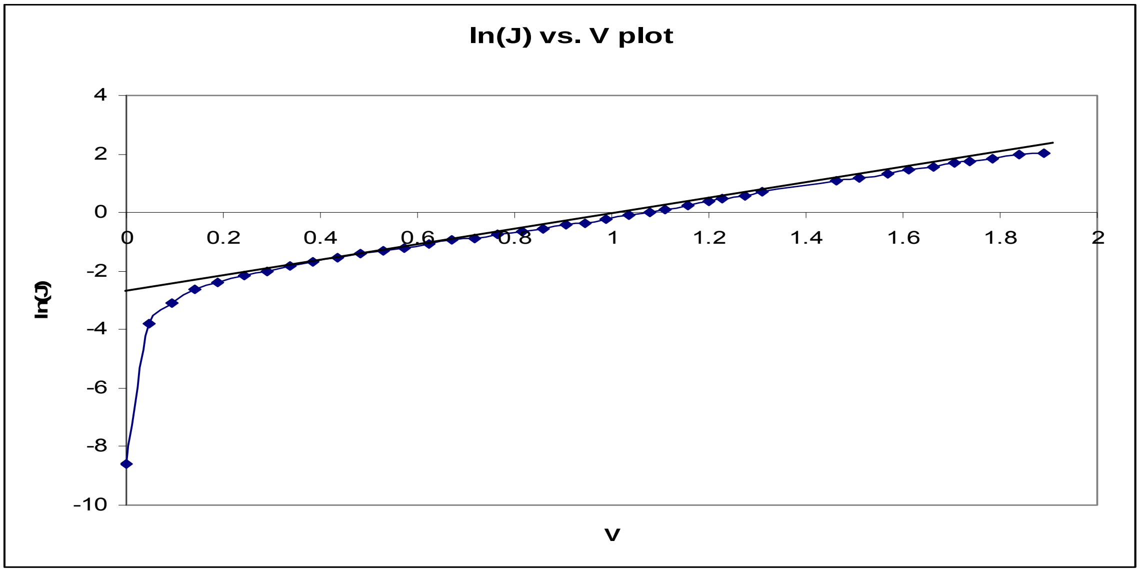

Figure 6.15 ln(J) vs. V plot for determining n and J_0 for CuPc(15 nm)/Al Schottky diode dark curve.

Figure 6.16 shows the J-V characteristics of the device Glass/ITO/PEDOT:PSS/CuPc (15 nm)/Al under illumination. The series resistance, ideality factor and reverse saturation current were computed to be 6.87 kΩ/cm^2, 7.66 and 0.147mA/cm^2 respectively. Figure 6.17 shows the series resistance corrected curve for the CuPc(15 nm)/Al light curve and Figure 6.18 shows the ln(J) vs. V plot for the CuPc(15 nm)/Al light curve.

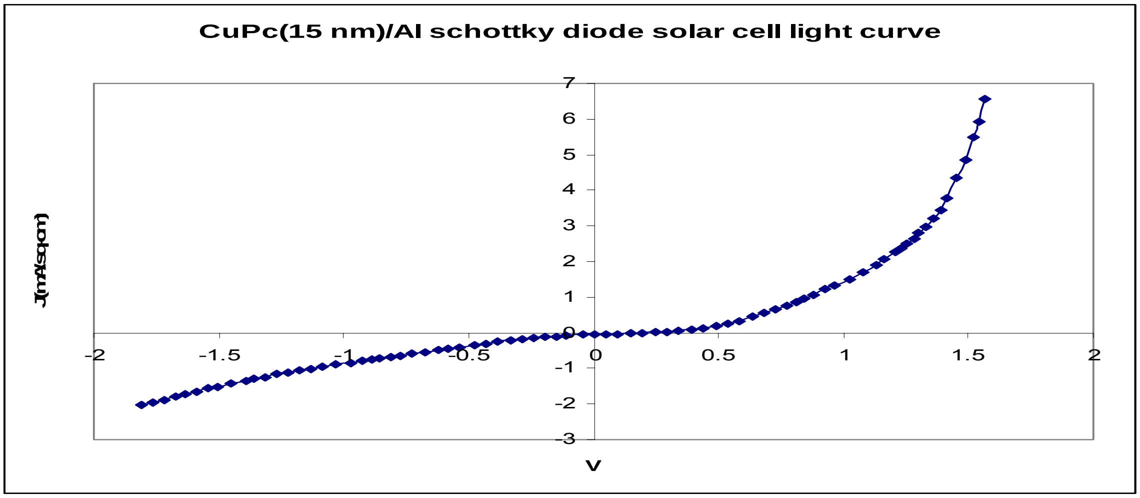

Figure 6.16 Glass/ITO/PEDOT:PPS/CuPc(15 nm)/Al Schottky diode solar cell light curve.

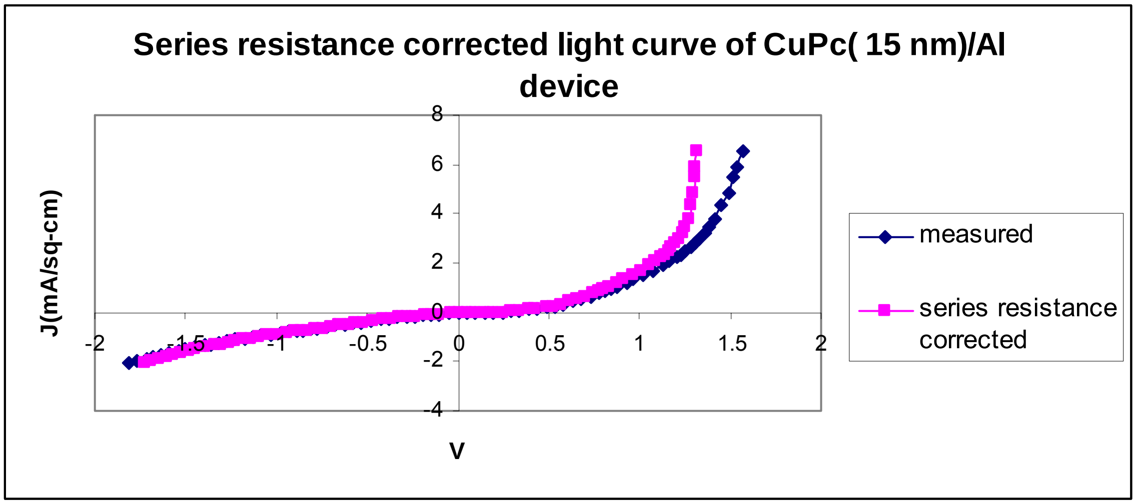

Figure 6.17 Series resistance corrected light curve for CuPc(15 nm)/Al device.

The Glass/ITO/PEDOT:PSS/CuPc(15 nm)/Al cell yielded a V_{oc} and J_{sc} of 220 mV and 0.04 mA/cm^2 respectively. The power delivered was 0.003 mW/cm^2 and the fill factor was 0.375. The cell had an efficiency of 0.003 %.

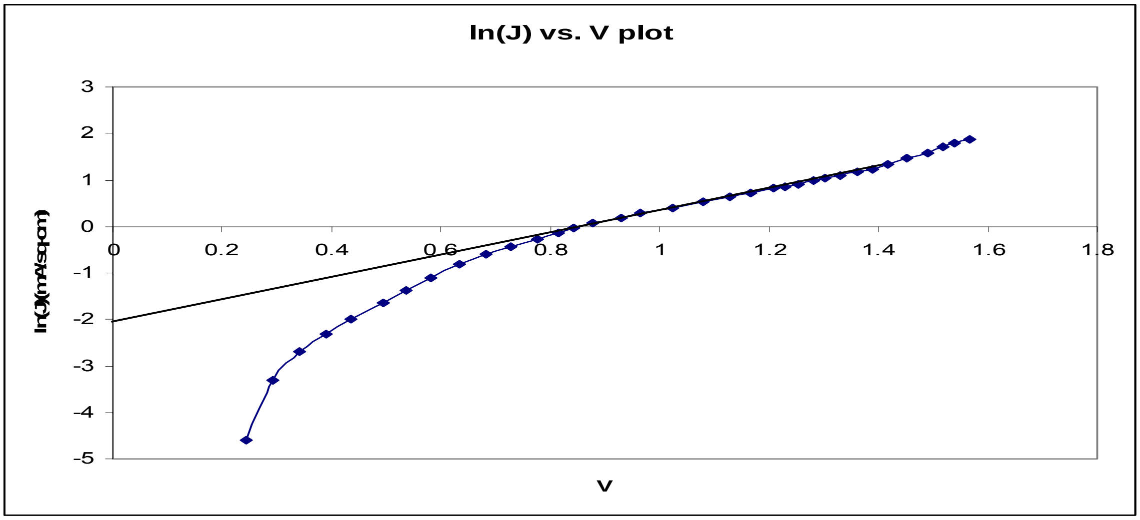

Figure 6.18 ln(J) vs. V plot for determining n and J_0 for CuPc(15 nm)/Al Schottky diode light curve.

6.6.2 J-V characteristics of CuPc(60 nm)/Al device

The series resistance(R_s) of the curve in Figure 6.19 was calculated to be 7.86 kΩ/cm^2. The J-V characteristic was then corrected for series resistance by subtracting JR_s from V. Figure 6.20 shows the plot of V vs. J and (V-JR_s) vs. J.

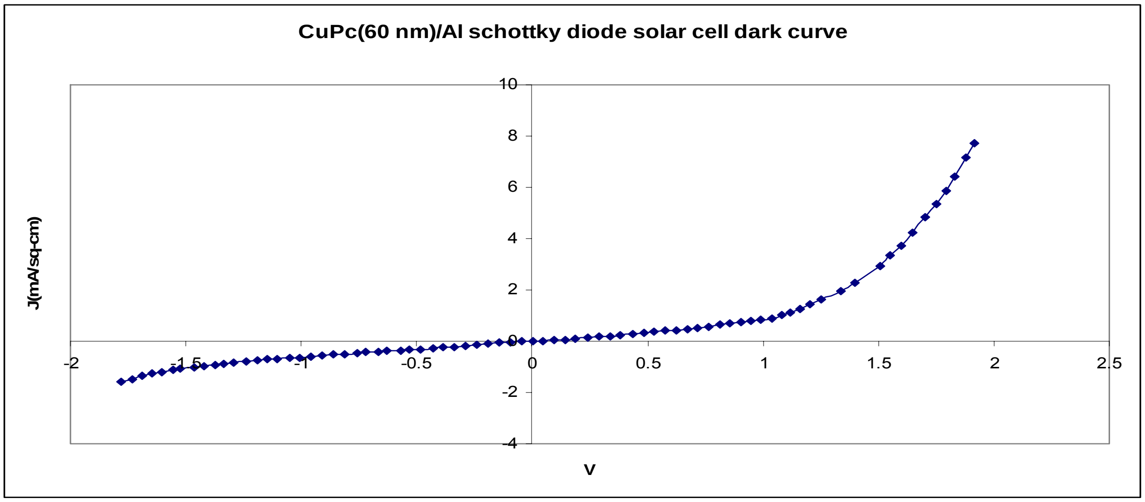

Figure 6.19 Glass/ITO/PEDOT:PPS/CuPc(60 nm)/Al Schottky diode solar cell dark curve.

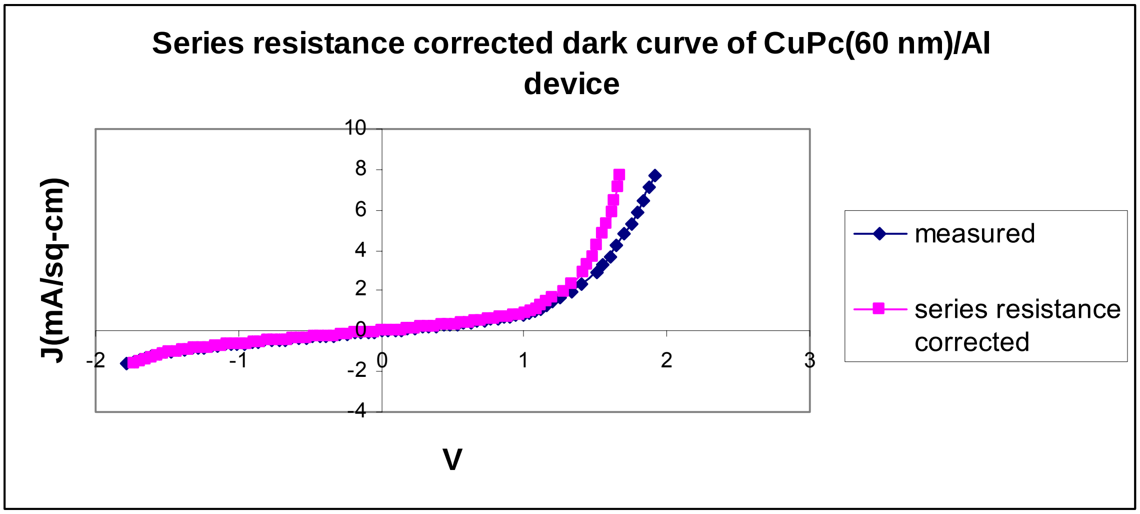

Figure 6.20 Series resistance corrected dark curve for CuPc(60 nm)/Al device.

Figure 6.21 shows the plot of ln(J) vs. V from which the value of J_o was calculated to be 0.127 mA/cm^2. The diode ideality factor n was calculated to be 18.03.

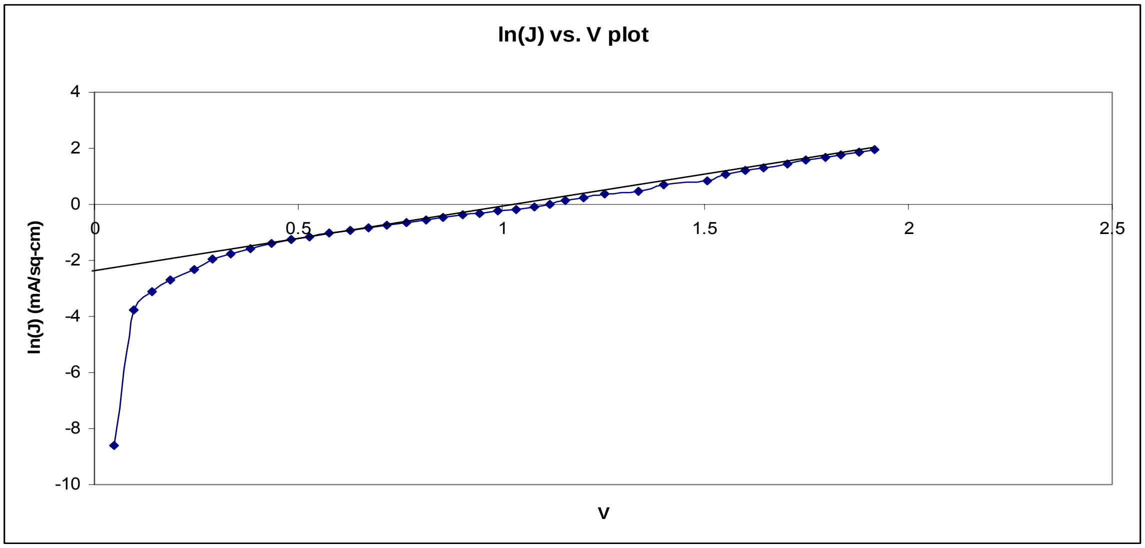

Figure 6.21 ln(J) vs. V plot for determining n and J_0 for CuPc(60nm)/Al Schottky diode dark curve.

Figure 6.22 shows the J-V characteristics of the device Glass/ITO/PEDOT:PSS/CuPc(60 nm)/Al under illumination. The series resistance(R_s), ideality factor and reverse saturation current were calculated to be 7.12 kΩ/cm^2, 19.3 and .110 mA/cm^2 respectively. The J-V characteristic was then corrected for series resistance by subtracting JR_s from V. Figure 6.23 shows the plot of V vs. J and (V-JR_s) vs. J.

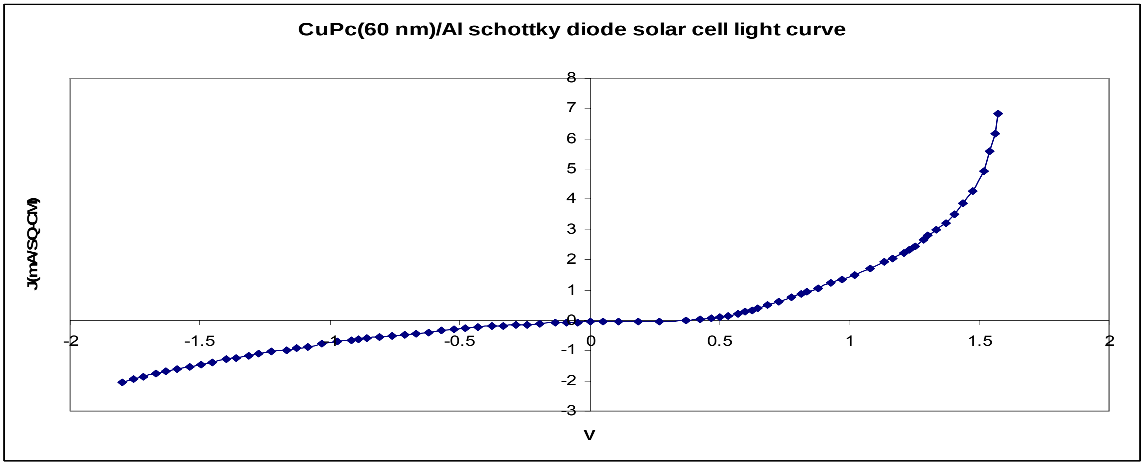

Figure 6.22 Glass/ITO/PEDOT:PPS/CuPc(60 nm)/Al Schottky diode solar cell light curve.

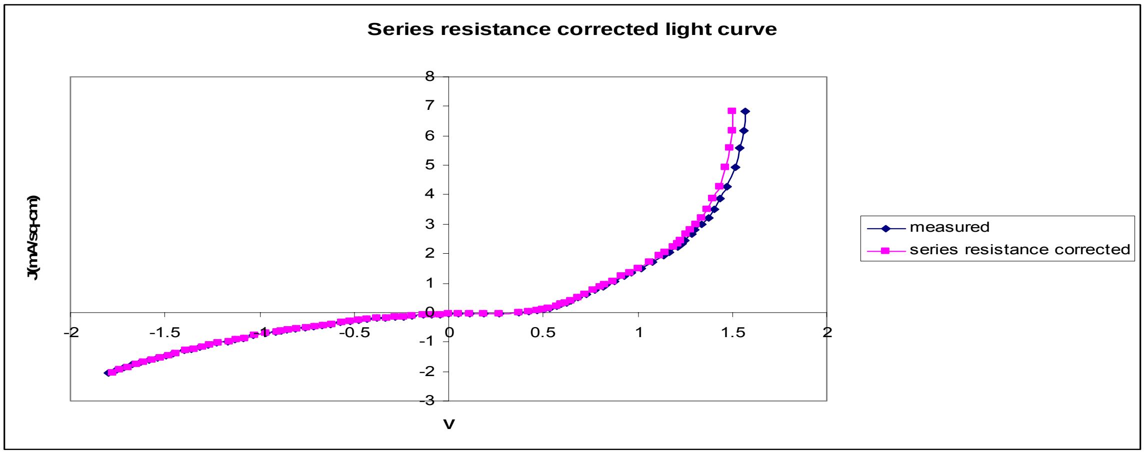

Figure 6.23 Series resistance corrected light curve for CuPc(60 nm)/Al device.

The Glass/ITO/PEDOT:PSS/CuPc(60 nm)/Al cell yielded a V_{oc} and J_{sc} of 360 mV and 0.054 mA/cm^2 respectively. The power delivered was 0.006 mW/cm^2 and the fill factor was 0.315. The cell had an efficiency of 0.006 %. Figure 6.24 shows the ln(J) vs. V plot of the device under illumination.

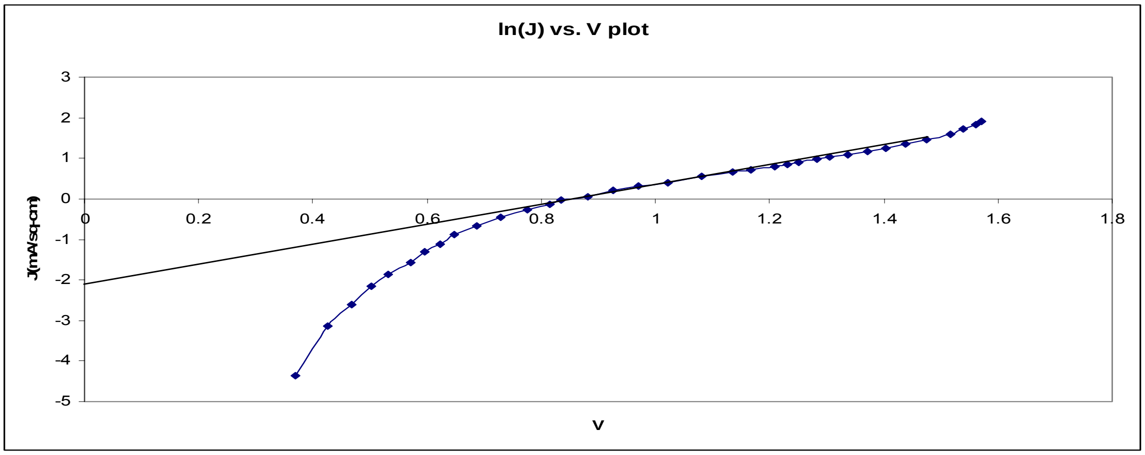

Figure 6.24 ln(J) vs. V plot for determining n and J_0 for CuPc(60 nm)/Al Schottky diode light curve.

6.6.3 J-V characteristics of CuPc(80 nm)/Al device

Figure 6.25 shows the J-V characteristics of the device Glass/ITO/PEDOT:PSS/CuPc (80 nm)/Al under dark conditions. The series resistance

(R_s) of the curve in Figure 6.25 was calculated to be 8.45 kΩ/cm^2. The J-V characteristic was then corrected for series resistance by subtracting JR_s from V. Figure 6.26 shows the plot of V vs. J and ($V-JR_s$) vs. J.

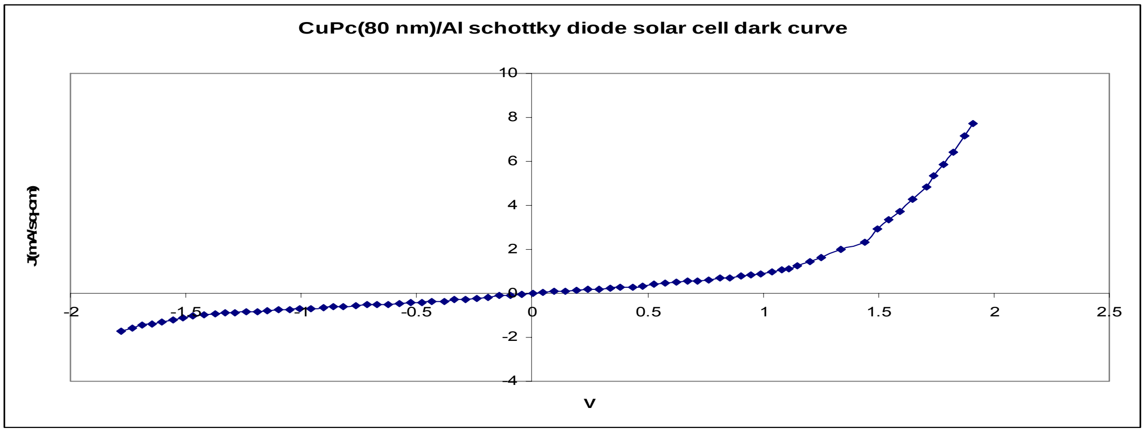

Figure 6.25 Glass/ITO/PEDOT:PPS/CuPc(80 nm)/Al Schottky diode solar cell dark curve.

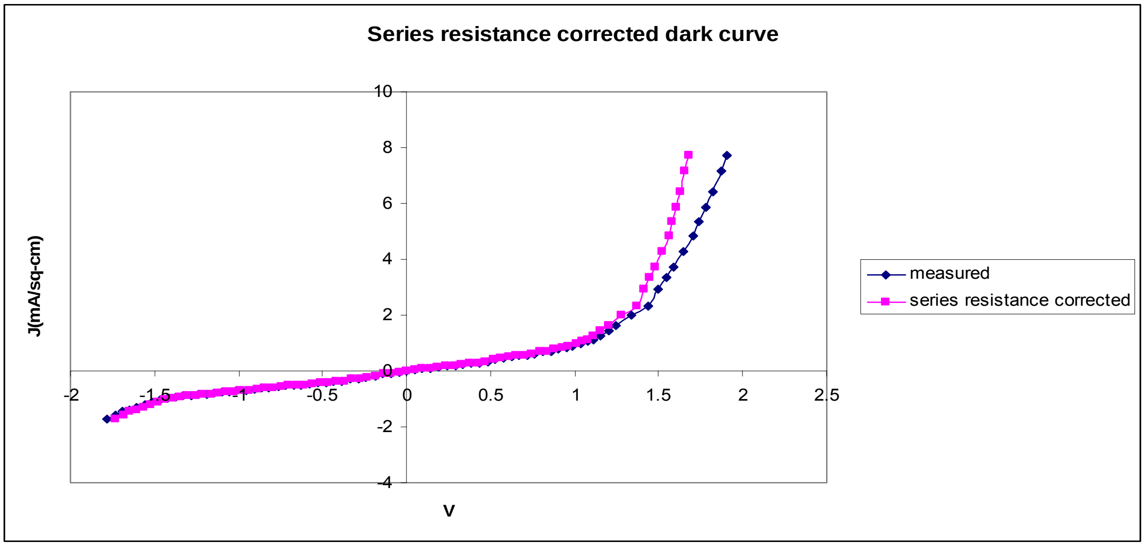

Figure 6.26 Series resistance corrected dark curve for CuPc(80 nm)/Al device.

Figure 6.27 shows the plot of ln(J) vs. V from which the value of J_o was calculated to be 0.135 mA/cm^2. The diode ideality factor n was calculated to be 17.5.

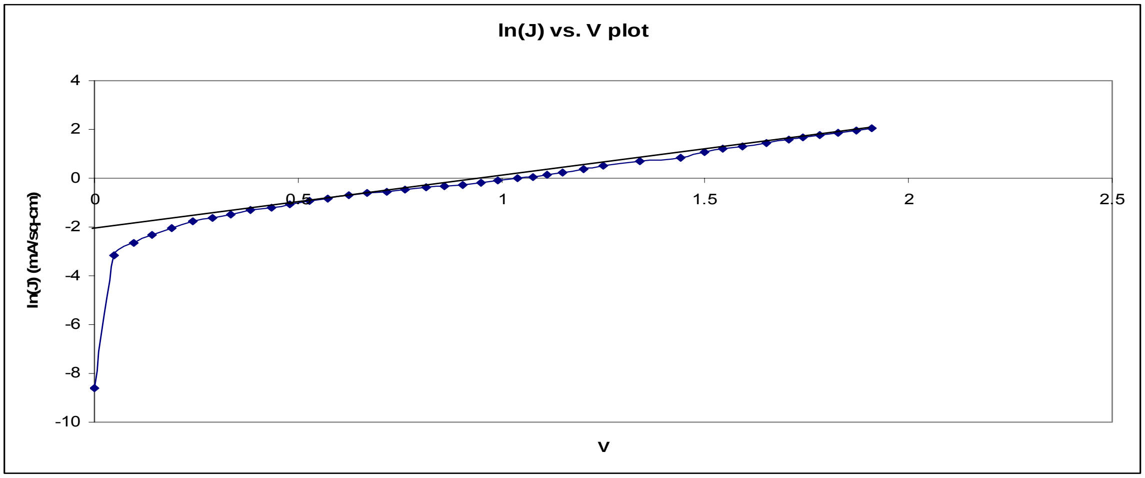

Figure 6.27 ln(J) vs. V plot for determining n and J_0 for CuPc(80 nm)/Al Schottky diode dark curve.

Figure 6.28 shows the J-V characteristics of the device Glass/ITO/PEDOT:PSS/CuPc(80 nm)/Al under illumination. The series resistance (R_s), ideality factor and reverse saturation current were calculated to be 8.24 kΩ/cm^2, 16.08 and .03 mA/cm^2. The J-V characteristic was then corrected for series resistance by subtracting JR_s from V. Figure 6.29 shows the plot of V vs. J and ($V-JR_s$) vs. J.

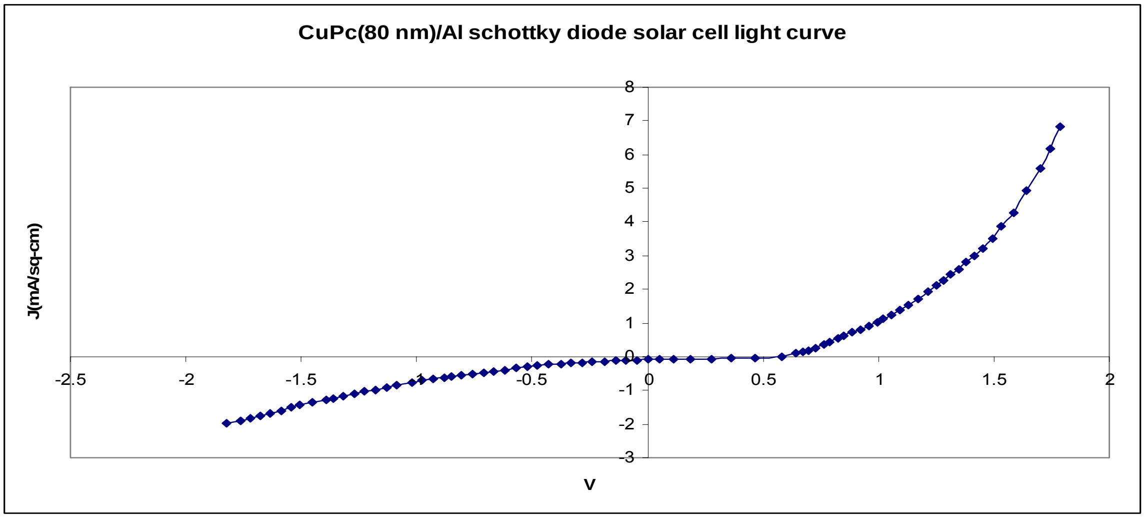

Figure 6.28 Glass/ITO/PEDOT:PPS/CuPc(80 nm)/Al Schottky diode solar cell light curve.

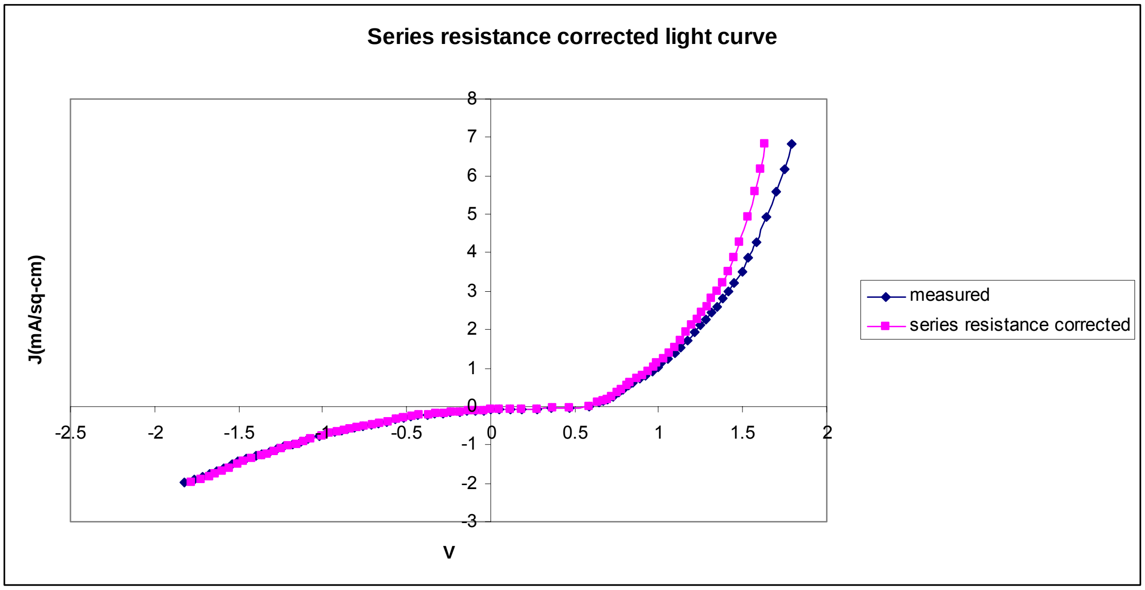

Figure 6.29 Series resistance corrected light curve for CuPc(80 nm)/Al device.

The Glass/ITO/PEDOT:PSS/CuPc(80 nm)/Al cell yielded a V_{oc} and J_{sc} of 584 mV and 0.094 mA/cm^2 respectively. The power delivered was 0.016 mW/cm^2 and the fill factor was 0.29. The cell had an efficiency of 0.016 %.

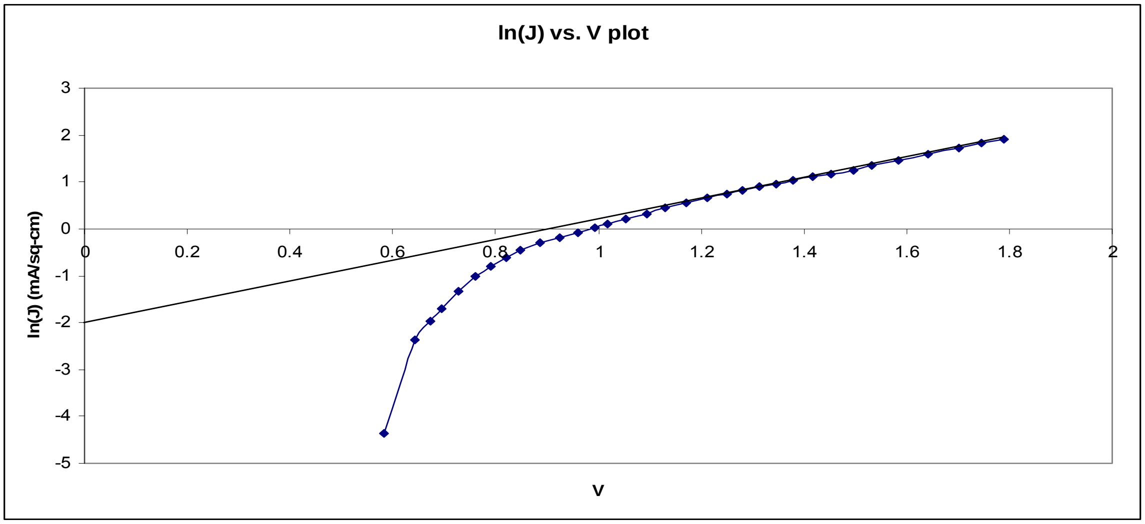

Figure 6.30 ln(J) vs. V plot for determining n and J_0 for CuPc(80 nm)/Al Schottky diode light curve.

6.6.4 J-V characteristics of CuPc(100 nm)/Al device

Figure 6.31 shows the J-V characteristics of the device Glass/ITO/PEDOT:PSS/CuPc (100 nm)/Al under dark conditions. The series resistance (R_s) of the curve in Figure 6.31 was calculated to be 8.31 kΩ/cm^2. The J-V characteristic was then corrected for series resistance by subtracting JR_s from V. Figure 6.32 shows the plot of V vs. J and ($V-JR_s$) vs. J.

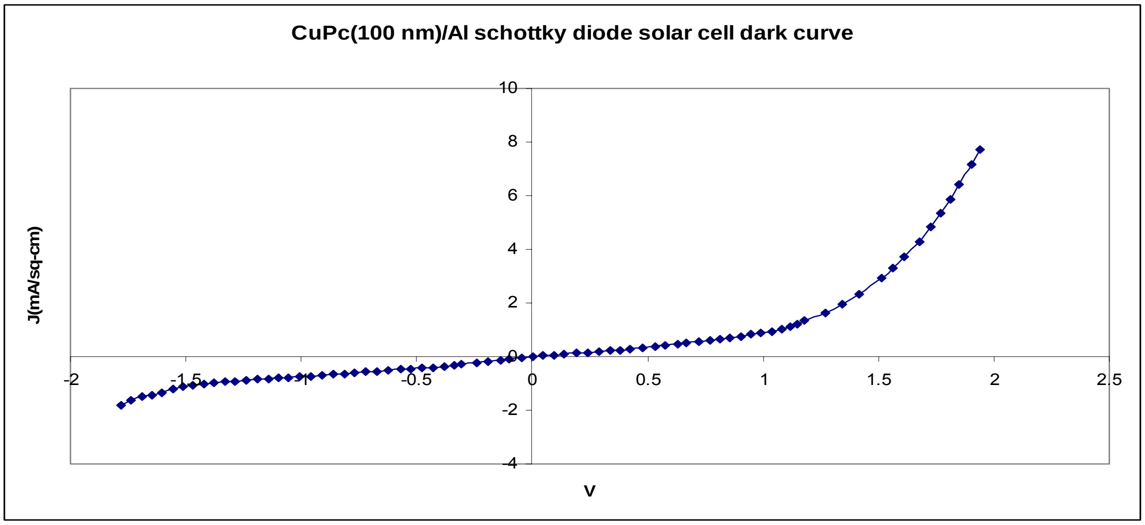

Figure 6.31 Glass/ITO/PEDOT:PPS/CuPc(100 nm)/Al Schottky diode solar cell dark curve.

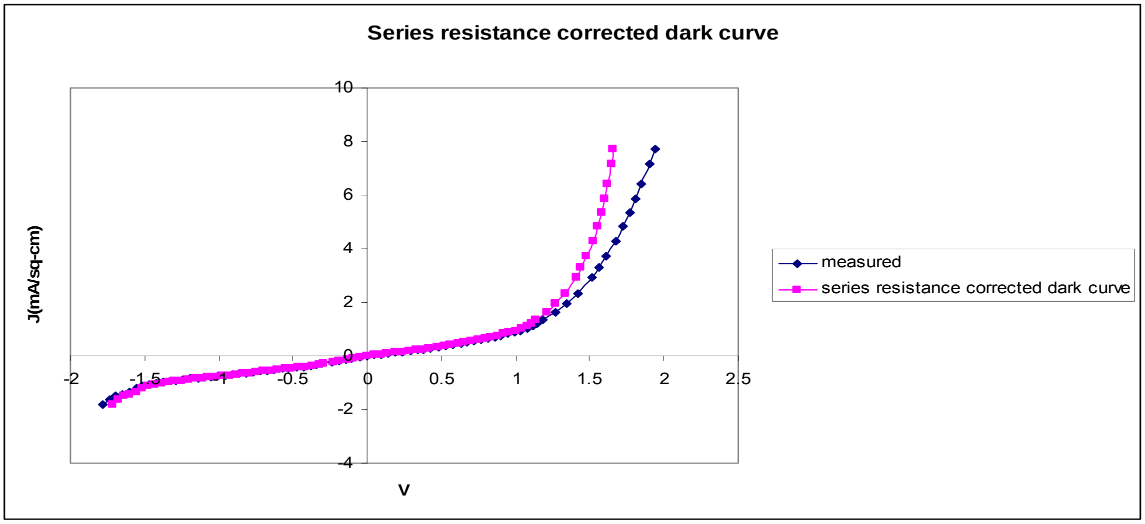

Figure 6.32 Series resistance corrected dark curve for CuPc(100 nm)/Al device.

Figure 6.33 shows the plot of ln(J) vs. V from which the value of J_o was calculated to be 0.149 mA/cm^2. The diode ideality factor n was calculated to be 17.78.

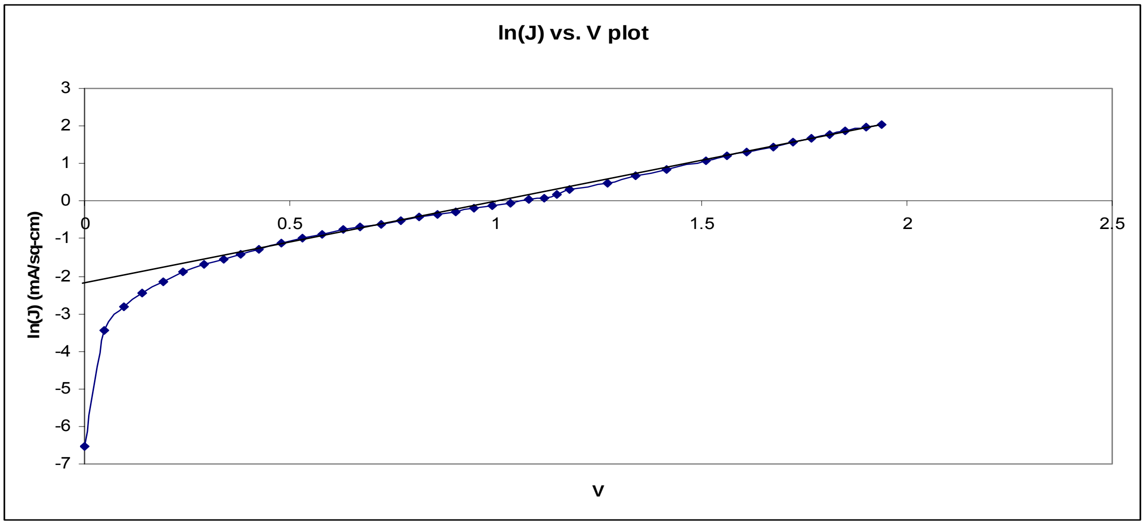

Figure 6.33 ln(J) vs. V plot for determining n and J_0 for CuPc(100 nm)/Al Schottky diode dark curve.

Figure 6.34 shows the J-V characteristics of the device Glass/ITO/PEDOT:PSS/CuPc (100 nm)/Al under illumination. The series resistance (R_s), ideality factor and reverse saturation current were calculated to be 8.57 kΩ/cm^2, 17.62 and .139 mA/cm^2 respectively. The J-V characteristic was then corrected for series resistance by subtracting JR_s from V. Figure 6.35 shows the plot of V vs. J and ($V-JR_s$) vs. J.

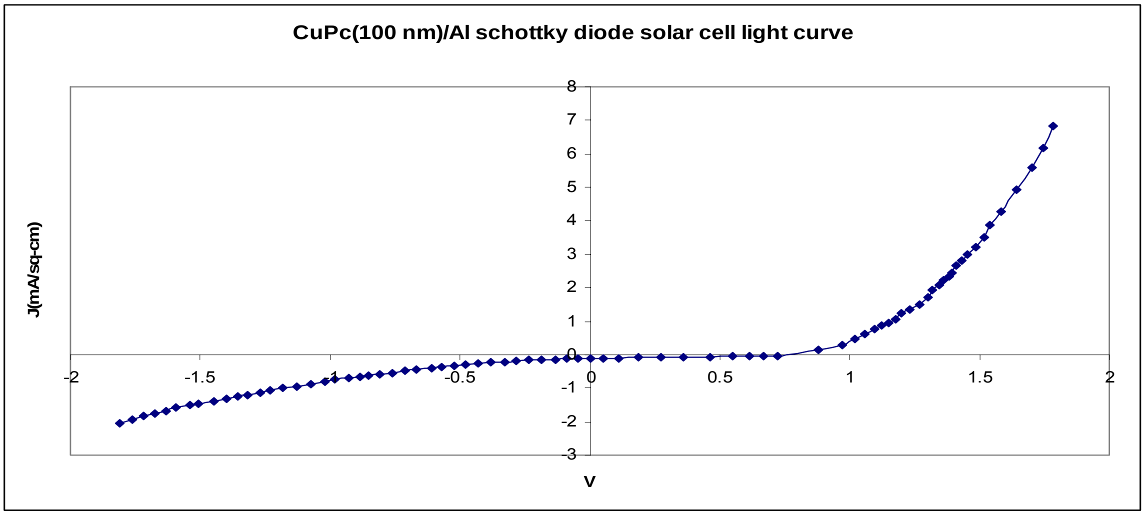

Figure 6.34 Glass/ITO/PEDOT:PPS/CuPc(100 nm)/Al Schottky diode solar cell light curve.

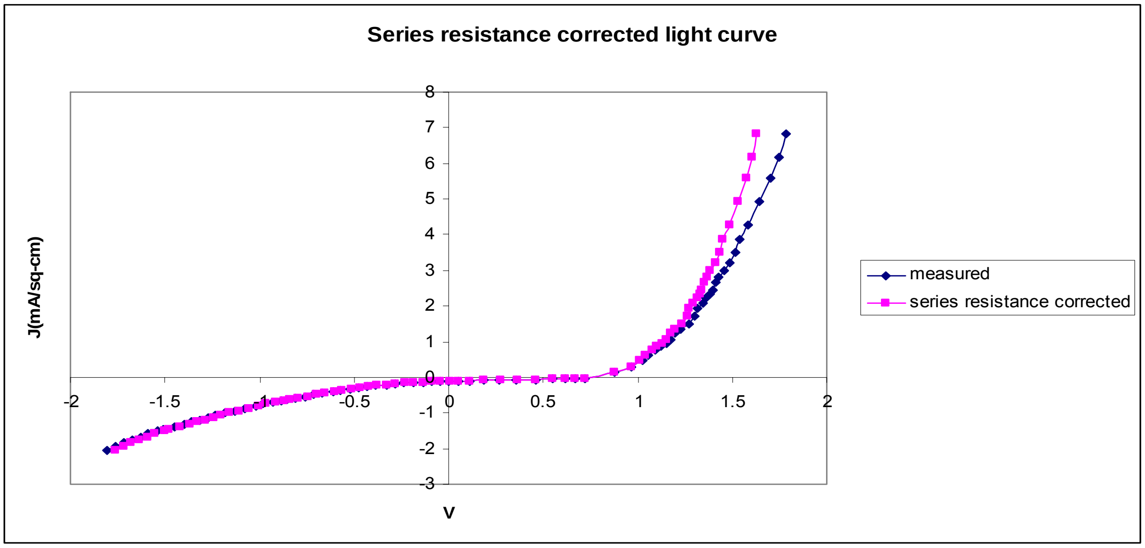

Figure 6.35 Series resistance corrected light curve for CuPc(100 nm)/Al device.

The Glass/ITO/PEDOT:PSS/CuPc(100 nm)/Al cell yielded a V_{oc} and J_{sc} of 770 mV and 0.114 mA/cm^2. The power delivered was 0.027 mW/cm^2 and the fill factor was 0.31. The cell had an efficiency of 0.027 %.

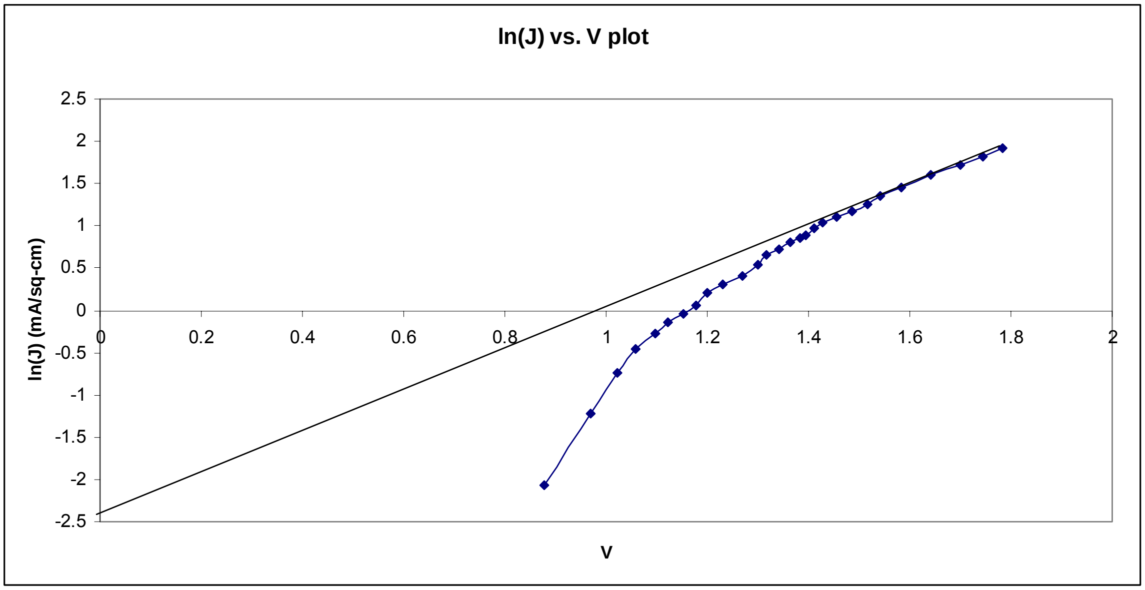

Figure 6.36 ln(J) vs. V plot for determining n and J_0 for CuPc(100 nm)/Al Schottky diode light curve.

6.6.5 J-V characteristics of the CuPc (120 nm)/Al device

Figure 6.37 shows the J-V characteristics of the device Glass/ITO/PEDOT:PSS/CuPc (120 nm)/Al under dark conditions. The series resistance (R_s) of the curve in Figure 6.37 was calculated to be 9.32 kΩ/cm^2. The J-V characteristic was then corrected for series resistance by subtracting JR_s from V. Figure 6.38 shows the plot of V vs. J and (V-JR_s) vs. J.

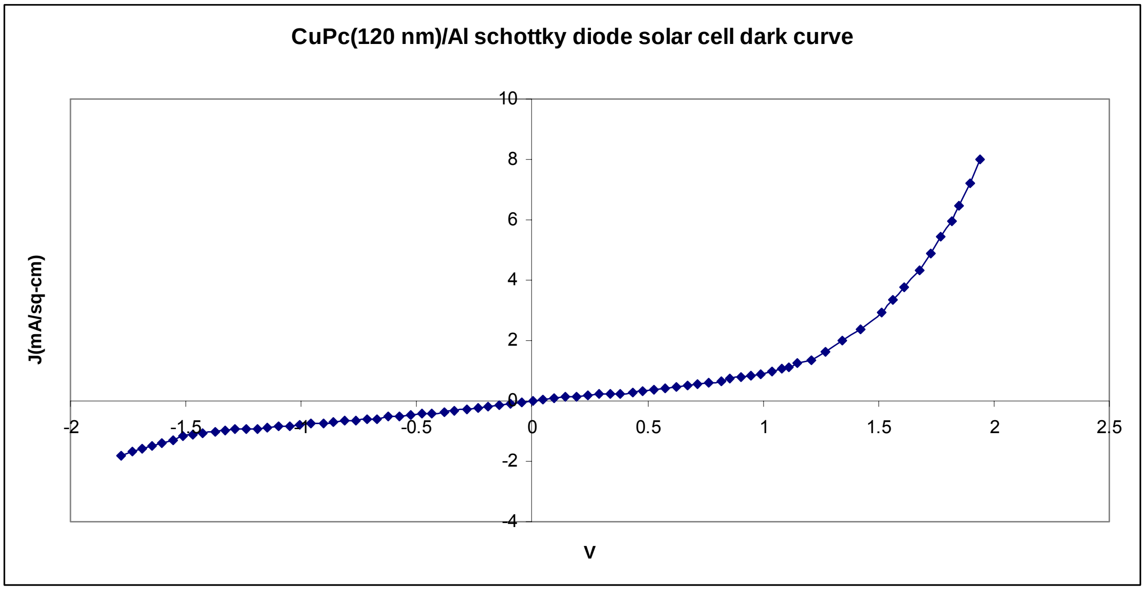

Figure 6.37 Glass/ITO/PEDOT:PPS/CuPc(120 nm)/Al Schottky diode solar cell dark curve.

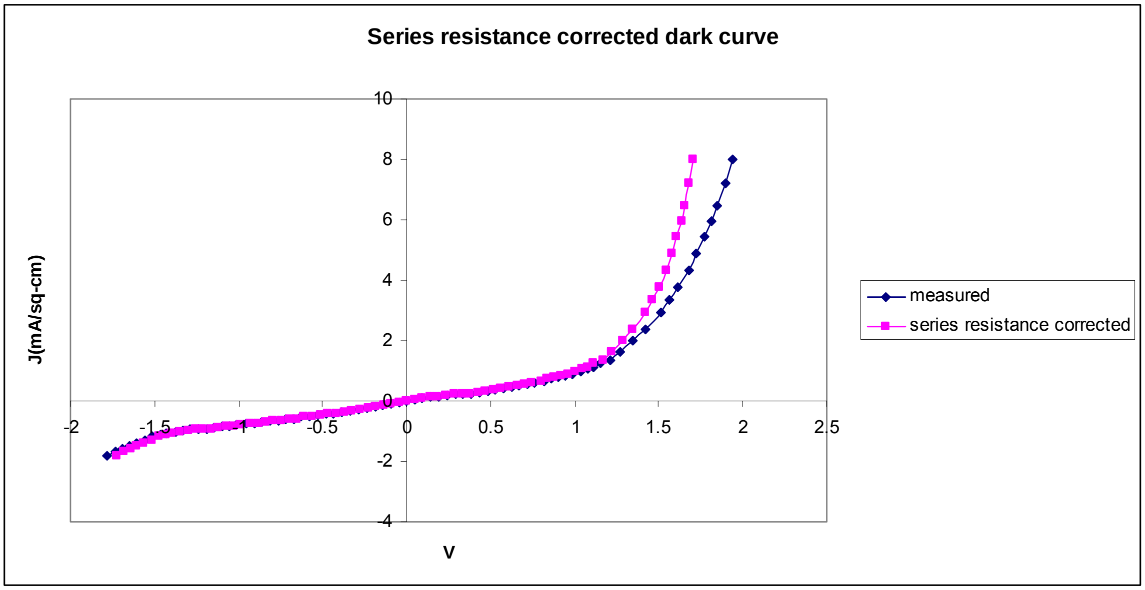

Figure 6.38 Series resistance corrected dark curve for CuPc (120 nm)/Al device.

Figure 6.39 shows the plot of ln(J) vs. V from which the value of J_o was calculated to be 0.142 mA/cm^2. The diode ideality factor n was calculated to be 15.95.

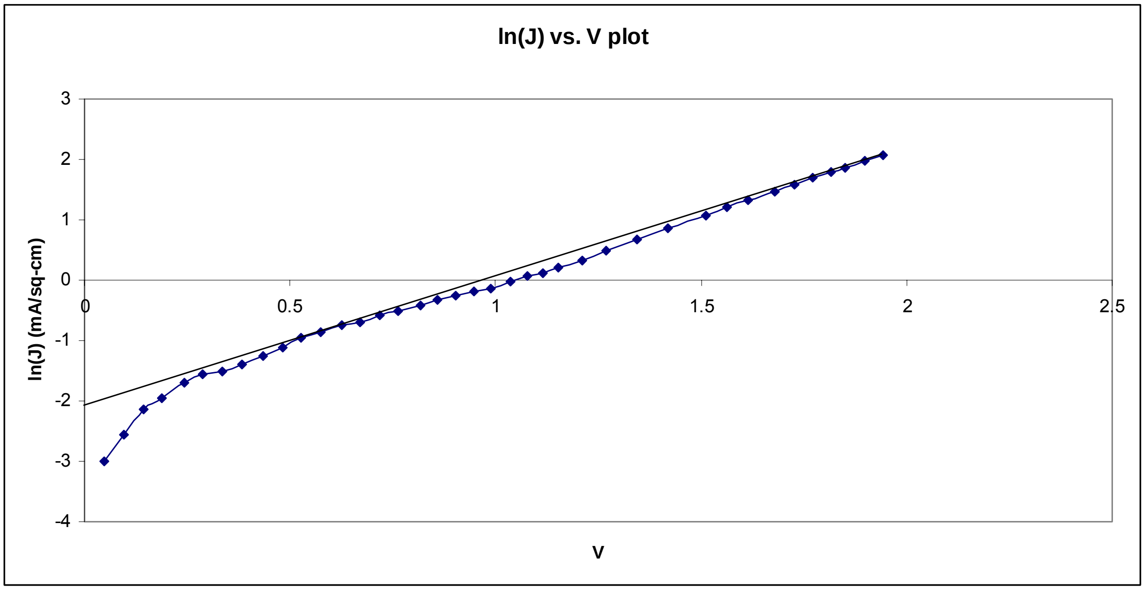

Figure 6.39 ln(J) vs. V plot for determining n and J_0 for CuPc(120 nm)/Al Schottky diode dark curve.

Figure 6.40 shows the J-V characteristics of the device Glass/ITO/PEDOT:PSS/CuPc (120 nm)/Al under illumination. The series resistance (R_s), ideality factor and reverse saturation current were calculated to be 9.11 kΩ/cm^2, 16.5 and 0.118mA/cm^2 respectively. The J-V characteristic was then corrected for series resistance by subtracting JR_s from V. Figure 6.41 shows the plot of V vs. J and (V-JR_s) vs. J.

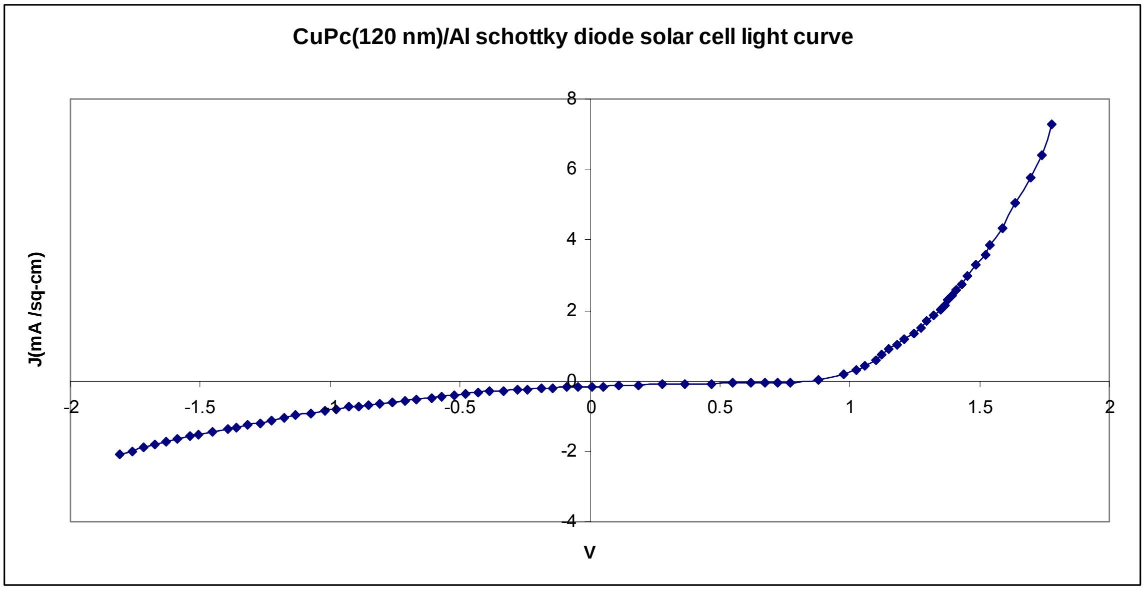

Figure 6.40 Glass/ITO/PEDOT:PPS/CuPc(120 nm)/Al Schottky diode solar cell light curve.

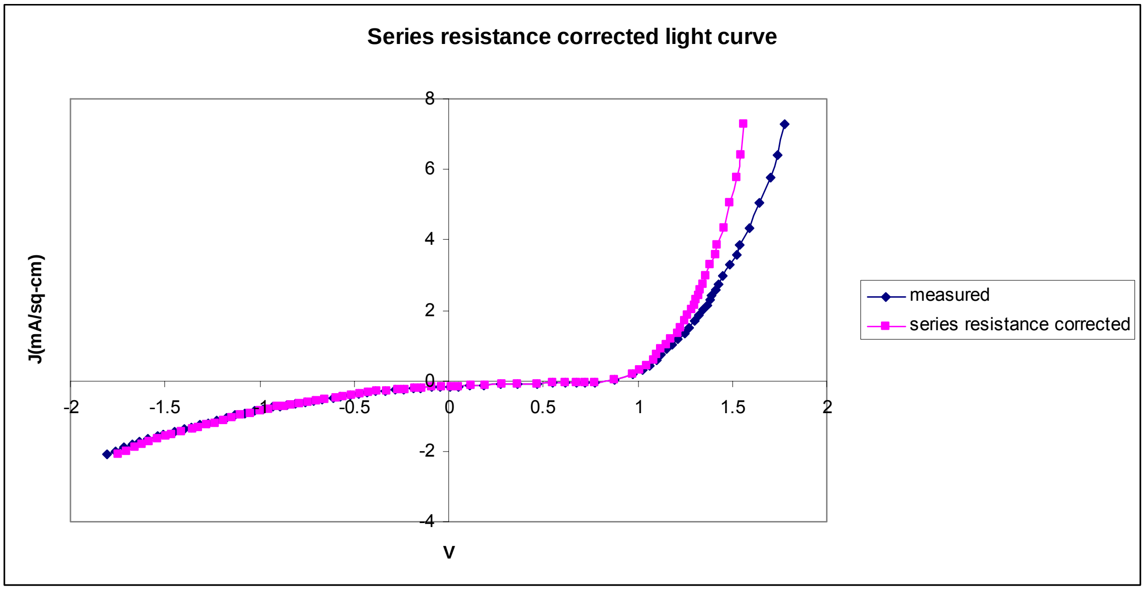

Figure 6.41 Series resistance corrected light curve for CuPc (120 nm)/Al device.

The Glass/ITO/PEDOT:PSS/CuPc (120 nm)/Al cell yielded a V_{oc} and J_{sc} of 879 mV and 0.124 mA/cm^2 respectively. The power delivered was 0.036 mW/cm^2 and the fill factor was 0.33. The cell had an efficiency of 0.036 %.

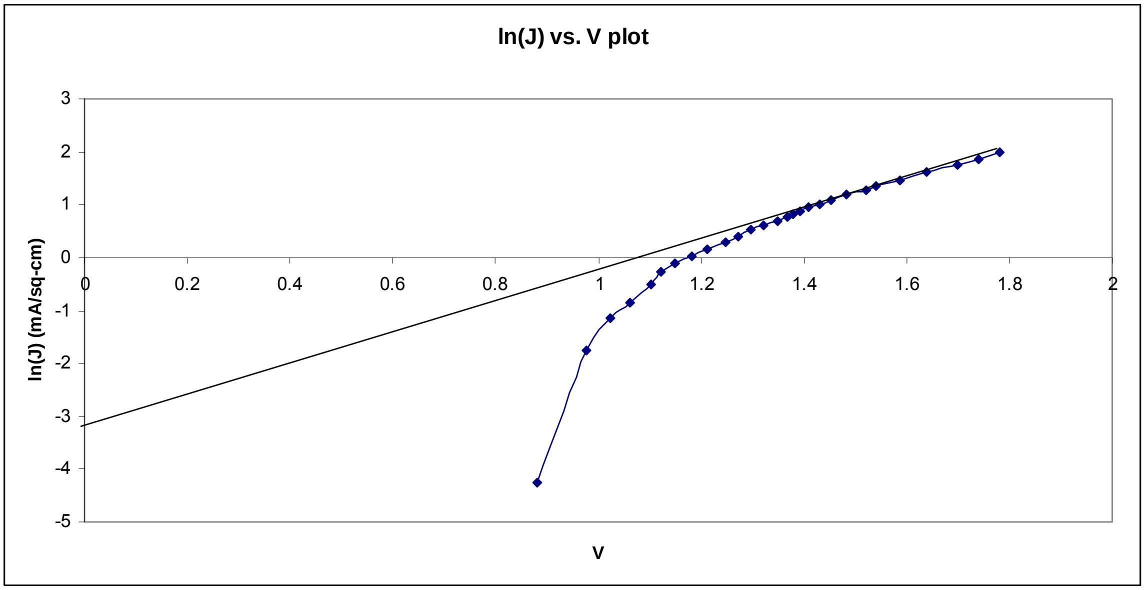

Figure 6.42 ln(J) vs. V plot for determining n and J_0 for CuPc(120 nm)/Al Schottky diode light curve.

6.6.6 J-V characteristics of the CuPc(140 nm)/Al device

Figure 6.43 shows the J-V characteristics of the device Glass/ITO/PEDOT:PSS/CuPc (140 nm)/Al under dark conditions. The series resistance (R_s) of the curve in Figure 6.38 was calculated to be 9.41 kΩ/cm^2. The J-V characteristic was then corrected for series resistance by subtracting JR_s from V. Figure 6.44 shows the plot of V vs. J and (V-JR_s) vs. J.

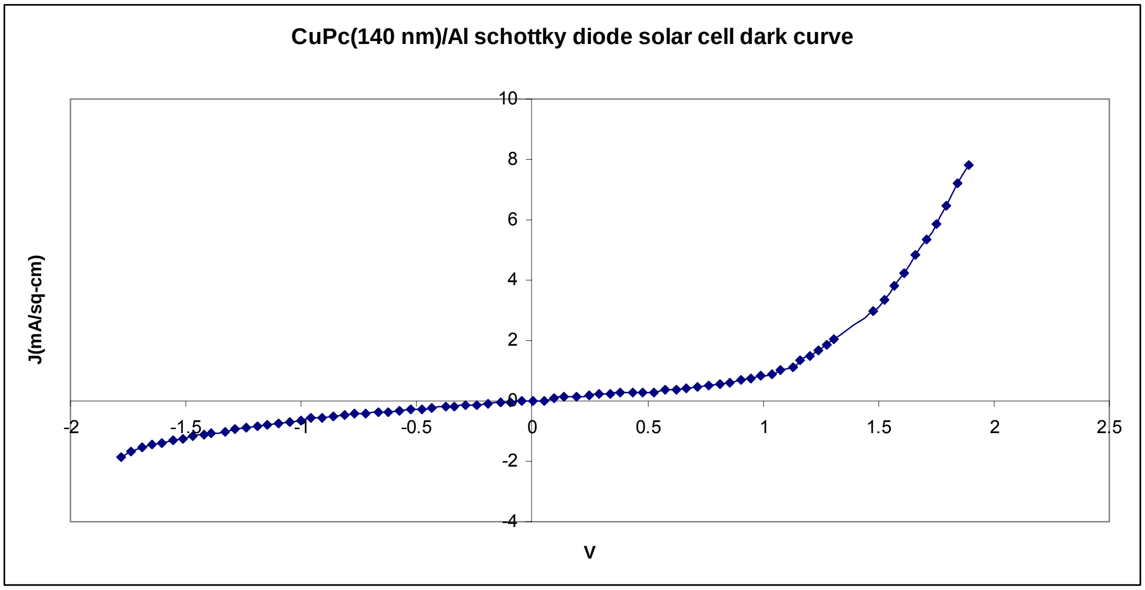

Figure 6.43 Glass/ITO/PEDOT:PPS/CuPc(140 nm)/Al Schottky diode solar cell dark curve.

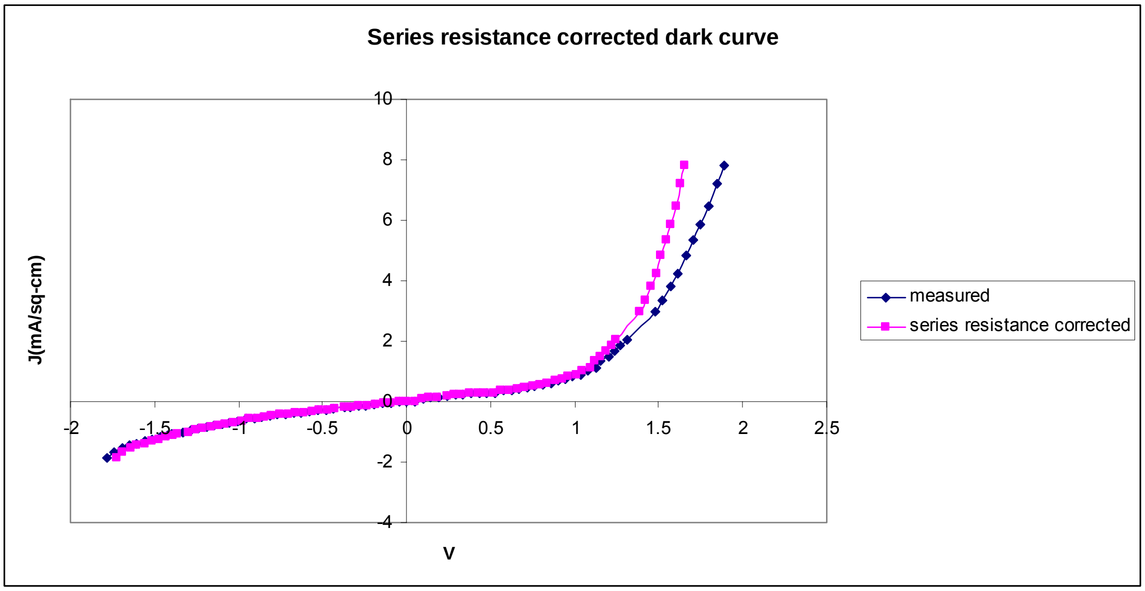

Figure 6.44 Series resistance corrected dark curve for CuPc (140 nm)/Al device.

Figure 6.45 shows the plot of ln(J) vs. V from which the value of J_o was calculated to be 0.126 mA/cm^2. The diode ideality factor n was calculated to be 18.29.

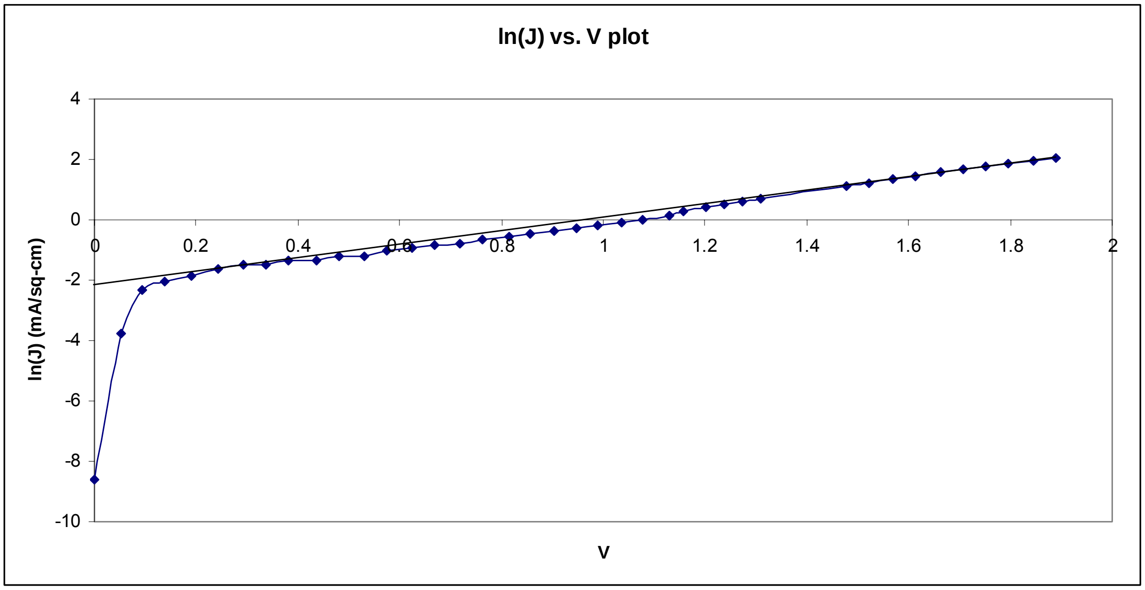

Figure 6.45 ln(J) vs. V plot for determining n and J_0 for CuPc(140 nm)/Al Schottky diode dark curve.

Figure 6.46 shows the J-V characteristics of the device Glass/ITO/PEDOT:PSS/CuPc (140 nm)/Al under illumination. The series resistance (R_S), ideality factor and reverse saturation current were calculated to be 8.97 kΩ/cm^2, 16.08 and .109 mA/cm^2 respectively. The J-V characteristic was then corrected for series resistance by subtracting JR_s from V. Figure 6.47 shows the plot of V vs. J and (V-JR_s) vs. J.

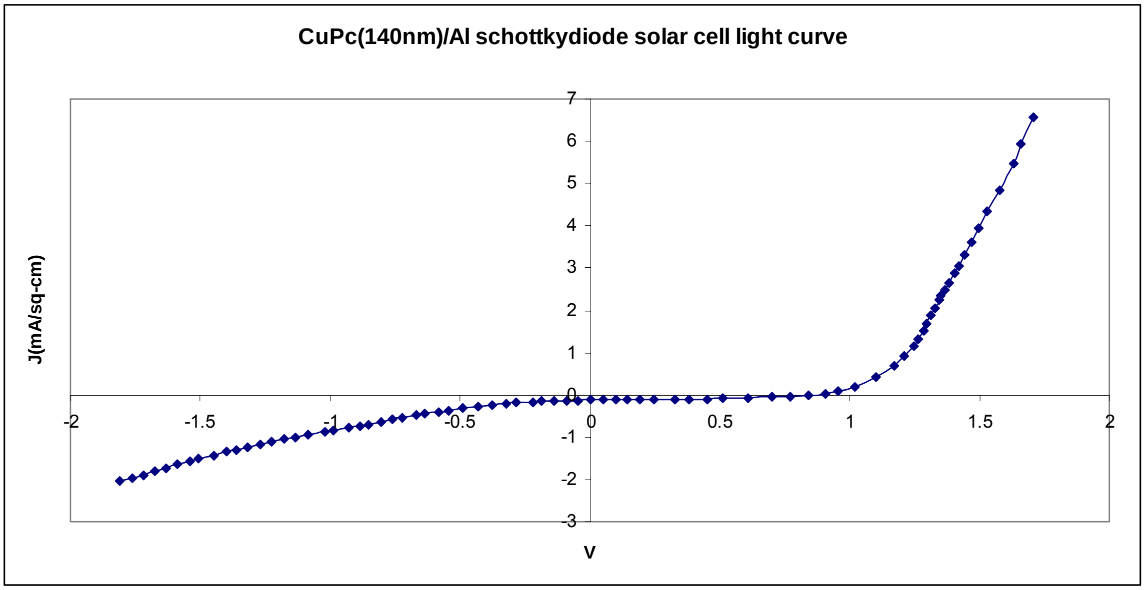

Figure 6.46 Glass/ITO/PEDOT:PPS/CuPc(140 nm)/Al Schottky diode solar cell light curve.

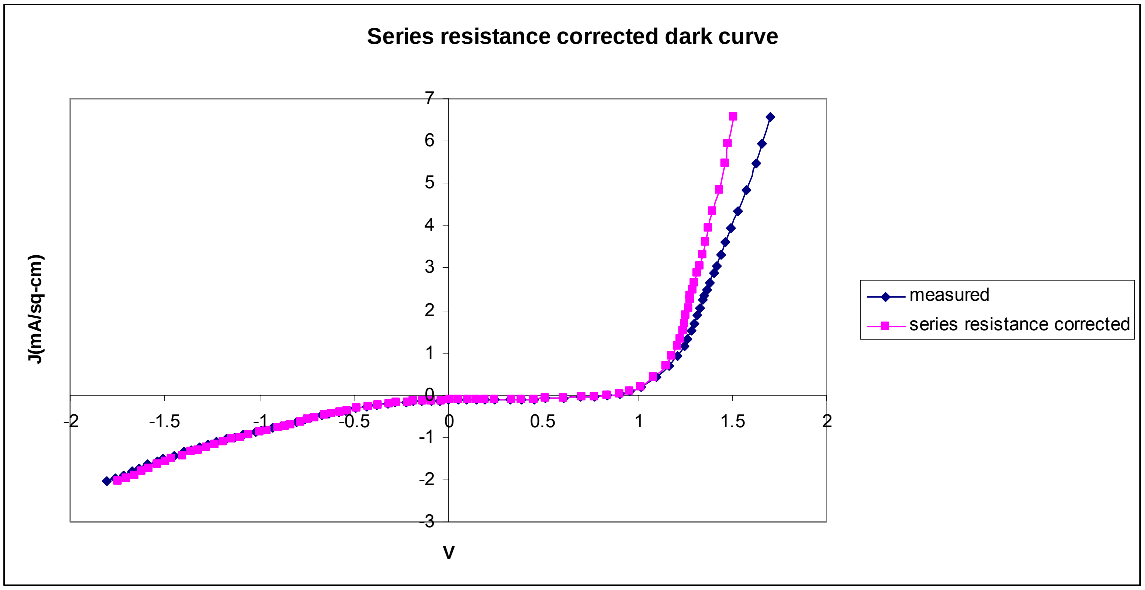

Figure 6.47 Series resistance corrected light curve for CuPc (140 nm)/Al device.

The Glass/ITO/PEDOT:PSS/CuPc (140 nm)/Al cell yielded a V_{oc} and J_{sc} of 907 mV and 0.125 mA/cm^2 respectively. The power delivered was 0.046 mW/cm^2 and the fill factor was 0.407. The cell had an efficiency of 0.046 %.

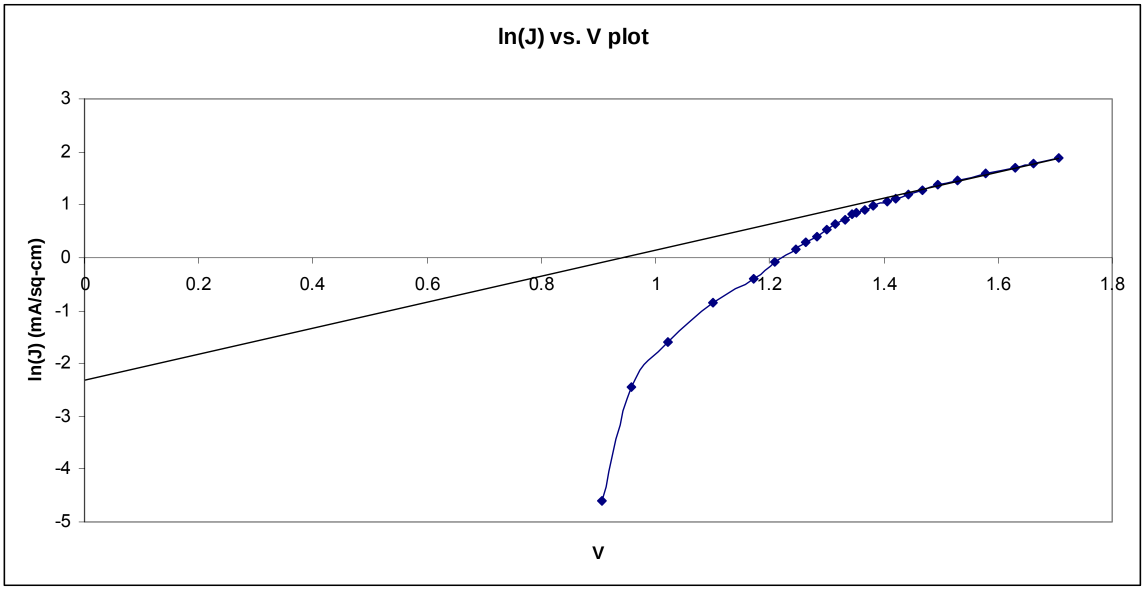

Figure 6.48 ln(J) vs. V plot for determining n and J_0 for CuPc(140 nm)/Al Schottky diode light curve.

Thickness	Series Resistance (R_s)	Ideality Factor (n)	J_o (mA/cm^2)
15 nm	7.10 kΩ/cm^2	7.7	0.121
60 nm	7.86 kΩ/cm^2	18.03	0.127
80 nm	8.45 kΩ/cm^2	17.5	0.135
100 nm	8.31 kΩ/cm^2	17.78	0.149
120 nm	9.32 kΩ/cm^2	15.95	0.142
140 nm	9.41 kΩ/cm^2	18.29	0.126

Table 6.3 Results of different thickness of CuPc Schottky diode solar cell dark curves.

From Table 6.3 it can be observed that the series resistance of the devices increases with the thickness of the CuPc film. Also the high series resistance of the devices can be attributed to the low electrical conductivity of the CuPc film and the PEDOT:PSS layer. From the J-V characteristics of the dark curves of the devices it can be observed that the curves show a slope in the reverse bias which can be attributed to the shunting paths available between the metal contact and the PEDOT:PSS layer. Also the high reverse saturation currents indicate some physical shunting paths.

Thickness	**R_s**	**n**	**J_o**	**V_{oc}**	**J_{sc}**	**F. F.**	**P. D.**	**η**
15 nm	6.87 kΩ/cm^2	7.66	0.147 mA/cm^2	220 mV	0.042 mA/cm^2	0.37	0.003	0.003 %
60 nm	7.12 kΩ/cm^2	19.30	0.110 mA/cm^2	360 mV	0.054 mA/cm^2	0.31	0.006	0.006%
80 nm	8.24 kΩ/cm^2	16.08	0.127 mA/cm^2	584 mV	0.094 mA/cm^2	0.29	0.016	0.016%
100 nm	8.57 kΩ/cm^2	17.62	0.139 mA/cm^2	770 mV	0.114 mA/cm^2	0.31	0.027	0.027%
120 nm	9.11 kΩ/cm^2	16.50	0.118 mA/cm^2	879 mV	0.124 mA/cm^2	0.33	0.036	0.036%
140 nm	8.97 kΩ/cm^2	16.08	0.109 mA/cm^2	907 mV	0.125 mA/cm^2	0.40	0.046	0.046%

Table 6.4 Results of different thickness of CuPc Schottky diode solar cell light curves.

Table 6.4 indicates the variation of series resistance (R_s), ideality factor (n), reverse saturation current density (J_o), open circuit voltage (V_{oc}), short circuit current (J_{sc}), fill factor, power delivered by the cell and the efficiency of the cell. As in the case of the dark curves, the series resistance of the cells under illumination also increases with the thickness of the CuPc films due to the high resistance offered by the increased thickness and the PEDOT:PSS layer. The high reverse saturation currents indicate the presence of some physical shunting paths. The values quoted in the Table 6.4 are the best values obtained out of 32 different devices.

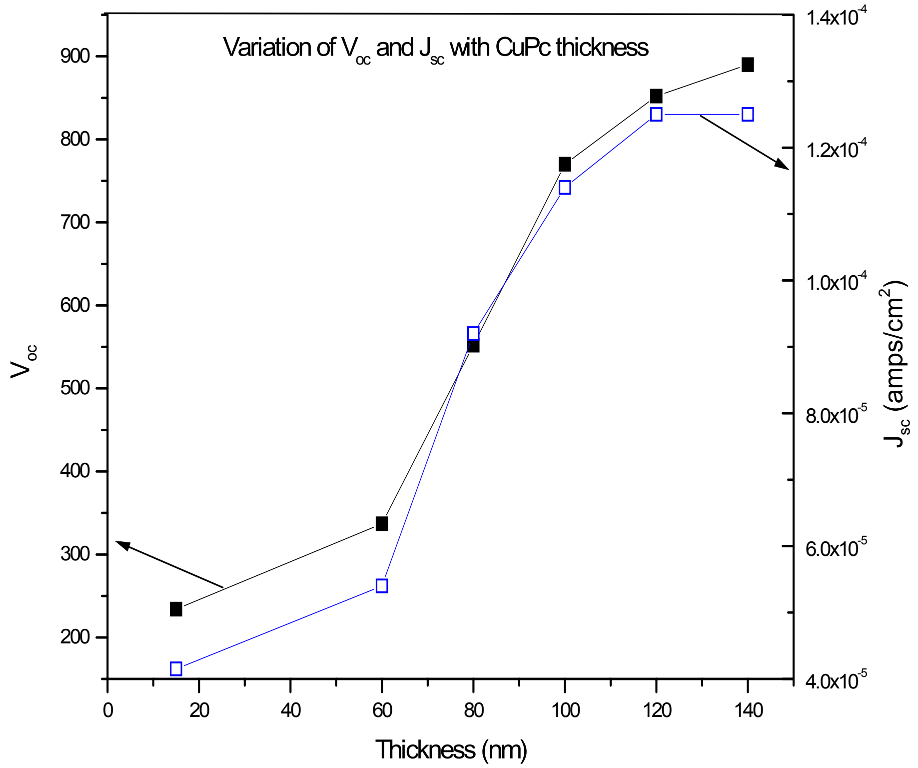

.

Figure 6.49 Plot showing the variation of open circuit voltage(V_{oc}) and short circuit current(J_{sc}) with thickness of CuPc films.

Figure 6.49 shows a plot of change in open circuit voltage and short circuit current with the CuPc thickness. From the plot it can be observed that the open circuit voltage (V_{oc}) increases with the thickness of the CuPc film. This increase in the open circuit voltage can be attributed to the increasing absorption of light by CuPc and the generation of more excitons with increasing thickness. In case of the short circuit current, we observe a rapid increase initially but as the thickness of the CuPc layer reaches 120 nm the increase in the short circuit current value is less. This shows that the short circuit current is series resistance limited at higher thickness of CuPc layer. We also observed a slight increase in the efficiency of the cells with the increasing thickness of CuPc layer. The overall efficiency of the cells is less when compared to their inorganic counter parts because of limited absorption of light across the solar spectrum and low charge carrier mobilities in organic layers. It can be observed from Table 6.3 and Table 6.4 that these diodes have a high diode ideality factors which indicate several transport mechanisms like recombination-generation currents in the depletion region and recombination through interface states at the junction.

6.7 J-V characteristics of TiO_2/CuPc based solar cells

The structure of the two TiO_2/CuPc based structures that were investigated are Glass/ITO/TiO_2/CuPc/Al, Glass/ITO/TiO_2/CuPc/PTCBI/Al.

6.7.1 J-V characteristics of Glass/ITO/TiO_2/CuPc/Al device

Figure 6.50 shows the J-V characteristics of the device Glass/ITO/TiO_2/CuPc (15 nm)/Al under dark conditions. The series resistance(R_s) of the curve in Figure 6.50 was calculated to be 11 kΩ/cm^2. The J-V characteristic was then corrected for series resistance by subtracting JR_s from V. Figure 6.51 shows the plot of V vs. J and ($V-JR_s$) vs. J.

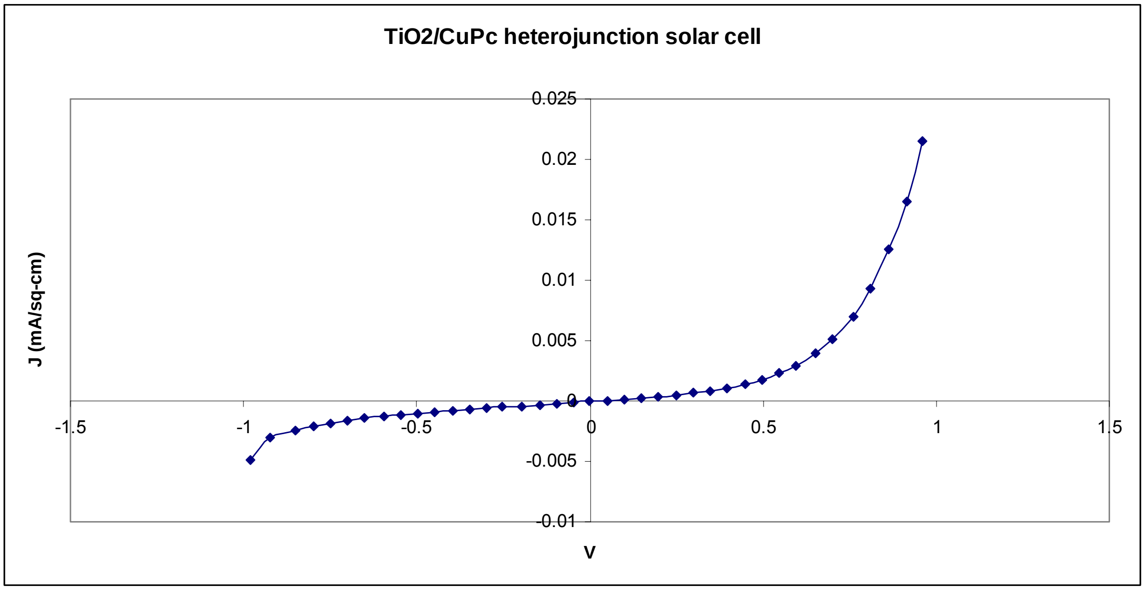

Figure 6.50 Glass/ITO/TiO_2/CuPc(15 nm)/Al heterojunction solar cell dark curve.

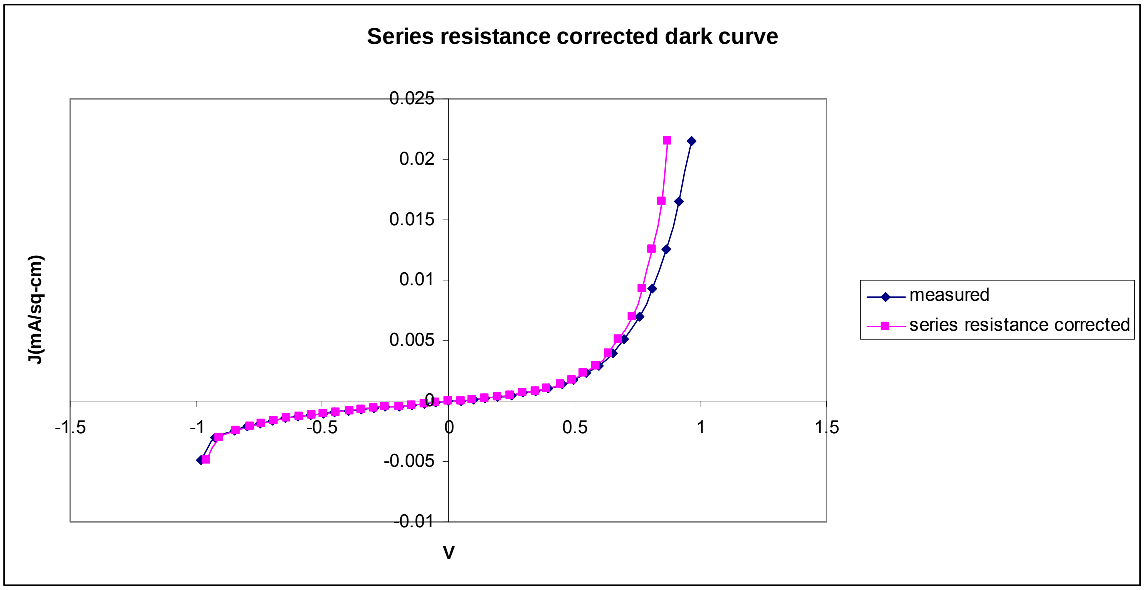

Figure 6.51 Series resistance corrected dark curve for Glass/ITO/TiO_2/CuPc(15 nm)/Al device.

Figure 6.52 shows the plot of ln(J) vs. V from which the value of J_o was calculated to be 0.203 μA/cm^2. The diode ideality factor n was calculated to be 7.08.

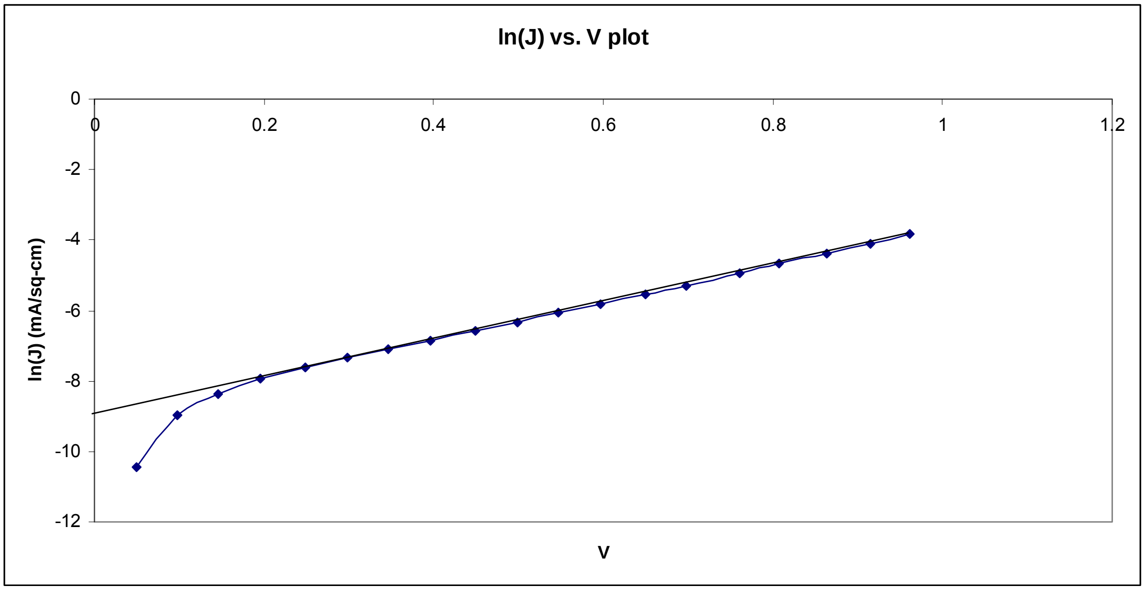

Figure 6.52 ln(J) vs. V plot for determining n and J_0 for Glass/ITO/TiO_2/CuPc(15 nm)/Al device dark curve.

Figure 6.53 shows the J-V characteristics of the device Glass/ITO/TiO_2/CuPc (15 nm)/Al under illumination. The series resistance (R_s), ideality factor and reverse saturation current were calculated to be 9.1 kΩ/cm^2, 10.48 and .93 μA/cm^2 respectively. .The J-V characteristic was then corrected for series resistance by subtracting JR_s from V. Figure 6.54 shows the plot of V vs. J and (V-JR_s) vs. J.

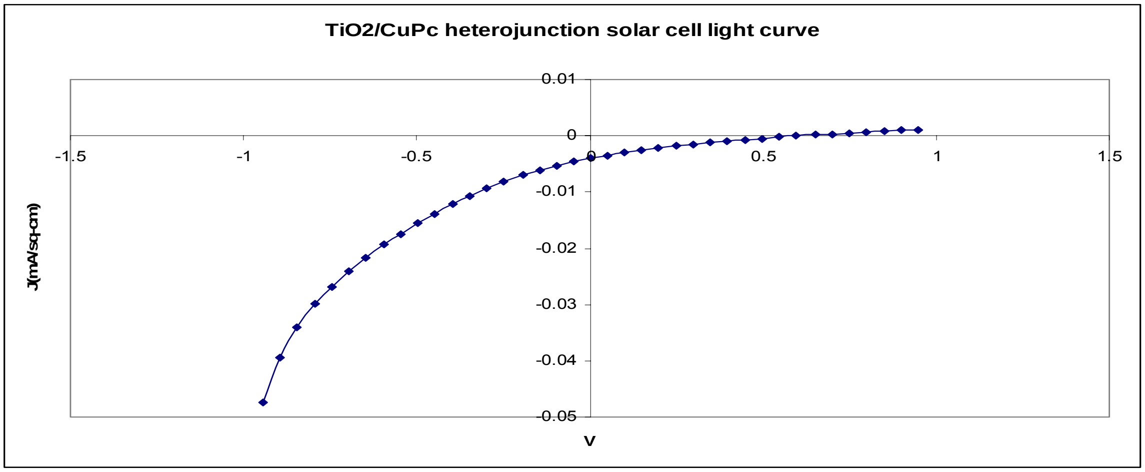

Figure 6.53 Glass/ITO/TiO_2/CuPc(15 nm)/Al heterojunction solar cell light curve.

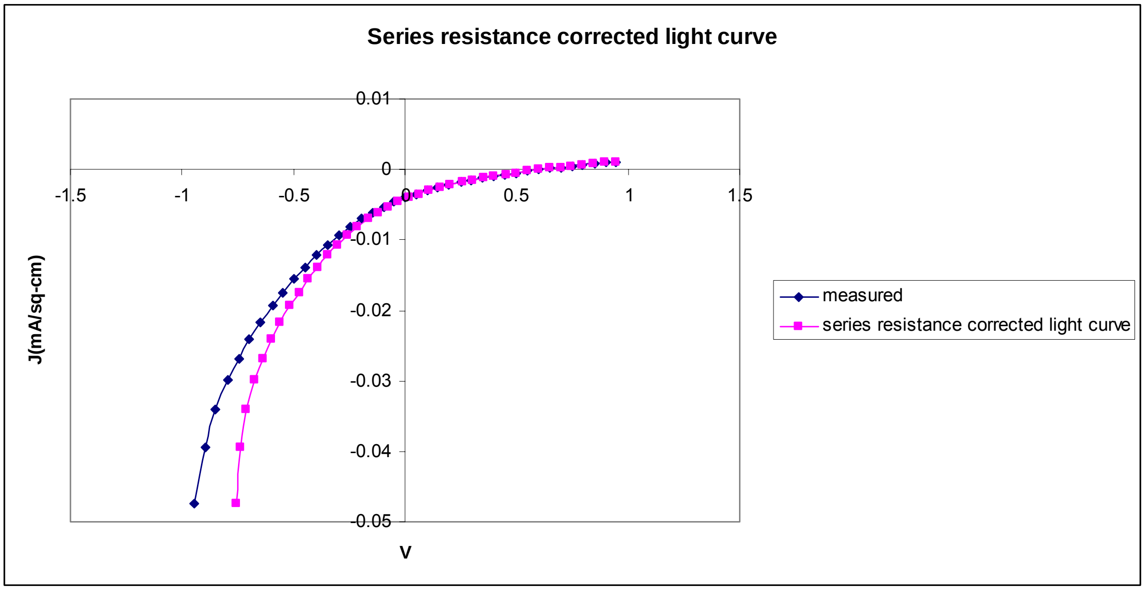

Figure 6.54 Series resistance corrected light curve for Glass/ITO/TiO_2/CuPc(15 nm)/Al device.

The Glass/ITO/TiO_2/CuPc (15 nm)/Al cell yielded a V_{oc} and J_{sc} of 650 mV and 0.0037 mA/cm^2 respectively. The power delivered was 0.488 μW/cm^2 and the fill factor was 0.203. The cell had an efficiency of 0.0004 %.

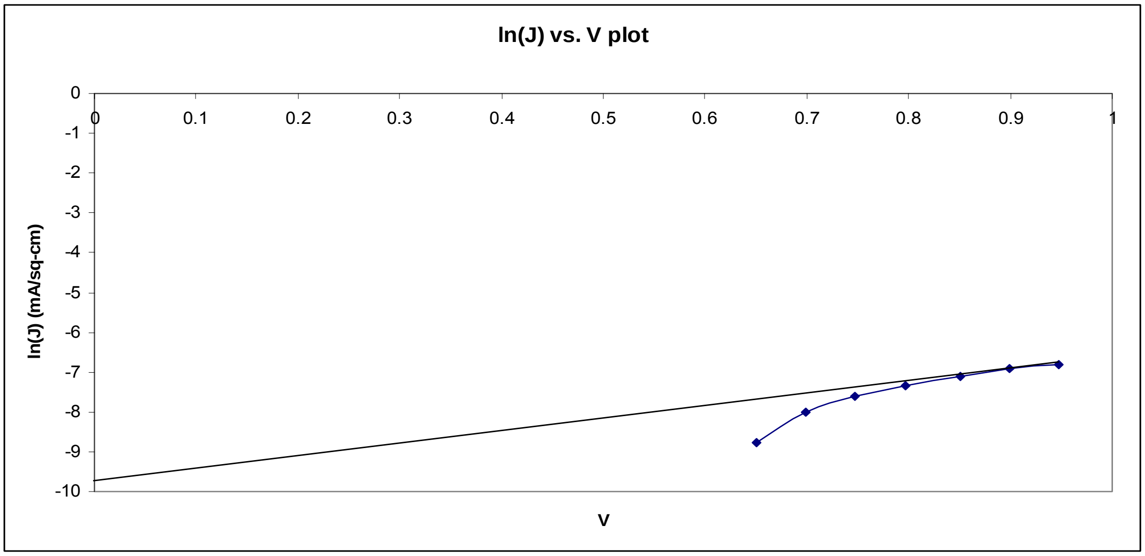

Figure 6.55 ln(J) vs. V plot for determining n and J_0 for Glass/ITO/TiO_2/CuPc(15 nm)/Al device light curve.

6.7.2 J-V characteristics of the Glass/ITO/TiO_2/CuPc/PTCBI/Al device

Figure 6.56 shows the J-V characteristics of the device Glass/ITO/TiO_2/CuPc (15 nm)/PTCBI/Al under illumination. The series resistance (R_s) of the curve in Figure 6.56 was calculated to be 12.2 kΩ/cm^2. The J-V characteristic was then corrected for series resistance by subtracting JR_s from V. Figure 6.57 shows the plot of V vs. J and ($V-JR_s$) vs. J.

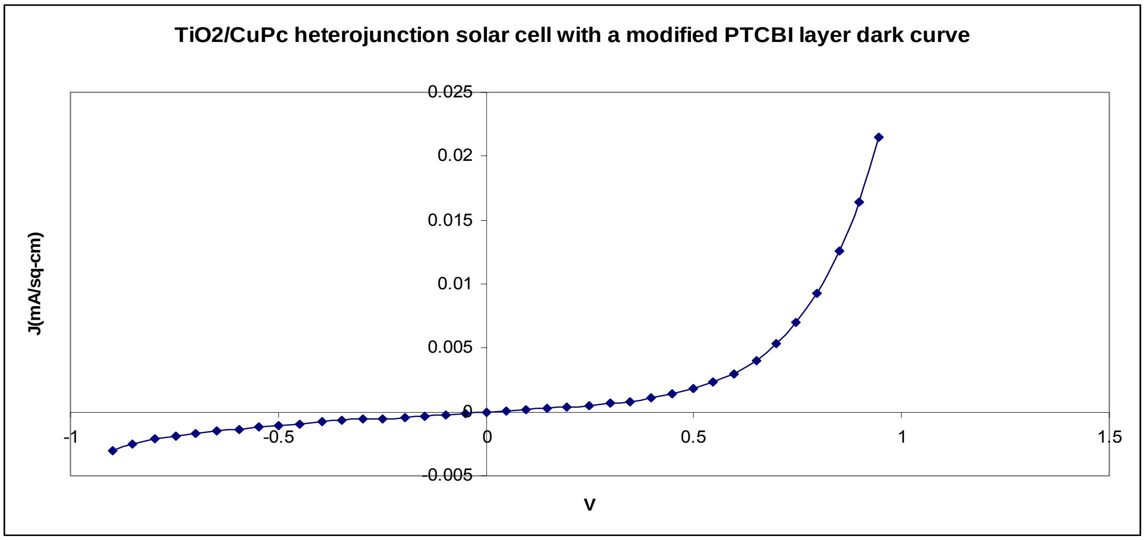

Figure 6.56 Glass/ITO/TiO_2/CuPc(15 nm)/PTCBI(7 nm)Al heterojunction solar cell dark curve.

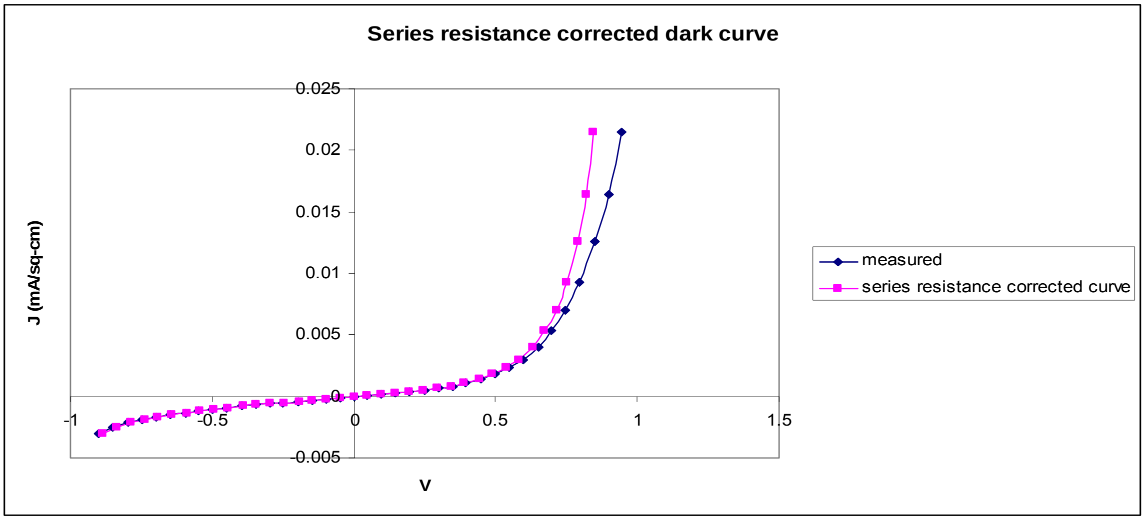

Figure 6.57 Series resistance corrected dark curve for Glass/ITO/TiO_2/CuPc(15 nm)/PTCBI/Al device.

Figure 6.58 shows the plot of ln(J) vs. V from which the value of J_o was calculated to be 0.018 μA/cm^2. The diode ideality factor n was calculated to be 6.94.

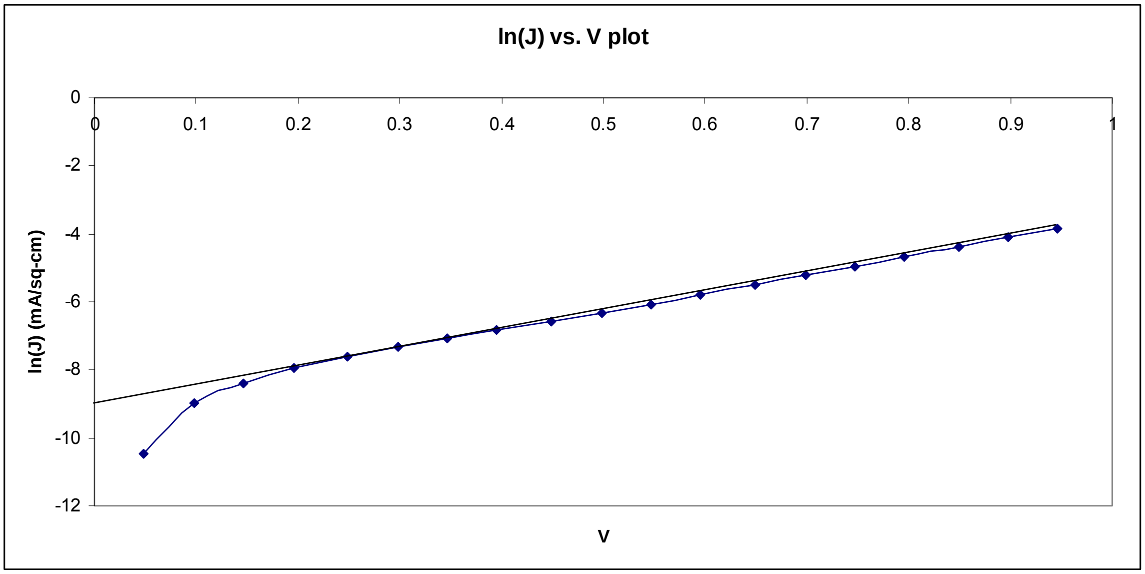

Figure 6.58 ln(J) vs. V plot for determining n and J_0 for Glass/ITO/TiO_2/CuPc (15 nm)/PTCBI/Al device dark curve.

Figure 6.59 shows the J-V characteristics of the device Glass/ITO/TiO_2/CuPc (15 nm)/PTCBI/Al under illumination. The series resistance (R_s), ideality factor and reverse saturation current were calculated to be 10.1 kΩ/cm^2, 9.36 and .05 μA/cm^2 respectively. The J-V characteristic was then corrected for series resistance by subtracting JR_s from V. Figure 6.60 shows the plot of V vs. J and ($V-JR_s$) vs. J.

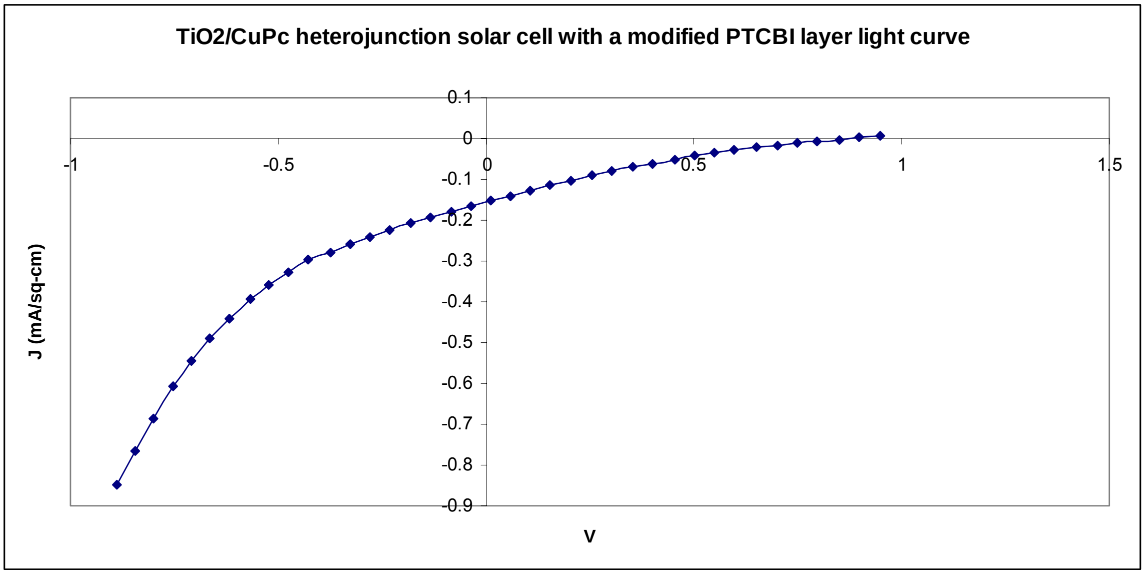

Figure 6.59 Glass/ITO/TiO_2/CuPc (15 nm)/PTCBI (7 nm)Al heterojunction solar cell light curve.

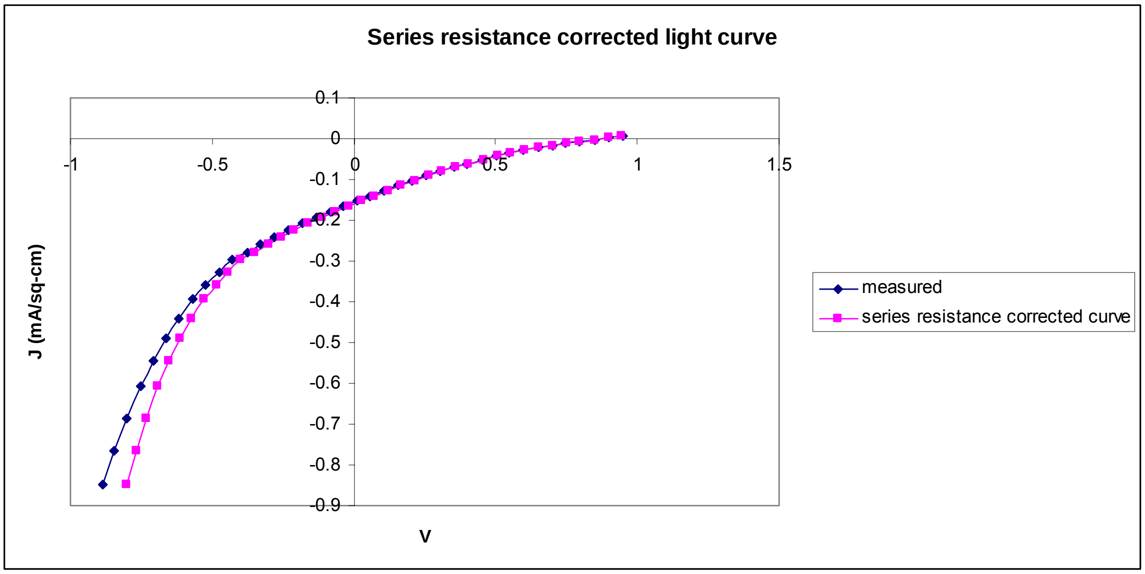

Figure 6.60 Series resistance corrected light curve for Glass/ITO/TiO_2/CuPc (15 nm)/PTCBI (7 nm)/Al device.

The Glass/ITO/TiO_2/CuPc (15 nm)/PTCBI/Al cell yielded a V_{oc} and J_{sc} of 850 mV and 0.153 mA/cm^2 respectively. The power delivered was 0.024 mW/cm^2 and the fill factor was 0.184. The cell had an efficiency of 0.024 %.

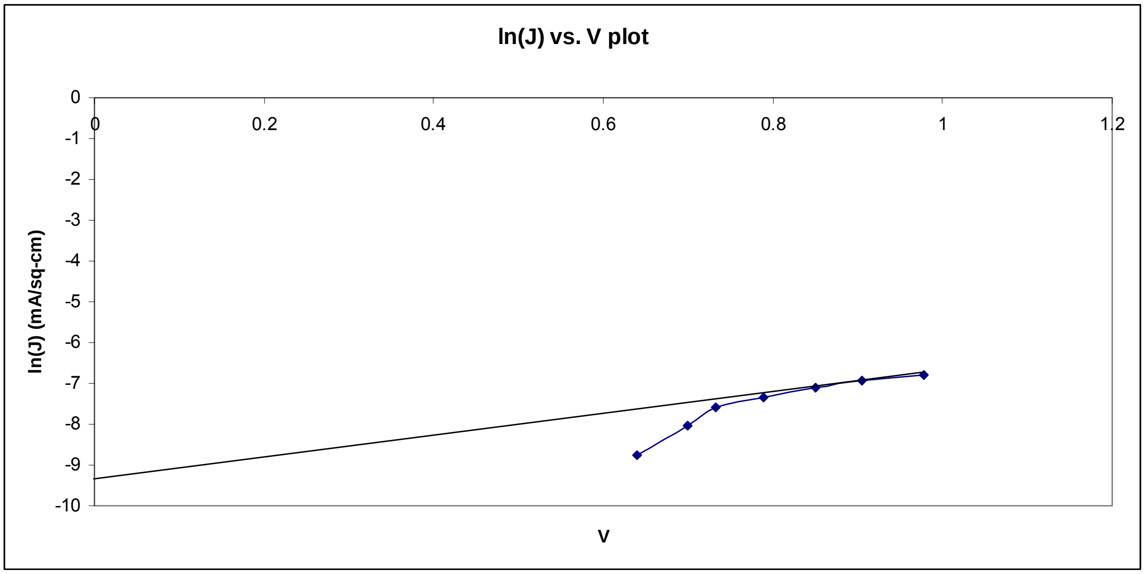

Figure 6.61 ln(J) vs. V plot for determining n and J_0 for Glass/ITO/TiO_2/CuPc(15 nm)/PTCBI(7 nm)/Al device light curve.

Structure	Series Resistance (R_s)	Ideality Factor (n)	J_o
ITO/TiO_2/CuPc/Al	11 kΩ/cm^2	7.08	0.203 µA/cm^2
ITO/TiO_2/CuPc/PTCBI/Al	12.2 kΩ/cm^2	6.94	0.018 µA/cm^2

Table 6.5 Results of TiO_2/CuPc/Al, TiO_2/CuPc/PTCBI/Al solar cell dark curves.

Table 6.5 shows the series resistance, diode ideality factor and reverse saturation current densities of the structures ITO/TiO_2/CuPc/Al and ITO/TiO_2/CuPc/PTCBI/Al. These devices suffer from high series resistance offered by the CuPc and TiO_2 layers. The low electrical conductivity of the CuPc layer can be attributed to the high series resistance observed.

Structure	**R_s**	**n**	**J_o**	**V_{oc}**	**J_{sc}**	**F. F.**	**P. D.**	**η**
ITO/TiO_2/ CuPc/Al	9 kΩ/cm^2	10.4	0.93 μA/cm^2	650 mV	0.0037 mA/cm^2	0.20	0.488 μW/cm^2	0.0004 %
ITO/TiO_2/ CuPc/PTCBI/Al	10.1 kΩ/cm^2	9.36	0.05 μA/cm^2	850 mV	0.153 mA/cm^2	0.18	0.024 mW/cm^2	0.024 %

Table 6.6 Results of TiO_2/CuPc heterojunction and TiO_2/CuPc heterojunction with a modified PTCBI layer light curves.

Table 6.6 shows the cell parameters for ITO/TiO_2/CuPc/Al and ITO/TiO_2 /CuPc/PTCBI/Al structures. As in the case of the dark curves the light curves also suffer from high series resistance offered by the CuPc and TiO_2 layers. The low value of reverse saturation current in case of the ITO/TiO_2/CuPc/PTCBI/Al structure when compared to the ITO/TiO_2/CuPc/Al structure suggests that the PTCBI layer is protecting the CuPc layer from being damaged by the high energy aluminium atoms. As hypothesized by V.P. Singh et al. [29] part of the PTCBI layer may actually be used up by aluminium in the formation of aluminium oxide (Al_2O_3) which forms a thin insulating layer and thereby protecting the CuPc from being damaged. Apart from forming a heterojunction with CuPc, the presence of pores in the TiO_2 layer helps in the scattering of light resulting in the increase of optical path and thereby increasing the open circuit voltage of the device. A considerable increase in the short circuit current could not be observed because of the high series resistance offered by the CuPc layer. The ITO/TiO_2/CuPc/PTCBI/Al structure shows a better photovoltaic behavior because of the protection of CuPc layer by the thin PTCBI layer. The cells suffer from low efficiencies due to various factors like high series resistance, low carrier mobilities in the organic layer and rapid degradation of organic films when exposed to air.

Chapter 7. Discussion

7.1 Material characterization of C_{60}

C_{60} is a molecule that consists of 60 carbon atoms in the form of a sphere. This sphere is made up of 12 hexagons and 12 pentagons with a carbon atom on each corner. C_{60} is a well known n-type organic semiconductor used in the fabrication of solar cells and OLEDs. Figure 4.1 shows the SEM image of the C_{60} film at high magnification and Figure 4.2 shows the SEM image of C_{60} at low magnification. The average particle size of C_{60} deposited on an ITO coated glass substrate was 30 nm. The low magnification image shows that the deposited film was uniform.

Figure 4.3 shows the X-ray diffraction pattern of the C_{60} film. The C_{60} film that was thermally evaporated showed peaks at 2θ positions of 10.1^0, 22^0 and 34^0 which correspond to 111, 222 and 333 planes respectively. C_{60} films did not show any preferred orientation which can be attributed to lattice mismatch between C_{60} and ITO. The peaks produced by C_{60} films were compared to the ones that were obtained by Z. Dai et al. [30]. The peaks produced at 2θ positions of 23^0, 30^0, 31^0, 35^0, 37^0, 45^0, 51^0 and 60^0 are produced by ITO.

7.2 Optical characterization of C_{60}

The Optical absorption plot of a material gives a fair idea of the absorption characteristics of the material in the visible spectrum, which is an important characteristic of a good photovoltaic material. A good photovoltaic material should have broad peaks of absorption in the visible spectrum of light to utilize most of the light passing through it to generate carriers. Absorption vs. wavelength plot of C_{60} film of thickness 40 nm is shown in Figure 5.1. The absorption plot shows peaks at wavelengths of 350 nm and at 450 nm. The absorption plot showed peaks at the same positions as obtained by Tetsuya Taima et al. [4]. C_{60} is a symmetric molecule and hence the transition between the HOMO and LUMO levels is forbidden, which can be attributed to the lack of a strong absorption band in the visible region of the absorption spectrum of C_{60} [4].

7.3 Electrical characterization of C_{60} Schottky diode solar cells

The ITO/C_{60}(40 nm)/LiF/Al structure showed a series resistance of 78.06 Ω/cm^2 and the ITO/PEDOT:PSS/C_{60}(60 nm)/LiF/Al structure showed a series resistance of 0.75 kΩ/cm^2 in case of the dark curves. The increase in the value of series resistance from the ITO/C_{60} (40 nm)/LiF/Al structure to the ITO/PEDOT:PSS/C_{60} (60 nm)/LiF/Al structure can be attributed to low carrier mobilities in the PEDOT:PSS layer. A Lithium Fluoride (LiF) layer of thickness 1 nm was deposited on the C_{60} films before the deposition of aluminium to protect the C_{60} layer from being damaged by the high energy aluminium atoms. In the case of both these devices a Schottky barrier is formed between the C_{60} layer and the aluminium layer since the thickness of LiF layer is 1 nm. The PEDOT:PSS layer which was used in the ITO/PEDOT:PSS/C_{60} (60 nm)/LiF/Al structure serves to make the surface of the ITO smooth and also to reduce the availability of shunting paths between aluminium and the ITO.

The value of diode ideality factor for dark curves in the case of the ITO/C_{60} (40 nm)/LiF/Al structure was 5.73 and its value is 13 in case of ITO/PEDOT:PSS/C_{60} (60 nm)/LiF/Al structure (see Table 6.1). These high diode ideality factors indicate several transport mechanisms like recombination-generation currents in the depletion region and recombination through interface states. The high diode ideality factors may also be attributed to tunneling from band states to localized defect states and band-to-band tunneling. The value of reverse saturation current for dark curves in the case of the ITO/C_{60} (40 nm)/LiF/Al structure was 0.019 mA/cm^2 and 0.047 mA/cm^2 in the case of the ITO/PEDOT:PSS/C_{60} (60 nm)/LiF/Al structure (see Table 6.1). The presence of physical shunting paths is reasonable considering these high reverse saturation currents and the fact that the curves have a slope in the third quadrant.

Table 6.2 indicates the variation of different cell parameters in the case of the ITO/C_{60} (40 nm)/LiF/Al and the ITO/PEDOT:PSS/C_{60} (60 nm)/LiF/Al structures. The increase in series resistance from 40 nm device (63.08 Ω/cm^2) to 60 nm device (0.12 kΩ/cm^2) was also observed in the case of the light curves. The increase in the value of open circuit voltage from 190 mV (40 nm device) to 310 mV (60 nm device) without any increase in the value of short circuit currents (0.49 mA/cm^2 for 40 nm device and 0.48 mA/cm^2 for 60 nm device) indicates the availability of fewer shunting paths in case of the

60 nm device as a result of the inclusion of the PEDOT:PSS layer. An increase in the efficiency from 0.021% (40 nm device) to 0.028% (60 nm device) was also observed. Tetsuya Taima et al. [4] have reported an open circuit voltage of 0.046 V and a short circuit current of 2.77 x 10^2 mA/cm^2 for ITO/C_{60} (100 nm)/Al structure. The high values of open circuit voltage observed in C_{60}/Al Schottky diodes fabricated in our lab can be attributed to the reduction in the thickness of the C_{60} layer as compared to the devices fabricated by Tetsuya Taima et al.. The value of short circuit currents can be increased by sublimating C_{60} before thermal evaporation since sublimation is known to eliminate the impurities present in the material.

7.4 Material characterization of CuPc

CuPc was used in the fabrication of ITO/PEDOT:PSS/CuPc/Al, ITO/TiO_2/CuPc/Al and ITO/TiO_2/CuPc/PTCBI/Al structures. CuPc is a well known p-type organic semiconductor used in the fabrication of organic solar cells and OLEDs. Figures 4.4 and 4.5 show the SEM images of CuPc at high and low magnifications respectively. It can be observed from Figure 4.4 that the average particle size of the CuPc film is approximately 30 nm.

Figure 4.6 shows the X-ray diffraction pattern of the CuPc film. The CuPc film showed a peak at 2θ position of 6.85^0 which corresponds to 111 plane as observed by M.M. El-Nahass et al. [31]. The peaks at 2θ position of 23^0, 30^0, 31^0, 35^0, 37^0, 45^0, 51^0 and 60^0 are produced by ITO. The fact that the CuPc film showed a single peak at 2θ position of 6.85^0 shows that it has a preferred orientation which results in better transportation of carriers.

7.5 Optical characterization of CuPc

The absorption vs. wavelength plots of CuPc films of thickness 15nm, 60 nm, 80 nm, 100 nm, 120 nm and 140 nm are plotted together in Figure 5.15. These plots showed absorption peaks at wavelengths 350 nm, 620 nm and 700 nm as observed by C.Y. Kwong et al. [7]. The absorption of these films increased with the thickness of the films as expected. Figure 5.16 shows the absorption coefficient vs. wavelength plot of the CuPc films. It can be observed from Figure 5.16 that the absorption coefficients of the

CuPc films of thickness 80nm, 100 nm, 120 nm and 140 nm are approximately equal. The absorption coefficients of CuPc films of thickness 15 nm and 60 nm are less than the absorption coefficients of films of thickness 80 nm and above. This behavior can be attributed to the scattering of light, and to reflection in 15 nm and 60 nm films since the thickness of the films is less compared to the films of thickness 80 nm and above.

7.6 Electrical characterization of CuPc Schottky diode solar cells

ITO/PEDOT:PSS/CuPc (x)/Al devices were fabricated and were measured to calculate the photovoltaic parameters where ‘x’ is the thickness of the CuPc layer and its values are 15 nm, 60 nm, 80 nm, 100 nm, 120 nm and 140 nm. Table 6.3 shows the variation of series resistance, ideality factor and reverse saturation current of these devices measured in the dark. In these devices, the Schottky barrier is formed between the CuPc layer and aluminium. PEDOT:PSS was used to smooth the surface of ITO. From Table 6.3 it can be seen that the series resistance increases with increases in the thickness of the CuPc film. The high values of series resistance in the case of these devices can be attributed to low carrier mobilities in the CuPc film and PEDOT:PSS layer. The value of reverse saturation current in these devices is also high indicating the presence of physical shunting paths available between aluminium and ITO. Also, the slope of the curves in the third quadrant indicates the presence of physical shunting paths. The diode ideality factor in these devices were also high indicating that the current transport in these devices cannot be explained with just the diffusion current dominated model. The other transport mechanisms like recombination-generation currents in the depletion region, band-to-band tunneling and recombination through interface states at the junction may be operative at the interface.

Table 6.4 lists the photovoltaic parameters of the CuPc/Al Schottky diode solar cells. As in the case of CuPc/Al Schottky diode dark curves the increase in the series resistance with the thickness of the CuPc layer was also observed in case of the light curves. An increase in the value of open circuit voltage and short circuit current was observed with increase in the thickness of the CuPc layer, which can be attributed to the increased absorption of light with the thickness of the CuPc film as observed in Figure 5.15. Figure 6.49 shows a plot in which the values of V_{oc} and J_{sc} are plotted against the thickness of the CuPc layer. The values of open circuit voltage does not change much from 100 nm device to 140 nm device which suggests that the exciton diffusion length of the CuPc is approximately 120 nm. An exciton diffusion length of 10 to 50 nm for CuPc was suggested by Fan Yang et al. [32]. It may be possible that the some of the excitons generated in these Schottky devices are dissociated by the electrostatic field generated by the difference in work functions of ITO and Aluminium electrodes and hence the exciton diffusion length may actually be less than 100 nm. The efficiency of the CuPc Schottky diode solar cells increases with the thickness of the CuPc layer, which can be attributed to the increase in the open circuit voltage and short circuit current of these devices with the increase in the thickness of CuPc layer. The low values of efficiencies in case of the CuPc Schottky diode solar cells can be attributed to low mobility of carriers in CuPc films.

7.7 Material characterization of TiO_2

The TiO_2 sol-gel was spin coated on the surface of ITO with the help of a spincoater at an rpm of 2000. The TiO_2 films that were spin coated at higher speeds were of poor quality in terms of film uniformity. The TiO_2 sol-gel was spin coated 4 times on the substrates and the thickness of the film was found to be approximately 30 nm using profilometer measurements. ITO/TiO_2/CuPc/Al devices with 8 times spincoated TiO_2 layers were also fabricated but they did not yield any V_{oc} and J_{sc}. The motive behind using the TiO_2 layer in these devices was to increase the effective optical path of light by allowing the light to pass through the pores formed on the annealed TiO_2 layer. Figure 4.7 and Figure 4.8 show the high and low magnification images of the TiO_2 layer annealed at a temperature of 300^{O}C. The average particle size of the TiO_2 film was approximately 25 nm. The macropores formed on the TiO_2 film were of diameter 300 nm and the density of the pores formed is approximately 0.15 per $(\mu m)^2$.

7.8 Optical characterization of TiO_2

Figure 5.17 and Figure 5.18 show the absorption vs. wavelength and absorption coefficient vs. wavelength plots of the TiO_2 sol-gel that was spincoated on ITO substrates. The approximate thickness of the spincoated TiO_2 layer was 30 nm. The

TiO_2 film had absorption peaks at wavelengths of 500 nm and 300 nm. The low absorption peaks of the TiO_2 film indicate that the film is a good window layer which can be used in solar cells.

7.9 Electrical characterization of ITO/TiO_2/CuPc/Al and ITO/TiO_2/CuPc/PTCBI/Al solar cells

ITO/TiO_2/CuPc (15 nm)/Al solar cells were fabricated with the motive of increasing the effective optical path of light by allowing light to pass through the pores formed in the annealed TiO_2 layer. In this device a heterojunction is formed at the interface of the CuPc (15 nm) layer and the spincoated TiO_2 layer. Also, a Schottky barrier is formed at the interface of the CuPc layer and the Aluminium layer. The value of open circuit voltage observed in case of the CuPc (15 nm)/Al Schottky diode solar cell was 430 mV (see Table 6.6) less than the value of open circuit voltage observed in TiO_2/CuPc(15 nm)/Al structure indicating the dominance of the TiO_2/CuPc heterojunction over the CuPc(15 nm)/Al Schottky barrier. The density of the pores formed on the surface of annealed TiO_2 was low (0.15 per $(\mu m)^2$), hence the effective optical path of light could not be increased significantly. Table 6.5 shows the values of series resistance, diode ideality factor and reverse saturation current obtained from the J-V characteristics of the dark curve of ITO/TiO_2/CuPc (15 nm)/Al structure. The value of series resistance was found to be 11 $k\Omega/cm^2$ indicating the high series resistance offered by the CuPc and TiO_2 layers. The value of diode ideality factor was found to be 7.08 which is quite high indicating the presence of several transport mechanisms like generation-recombination currents and recombination through interface states. The value of reverse saturation currents is less when compared to the ITO/PEDOT:PSS/CuPc (x)/Al structures indicating less number of shunting paths available in the ITO/TiO_2/CuPc (15 nm)/Al structure.

Table 6.6 shows the values of photovoltaic parameters for the ITO/TiO_2/CuPc (15 nm)/Al structure. The value of open circuit voltage was 650 mV and the value of short circuit current was 0.0037 mA/cm^2. A.K. Ray et al. [8] have reported a ITO/TiO_2/CuPc (460 nm)/Au solar cell with an open circuit voltage of 0.024 V and a short circuit current of 0.012 mA/cm^2. The higher value of open circuit voltage observed in case of the TiO_2/CuPc/Al device fabricated in our lab can be attributed to the reduction in the thickness of CuPc layer from 460 nm (used by A.K Ray et al. [8]) to 15 nm which eliminates the recombination of excitons during their movement from the junction towards the metal contacts.

Table 6.5 shows the series resistance, diode ideality factor and reverse saturation current values of the ITO/TiO_2/CuPc (15 nm)/PTCBI/Al structure. PTCBI, a well known n-type organic semiconductor was used both to form a heterojuntion with the CuPc layer and also to protect the CuPc layer from high energy Aluminium atoms. In this device a heterojunction is formed at the interface of TiO_2 and CuPc layers and also at the interface of CuPc and PTCBI layers. The increase in the value of open circuit voltage from ITO/TiO_2/CuPc (15 nm)/Al structure to ITO/TiO_2/CuPc (15 nm)/PTCBI/Al structure suggests that the CuPc/PTCBI junction is the dominant junction in the ITO/TiO_2/CuPc (15 nm)/PTCBI/Al structure. The value of series resistance was calculated to be 12.2 kΩ/cm^2, which can be attributed to the low mobility of carriers in CuPc and PTCBI layers. The value of diode ideality factor was calculated to be 6.94 indicating the presence of several transport mechanisms like generation-recombination currents, recombination through interface states and band-to-band tunneling. The low value of reverse saturation current (0.018 μA/cm^2) shows the presence of less number of shunting paths available in the device.

Table 6.6 shows the photovoltaic parameters of the ITO/TiO_2/CuPc (15 nm)/PTCBI/Al structure. An increase in the values of open circuit voltage and short circuit current which can be seen from Table 6.6 was observed from ITO/TiO_2/CuPc (15 nm)/Al structure to ITO/TiO_2/CuPc (15 nm)/PTCBI/Al structure which can be attributed to the addition of a more dominant CuPc (15 nm)/PTCBI junction to the TiO_2/CuPc (15 nm) junction. These cells suffer from low efficiencies due to various factors like low carrier mobilities in the organic layers and rapid degradation of the organic films when exposed to air.

Chapter 8. Conclusions

C_{60}/Al Schottky diode solar cells were fabricated on ITO coated glass slides. The 40 nm thick C_{60} device yielded a open-circuit voltage of 190 mV and a short-circuit current density of 0.49 mA/cm^2. LiF was used to improve the fill factor of the devices and also to shield the C_{60} from high energy Aluminium atoms. The 60 nm thick C_{60} device yielded an open circuit voltage of 310 mV and a short circuit current of 0.48 mA/cm^2. We can observe an increase in the open circuit voltage of the 60 nm device when compared to the 40 nm device. The increase in the open circuit voltage can be attributed to the increase in the absorption of the film. The low mobilties of charge carriers in the organic films and also the PEDOT:PSS layer resulted in high series resistance and low current values.

Also, CuPc/Al Schottky diode solar cells were fabricated on ITO coated glass substrates. We observed an increase in open circuit voltage from 220 mV in the case of the 15 nm thick device upto 907 mV in the case of the 140 nm thick device. The increase in the open circuit voltage can be attributed to the increasing absorption of light by CuPc and generation of more excitons with increasing thickness. In case of the short circuit current, we observe a rapid increase initially from 0.042 mA/cm^2 (15 nm thick device) to 0.124 mA/cm^2 (120 nm thick device) but as the thickness of the CuPc layer reaches 120 nm the increase in the short circuit current is less which can be observed from the short circuit current for the 140 nm thick device whose value is 0.125 mA/cm^2. This shows that the short circuit current is series resistance limited at higher thickness of the CuPc layer. We also observed an increase in the efficiency of the cells from 0.003% (15 nm thick device) to 0.046% (140 nm thick device) with increasing thickness of the CuPc layer. The overall efficiency of the cells is very small when compared to their inorganic counterparts because of limited absorption of light across the solar spectrum and low charge carrier mobilities in organic layers.

Furthermore, TiO_2/CuPc/Al and TiO_2/CuPc/PTCBI/Al devices were fabricated on ITO coated glass substrates. The values of open circuit voltage were 650 mV in case of ITO/TiO_2/CuPc/Al structure and 850 mV in case of the ITO/TiO_2/CuPc/PTCBI/Al structure. These values of open circuit voltages were one of the highest ever reported values for TiO_2 based solar cells. The low value of reverse saturation current in case of the ITO/TiO_2/CuPc/PTCBI/Al structure whose value is 0.05 μA/cm^2 when compared to the ITO/TiO_2/CuPc/Al structure whose value is 0.93 μA/cm^2 suggests that the PTCBI layer is protecting the CuPc layer from being damaged by the Aluminium atoms and thereby reducing the shunting paths available. The cells suffer from low efficiencies due to various factors like high series resistance and low carrier mobilities in the organic layers.

Chapter 9. Suggestions to future work

The efficiency of the C_{60} and CuPc Schottky diode solar cells can be greatly improved by depositing the C_{60} and CuPc in porous alumina templates and thereby increasing the scattering of light. Electrodeposition of the organic films instead of thermal evaporation can be more useful since electrodeposition leads to a better conformal deposition of the films into the pores. The performance of the TiO_2 based devices can be improved by annealing the TiO_2 films at a higher temperature. A study of lifetime of the organic solar cells can also be very useful in judging the practical usage of these cells. Organic semiconductors with higher mobilities as opposed to the ones used in this work can also be very useful for the fabrication of solar cells with higher efficiencies.

The organic materials used in this work were deposited without being subjected to any prior purification before deposition. Sublimation of the organic materials is known to improve their purity and thereby increasing the mobility of carriers. C_{60}, CuPc and PTCBI can be purified by sublimation before thermal evaporation which can lead to higher efficiencies. Also, other metal electrodes like silver, gold and platinum can be used in place of aluminium to increase the value of short circuit currents. Also, the composition of the chemicals used in the TiO_2 sol-gel can be varied to increase the density of pores and thereby increasing the effective optical path of light. ITO/TiO_2/CuPc/PTCBI/Al device with an open circuit voltage of 850 mV and a short circuit current density of 0.153 mA/cm^2 is the best device to pursue for further work. The value of efficiency which is 0.024% for the ITO/TiO_2/CuPc/PTCBI/Al device, can be increased by decreasing the value of series resistance. Sublimation of the organic materials used in the fabrication of the device can lead to lower values of series resistance and hence higher values of short circuit currents.

References

1. V. D. Mihailetchi, P. W. M. Blom, J. C.Hummelen and M. T. Rispens, Journal of Applied Physics, Vol. 94, Number 10, 2003.
2. C. W. Tang, Applied Physics Letters, 48, 1986.
3. Jenny Nelson, James Kirkpatrick and P. Ravirajan, Physical Review B 69, 035337, 2004.
4. Tetsuya Taima, Masayuki Chikamatsu, Raghu Nath Bera, Yuji Yoshida, Kazuhiro Saito and Kiyoshi Yase, The Journal of Physical Chemistry, Vol. 108, Number 1, January 8, 2004.
5. F.T. Reis, D. Mencaraglia, S. Oould Saad, I. Seguy, M.Oukachmih, P.Jolinat, P.Destruel, Synthetic Metals 138, 2003.
6. H. Ding, M. K .Ram, L. Zheng, C. Nicolini, Journal of Material Science 36 (2001).
7. C.Y. Kwong, A.B.Djurisic, P.C. Chui, L.S.M. Lam, W.K. Chan, Applied Physics A, Material Science & Processing, 77, 555-560 (2003).
8. A. K. Ray, S.M. Tracey, A.K. Hassan, S.T. Shishiyanu, T.S. Shishiyanu, Moldavian Journal of The Physical Sciences, N2, 2002.
9. S. M. Sze, Physics of semiconductor devices, 2nd edition, Chapter 5.
10. R. S. Muller, Theodore Cummins, Solid State Electronic Devices, Chapter 2.
11. Ben G. Streetman, Solid State Electronic Devices, Prentice Hall, 3rd edition.
12. Jenny Nelson, Current Opinion in Solid State & Materials Science 6 (2002) 87-95.
13. Brian A. Gregg, Journal of Physical Chemistry B 2003, 107, 4688-4698.
14. D. Meissner, J. Rostalski, Synthetic Materils 121 (2001) 1551-1552.
15. Charles Kittel, Introduction to Solid State Physics, 7th edition, John Wiley and Sons.
16. Thomas Stubinger and Wolfgang Brutting, Journal of Applied Physics, Vol. 90, Number 7, 2001.
17. Jenny Nelson, The Physics of Solar Cells, Imperial College Press.
18. Brabec, V. Dyakonov, J. Parisi, N. S. Sacricifti, Organic Photovoltaics, Springer Series.
19. Alan L. Fahrenbruch, Richard H. Bube, Fundamentals of Solar cells, Academic press, INC.
20. David L. Pulfrey, Photovoltaic Power Generation, Van Nostrand Reinhold

Company.

21. W.D. Johnston, Jr., Solar Voltaic Cells, Marcel Dekker, INC.
22. Kasturi Lal Chopra, Suhit Ranjan Das, Thin Film Solar Cells, Plenum Press.
23. Craig A. Grimes and R. Suresh Singh, Journal of Materials Research, 16(6), 2001.
24. R. Suresh Singh, C.A. Grimes and E.C.Dickey, Materials Reasearch Innovation, 5(3-4), 178-184, 2002.
25. Christoph J. Brabec, Sean E. Shaheen, Christoph Winder and N. Serdar Sacricifti, Applied Physics Letters, Vol. 80, Number 7, 2002.
26. Basics of X-Ray Diffraction, Thermo ARL, ARL Applied Research Laboratories. http://www.thermo.com/com/cda/home
27. Principles of Scanning Electron Microscopy, Department of Biology, University of Dayton.
28. Dr. Glagovich, Central Connecticut State University. http://www.chemistry.ccsu.edu/glagovich/teaching/472/uvvis/measure.html
29. V. P. Singh, R. S. Singh, B. Parthasarathy and A. Aguilera, Applied Physics Letters, 86, 2005.
30. Z. Dai, H. Naramoto, Journal of Physics, 1999.
31. M.M. El-Nahass, F.S. Bahabri, A.A. Al Ghamdi, S.R. Al-Habri, Egypt. J. Sol. Vol. (25), No. (2), (2002).
32. Fan Yang, Max Shtein and Stephen R. Forrest , Nature Materials 4, 37-41 (2005).

Vita

Subhash C.C. Vallurupalli was born in Eluru, West Godavari district, Andhra Pradesh, India on May 14, 1981. He received his Bachelor of Engineering degree in Electronics and Communication Engineering in 2002 from Osmania University, Hyderabad, India. He worked as a Research Assistant from 2004-2005 in the Electronic Devices Research Group at the University of Kentucky, Lexington, Kentucky, U.S.A..

Subhash C. C. Vallurupalli